SANDIA REPORT

SAND2005-7587
Unlimited Release
Printed December 2005

Materials Physics and Device Development for Improved Efficiency of GaN HEMT High Power Amplifiers.

Daniel D. Koleske, Andrew A. Allerman, S. R. Kurtz, Stephen R. Lee, Alan F. Wright, Carleton H. Seager, Nancy A. Missert, Albert G. Baca, Ronald D. Briggs, Phil F. Marsh, Chris P. Tigges, Randy J. Shul, David M. Follstaedt, and Paula P. Provencio

Prepared by
Sandia National Laboratories
Albuquerque, New Mexico 87185 and Livermore, California 94550

Sandia is a multiprogram laboratory operated by Sandia Corporation, a Lockheed Martin Company, for the United States Department of Energy's National Nuclear Security Administration under Contract DE-AC04-94AL85000.

Issued by Sandia National Laboratories, operated for the United States Department of Energy by Sandia Corporation.

Available to DOE and DOE contractors from
U.S. Department of Energy
Office of Scientific and Technical Information
P.O. Box 62
Oak Ridge, TN 37831

Telephone: (865)576-8401
Facsimile: (865)576-5728
E-Mail: reports@adonis.osti.gov
Online ordering: http://www.osti.gov/bridge

Available to the public from
U.S. Department of Commerce
National Technical Information Service
5285 Port Royal Rd
Springfield, VA 22161

Telephone: (800)553-6847
Facsimile: (703)605-6900
E-Mail: orders@ntis.fedworld.gov
Online order: http://www.ntis.gov/help/ordermethods.asp?loc=7-4-0#online

SAND2005-7587
Unlimited Release
Printed December 2005

Materials Physics and Device Development for Improved Efficiency of GaN HEMT High Power Amplifiers

Daniel D. Koleske and Andrew A. Allerman
Advanced Material Sciences Department

S. R. Kurtz and Stephen R. Lee
Semiconductor Material & Device Sciences Department

Alan F. Wright, Carleton H. Seager and Nancy A, Missert
Nanostructure and Semiconductor Physics

Albert G. Baca, Phil F. Marsh, and Ronald D. Briggs
RF Microsystems Technologies

Chris P. Tigges
Photonic Microsystems Technologies

Randy J. Shul
Microdevice Technologies

David M. Follstaedt, and Paula P. Provencio
Radiation-Solid Interactions Department

Sandia National Laboratories
P.O. Box 5800
Albuquerque, New Mexico 87185-0601

Abstract

GaN-based microwave power amplifiers have been identified as critical components in Sandia's next generation micro-Synthetic-Aperture-Radar (SAR) operating at X-band and Ku-band (10-18 GHz). To miniaturize SAR, GaN-based amplifiers are necessary to replace bulky traveling wave tubes. Specifically, for micro-SAR development, highly reliable GaN high electron mobility transistors (HEMTs), which have delivered a factor of 10 times improvement in power performance compared to GaAs, need to be developed. Despite the great promise of GaN HEMTs, problems associated with nitride materials growth currently limit gain, linearity, power-added-efficiency, reproducibility, and reliability. These material quality issues are primarily due to heteroepitaxial growth of GaN on lattice mismatched substrates. Because SiC provides the best lattice match and thermal conductivity, SiC is currently the substrate of choice for GaN-based microwave amplifiers. Obviously for GaN-based HEMTs to fully realize their tremendous promise, several challenges related to GaN heteroepitaxy on SiC must be solved.

For this LDRD, we conducted a concerted effort to resolve materials issues through in-depth research on GaN/AlGaN growth on SiC. Repeatable growth processes were developed which enabled basic studies of these device layers as well as full fabrication of microwave amplifiers. Detailed studies of the GaN and AlGaN growth of SiC were conducted and techniques to measure the structural and electrical properties of the layers were developed. Problems that limit device performance were investigated, including electron traps, dislocations, the quality of semi-insulating GaN, the GaN/AlGaN interface roughness, and surface pinning of the AlGaN gate. Surface charge was reduced by developing silicon nitride passivation. Constant feedback between material properties, physical understanding, and device performance enabled rapid progress which eventually led to the successful fabrication of state of the art HEMT transistors and amplifiers.

Acknowledgments

We acknowledge scientific discussion with J. Randall Creighton on the growth of AlGaN materials, specifically how best to avoid AlGaN particle formation during MOCVD growth. We acknowledge the daily technical contributions to the growth, characterization and device fabrication of the GaN-based HEMTs, including Jeffrey J. Figiel, Michael J. Russell, Robert J. Kaplar, Tom Bauer, Mary H. Crawford, Arthur J. Fischer, Christine C. Mitchell, Karen C. Cross, Mike Moran, Jim A. Bur, Kris W. Fullmer Karen E. Waldrip, Carlos Sanchez, Mark Overberg, and Alan M. West. Self-heating studies were conducted with Mark Holtz, I. Ahmad, V. Kasisomayajula and J. M. Berg from Texas Tech. University.

In Rememberance

Sadly, during the course of this work one of our colleagues, Steven R. Kurtz, passed away in a white water rafting accident while on the Middle Fork of the Salmon River in Idaho. He was 51. Steve contributed to the fundamental physical understanding of the HEMT structures developed in this program. Steve attended Bucknell University in Lewisberg, PA, where he was introduced to physics. In 1980, Steve graduated with a Ph. D. in condensed matter physics from at the University of Illinois and later that year he moved to Albuquerque to begin a successful career as research physicist at Sandia National Laboratories. He had over 300 publications to his credit at the time of his death. Steve's scientific work was always highly respected and of the utmost quality. As an example of this quality, his contributed submission to the 2005 Fall Meeting of the Material Research Society entitled "Quantum-Confined Stark Effect and Polarization Fields in Single Quantum Well InGaN/GaN LEDs" was so highly rated by the organizing committee that it was elevated to an invited talk. Dr. Robert J. Kaplar who worked closely with Steve will present this work at the MRS. Steve will be remembered for his unrelenting determination to live life to its fullest, his ability to develop scientific understanding of complex problems and for his quirky sense of humor. He will be sorely missed.

Contents

Figures List

Tables List

Nomenclature

2-DEG	Two dimensional electron gas
AFM	atomic force microscopy
AlN	aluminum nitride
AlGaN	aluminum gallium nitride
C	elemental carbon
CE	cantilever epitaxy
C-V	capicatance-voltage characterization
DFT	density functional theory
DLTS	deep level transient spectroscopy
DOD	department of defense
DOE	Department of Energy
DS&A	defense systems and assessments
ELOG	Epitaxial lateral overgrowth
eV	electron volt
FKO	Franz–Keldysh oscillations
GaN	gallium nitride
H	elemental hydrogen
H_2	hydrogen gas
Hall	Hall effect measurement
HEMT	high electron mobility transistor (same as HFET)
HFET	heterojunction field effect transistor (same as HEMT)
HS	homeland security
ICP	inductively coupled plasma
Ku-band	Frequency band 12-18 GHz
LDRD	laboratory directed research and development
MEMS	micro electro-mechanical system
μmoles	micromoles
MOCVD	metalorganic chemical vapor deposition
MOSS	muli-beam optical stress sensor
N_2	nitrogen gas
NH_3	ammonia gas
nm	nanometer
n-type	n-type doped semiconductor
NW	nuclear weapons
O	elemental oxygen
O_{Ga}	oxygen substituted on a Ga site
O_I	oxygen interstitial
O_N	oxygen substituted on a N site
PL	photoluminescence
p-type	p-type doped semiconductor
RDR	rotating disk reactor

RF	radio frequency
RMS	root-mean-square
SAR	synthetic aperture radar
SCCM	standard cubic centimeters per minute
SEM	scanning electron microscope
SETI	Sensor Electronic Technology, Inc.
SI	semi-insulating
Si	elemental silicon
SiC	silicon carbide
SIMS	secondary ion mass spectroscopy
SLPM	standard liters per minute
SMU	strategic management units
SNL	Sandia National Laboratories
TEM	transition electron microscopy
TMAl	trimethylaluminum
TMGa	trimethylgallium
TWT	Traveling wave tubes
UV	ultra-violet
V/III	ratio of group V elements to group III elements
VTD	vertical threading dislocations
X-band	Frequency band 8-12 GHz
XRD	x-ray diffraction

1. Introduction

1.1 Technical Problem

It is widely acknowledged that GaN-based amplifiers have the greatest potential to replace bulkier traveling wave tubes (TWTs) to miniaturize synthetic aperture radar (SAR). This replacement is possible due to the higher breakdown field, electron velocity, and thermal conductivity of GaN compared to other semiconductors. GaN-based high electron mobility transistors (HEMTs) have exhibited greater than 10 times the power density of GaAs-based HEMTs. The higher breakdown field in GaN also allows more compact transistor placement and efficient power combining between different transistors. These advantages of GaN-based HEMTs should revolutionize the miniaturization of X- and Ku-band amplifiers, enabling new types of miniature RF systems of immense importance to numerous critical NS and NW applications.

Despite the great potential observed in prototype devices, GaN HEMTs typically contain large numbers of defects that adversely affect device performance. These defects are a consequence of growing GaN on lattice-mismatched substrates such as sapphire and SiC. The use of sapphire and SiC are necessary because bulk GaN substrates are not currently available. Even when GaN substrates become available, they will not provide as much heat removal capability as SiC substrates. This suggests that the most efficiently cooled GaN HEMTs will be those grown on SiC and that the defects, which arise from the heteroepitaxy of GaN on SiC, must be reduced or their influence nullified.

In this LDRD, we developed a stable nitride-based HEMT growth and device fabrication capability to produce state-of-the-art electrical properties. Using the work of the LDRD as a base we were able to produce 20 Watt 3 GHz GaN-based microwave amplifiers. In this final report we describe many of the research steps used to achieve this milestone. We worked to identify defects and materials issues that limit GaN HEMT performance and where possible we found solutions to either remove the defects from the HEMT structure or nullify their influence on device performance. Because SiC provides the best heat removal of any substrate, research in this LDRD was primarily focused on materials growth, physical understanding and device fabrication of GaN HEMTs on SiC. In what follows we present some of the technical issues, technical approach, and expected results before this LDRD began. We also comment on the creativity and innovation of the approach and the impact and ties to DOE that this program will have made.

1.2 Technical Issues

The major technical issues associated with GaN HEMT technology are the presence of defects including traps and dislocations, thermal management of the operating devices, dislocations near the active regions, and growth and device fabrication reproducibility.

Defects are introduced into the HEMT structure (see Fig. 1.1) during the growth. The most common defects that occur in GaN are dislocations, impurities, and point defects. Dislocations originate in GaN at the hetero-interface partly due to the lattice mismatch between SiC and GaN and partly due to the discrete GaN grains, which form and ultimately coalesce on the SiC to form the film. Dislocations in GaN typically range from 10^8 to 10^{10} cm^{-2} and this density is independent of growth technique. Impurities and point defects on the other hand are more strongly influenced by the reactor growth conditions. Each of these defects can adversely affect device performance by creating charge trapping centers and leakage pathways, which can ultimately lead to device failure and reliability issues.

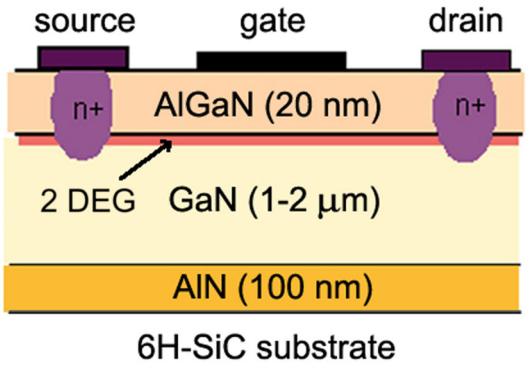

Fig. 1.1 Diagram of an AlGaN/GaN HEMT structure grown on SiC.

Trapping type defects can dramatically limit frequency performance, especially in the GaN or AlGaN layers near the two dimensional electron gas (2-DEG). For a HEMT to work properly the GaN must be insulating enough such that current flows only through the 2-DEG and not in parallel through the bulk GaN. If on the other hand, the semi-insulating (SI) GaN is too resistive electron traps may be present in the GaN. Traps can also produce current collapse in HEMT devices, which is caused when hot electrons are injected into the insulating GaN region. Once trapped, the electrons cannot be thermally emitted because of the large bandgap. As a result the electrons effectively back gate the device, leading to reduced current flow in the 2-DEG. In addition to hot electron injection, cycling either the gate or drain voltage can cause transient reductions in the drain current. Traps are also likely present in the AlGaN and at surface of HEMTs. Traps may result from impurity, vacancy, or dislocation structures. Ultimately, these traps limit gain, linearity, power-added-efficiency, reproducibility, and reliability in GaN-based HEMT devices. To date, not been much progress has been made in solving these trap related issues that influence rf-dispersion.

Ideally, bulk GaN substrates could reduce or eliminate the influence of trapping type defects on HEMT performance, especially traps associated with dislocations. However, during operation junction temperatures of HEMTs are greater than 200 ºC, which can lead to device breakdown and loss of linearity. This suggests that active cooling of the devices is potentially as important as reducing the influence of traps. Because SiC has a high thermal conductivity and is closely lattice matched GaN (3.5% difference) and AlN (< 1% difference), SiC is the best substrate for GaN HEMTs. To date the GaN HEMTs with the best power performance have been grown on SiC.

The main issue with GaN heteroepitaxy on SiC is that threading dislocations are formed in the GaN. As shown in Fig. 1, 100 nm of AlN is first grown on the SiC to provide nucleation sites and enhance two dimensional growth of the GaN. Growth of the AlN layer generates primarily edge type dislocations resulting from the discrete granularity of the AlN film. These edge dislocations can then propagate through the GaN and AlGaN films. While these dislocations are benign to transport in the 2-DEG they can limit the maximum source-drain voltage and provide shorting pathways within the device. Additional misfit dislocations can be generated at the AlGaN/GaN interface, especially when the Al concentration exceeds 30%. Techniques to reduce dislocations, such as epitaxial lateral overgrowth (ELOG), have not been extensively studied for improving HEMT performance.

Finally, there are many issues associated with the growth and characterization GaN HEMTs on SiC that have not yet been identified or addressed. In general, the growth and theory of how semi-insulating (SI) GaN is produced on SiC is not well controlled or understood. Surprisingly, some researches in the field have suggested that the GaN grain structure may play a pivotal role in achieving SI GaN. If this is the case, then reproducible nucleation of the GaN to replicate the same grain structure is absolutely necessary. Understanding of the physics behind the operation of GaN HEMTs is also lacking. This is primarily because physics measurements of the HEMT material properties are difficult and models of HEMTs with traps, dislocations, and surface charge have not been developed.

1.3 Technical Approach

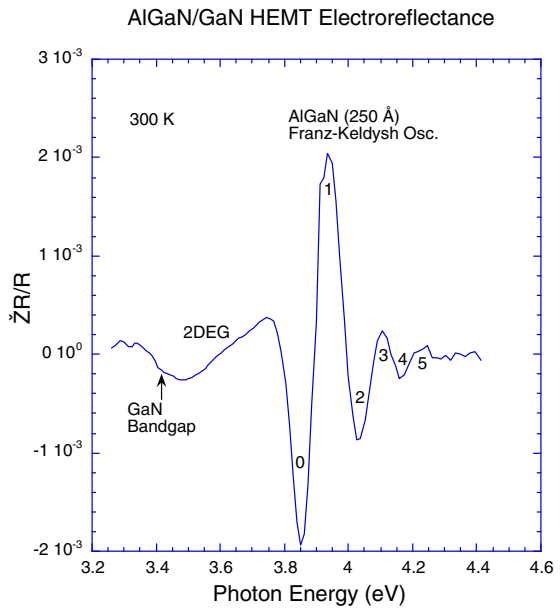

Fig. 1.2 First HEMT in-situ measurement of AlGaN electric field (0.41 MV/cm) and composition (16% Al) from Franz-Keldysh oscillations.

Fundamental experiments and calculations will be performed in parallel with HEMT growth, fabrication, testing, and equivalent circuit and thermal modeling. This approach will lead to a basic understanding of the mechanisms limiting HEMT performance, and identify "trouble spots" that need to be addressed through material improvement and device design. To ensure that our discoveries feedback to improve HEMT performance, we have assembled a team of senior solid-state material scientists, device physicists, and microelectronic engineers.

Initial experiments will investigate the influence of growth conditions on the GaN and AlGaN quality on SiC. The rapid feedback techniques of Hall mobility, x-ray diffraction (XRD), capicatance-voltage measurements (C-V), photoluminescence, and AFM will

be used to characterize GaN, AlGaN, and HEMT films. In addition, innovative photoreflectance and gated electroreflectance techniques are being developed to provide depth profiling of HEMT material quality and carrier densities. As shown in Fig. 1.2, we have recently demonstrated the usefulness of novel gated electroreflectance measurements to provide the first in-situ profiles of HEMT material composition, quality, and internal electric fields. HEMT device fabrication and testing will provide the most critical input toward optimizing the materials growth.

After establishing baseline materials growth and characterization, sources and locations of trapping type defects will be identified. Defect spectroscopies, which include photocapacitance, photoconductivity, deep level transient spectroscopy, e-beam injection, and H-passivation techniques will be used to identify and locate potential sources of traps. Density functional calculations will be correlated with DLTS and photocapacitance techniques in an effort to study electron trapping at dislocations and point defects to possibly identify the sources of these traps. Once identified, growth experiments will be conducted to remove these traps from the active regions of the devices. If the traps cannot be removed, their influence on the device will be mitigated, for example by dielectric passivation of the surface charge states, or by device design changes such as the use of recessed gates, which will require the development of non-damaging etch chemistries.

To reduce the influence of dislocations on the HEMT properties, GaN will be grown on cantilever patterned SiC. Recently, using cantilever epitaxy (CE) on patterned sapphire, we have achieved GaN with a dislocation density of $1x10^7$ cm^{-2}, which is 2-3 orders of magnitude lower than our standard GaN grown on planar sapphire. GaN growth on CE SiC will be optimized to both reduce dislocations and to maximize the thermal conductivity between the CE GaN and the SiC substrate. AFM and cathodoluminescence will be used to measure the reductions in dislocation density and TEM will be used to study the dislocation reduction mechanism. By producing HEMTs on CE GaN on SiC, the HEMT device physics can be studied for the first time with and without the influence of dislocations. Separate growth conditions, which minimize misfit dislocations at the AlGaN/GaN interface, will also be developed.

Growth reproducibility will be aided by unique in-situ diagnostics developed at Sandia. These in-situ diagnostics include optical reflectance, emissivity correcting pyrometry and the multi-beam optical stress sensor (MOSS). The use of optical reflectance to control the cantilever growth was instrumental in achieving GaN films with low dislocation densities. Correlation between the in-situ diagnostic signatures and the device and materials properties will ensure replication of HEMT growth structures. Since the quality of the SI GaN is critical to device pinchoff and frequency performance, experimental and theoretical studies will be conducted in order to identify how particular defects influence energy levels and contribute to the SI nature of GaN and AlGaN films.

In this LDRD, experimental and theoretical solid state studies along with device fabrication and testing will provide quality control and direct material growth activities to improve overall GaN HEMT performance. Our in-house materials program will be supplemented by device structures obtained through outside collaborations. By examining devices grown by alternative techniques (textured substrates or MBE for example) or with alternative substrates, we can test our hypotheses regarding connections between material growth, solid state properties and HEMT performance, providing additional direction to our overall Sandia effort**.**

1.4 Expected results

Specifically, we plan to identify and understand the material-based issues which are limiting GaN HEMT performance, and we will pursue material growth and device design-based solutions to solve these problems. These innovations will become the foundation of high performance, GaN-based microwave electronic technology at Sandia. The solutions that we acquire through research will guide both device development within Sandia and the choice of Sandia's collaborators from the greater GaN electronics community. We fully expect to solve many of the materials related issues that currently limit GaN HEMT device performance.

1.5 Creativity and Innovation

Our approach will combine Sandia's unique materials growth, modeling, and measurement capabilities to develop GaN HEMT devices on SiC. Over the years, several in-situ diagnostics have been developed at Sandia to measure compound semiconductor growth, including spectroscopic optical reflectance, emissivity correcting pyrometry and the multi-beam optical stress sensor (MOSS). The development of CE GaN on SiC substrates offers a unique solution to reducing dislocation densities in GaN keeping the excellent heat removal benefit of the SiC substrate. Novel characterization techniques, such as photoreflectance and gated electroreflectance, are being developed to provide depth profiling of HEMT material quality and carrier densities and to determine the location (AlGaN versus GaN, bulk versus surface), density, and origin of space charge and scattering in HEMTs. Along with dielectric passivation techniques, damage-free etches that currently do not exist for the nitrides will be developed for recessed gate technology, to minimize the influence of surface charge on HEMT performance.

1.6 Impact

Successful GaN microwave electronics is a disruptive technology that will have a huge impact in electronic sensors and communications in the 8-30 GHz frequency range by replacing vacuum electronics technology with solid-state electronics. The benefits of solid-state power are miniaturization, reduced cost, increased reliability, and reduced complexity. For example, miniaturization and weight reduction of synthetic aperture radars will allow radical new implementations based on conformal phased arrays that will open up the customer base for Sandia.

This LDRD is critical for many future programs at Sandia. Knowledge gained in this work will benefit the NW, ET, and MC SBUs in advancing GaN technology for remote electronic sensors such as SAR. Communications applications of GaN electronics are also important for the ET and MC SBUs. Sandia will also gain opportunities to impact critical DOD initiatives such as phased array radar upgrades associated with reconnaissance missions and national missile defense. By enabling 7-fold increases in power levels per aperture in the 8-12 GHz frequency bands, increased range and discrimination of phased array radars can be implemented without increasing aperture size and cost.

1.7 Tie to DOE

GaN-based solid-state microwave electronic devices are potential replacements for vacuum electronics technology in the 8 to 30 GHz frequency range. Using GaN-based microwave devices will allow weight and size reduction of synthetic aperture radars (SAR), RF MEMS, and communications applications of interest to NW, DS&A, and HS SMUs. This research will also impact DoD initiatives such as phased array radar associated with reconnaissance missions and national missile defense.

2. MOCVD growth of AlGaN/GaN HEMT Structures

2.1. Growth and characterization of MOCVD films

Films were grown using metalorganic chemical vapor deposition (MOCVD). For the research and HEMT structure growth two reactors were used as shown in Fig. 2.1. Nitride films were grown on c-plane sapphire or SiC using a custom designed, high speed rotating disk reactor (RDR) as shown in Fig. 2.1(a) or a commercial EMCORE short jar RDR reactor as shown in Fig. 2.1(b). Material growth was performed using metal-organic vapor-phase epitaxy in an EMCORE D-125 reactor with a short, jar geometry. In the short jar geometry, the wafer surface in located 3inches away from the surface of the injection flange.

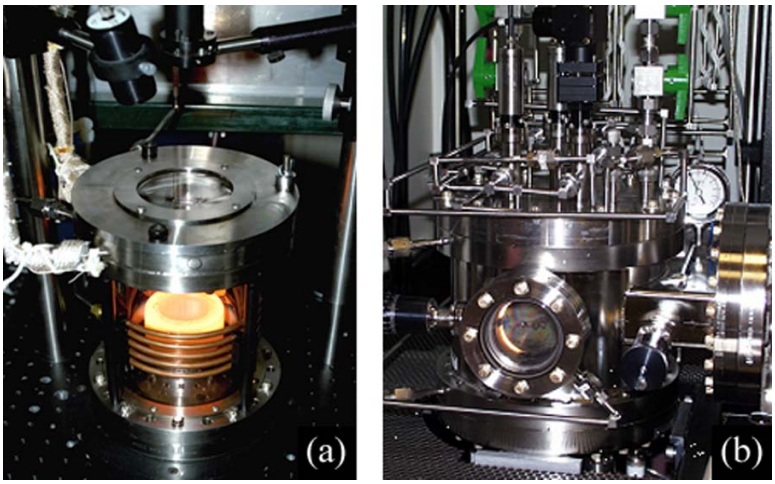

Fig. 2.1 Two MOCVD reactors were used for the studies and HEMT structure shown in this report. In (a) a custom RDR reactor developed at Sandia is shown and in (b) a EMCORE reactor (now Veeco) short jar RDR reactor used for the growth of the HEMT structures.

For both reactors the sapphire or SiC wafers were placed on a SiC coated graphite susceptor and the growth temperature was measured using optical pyrometry. Because both the substrates and the GaN films are transparent throughout the temperature range used, the optical pyrometer measures the temperature of the SiC coating the wafer rests on. This presents problems for obtaining absolute temperature measurement of the wafer. The growth conditions were monitored in-situ using an emissivity correcting pyrometer at 550 nm and a thermocouple [2.1]. The optical reflectance unit is a near-normal probe using a tungsten-halogen lamp [2.1]. The light from the tungsten-halogen lamp was delivered to the growth chamber via an optical fiber and focused onto the wafer surface. Similarly, the reflected light was focused onto an optical fiber and its intensity was measured using a Si photodiode detector equipped with a 10 nm bandwidth filter [2.1]. By modulating the tungsten-halogen light source, the light emission from the susceptor could be measured independently from the reflected light, allowing for emissivity corrected pyrometry [2.1].

The typical growth conditions would involve loading the wafers as received into the growth chamber, followed by heating in H_2 (and N_2) up to high temperature (>1050 ºC) to remove advantageous hydrocarbon material and oxides in the case of SiC. For the growth of the nitride material s trimethylgallium (TMGa), trimethylaluminum (TMAl), and ammonia (NH_3) were used in H_2 and N_2 carrier gas. The growth pressure, temperature, and reactant flow rates were varied during the course of the growth run, so specifics

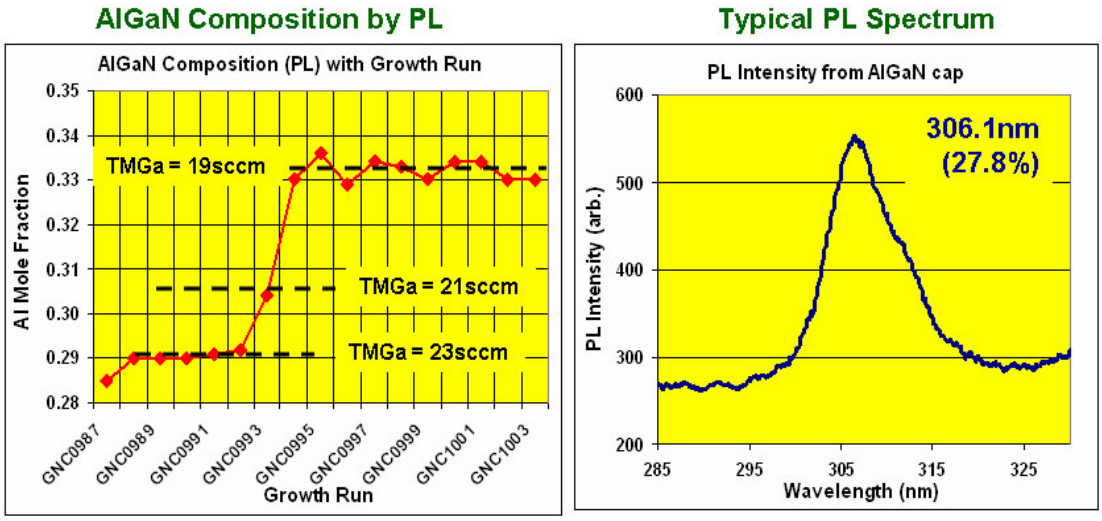

Fig 2.2. AlGaN composition measured using PL. In (a) the Al content is increased by decreasing the TMGa flow rates. In (b) a typical AlGaN PL scan is shown for an AlGaN film with 27.8% Al.

of the growth conditions are not given here but are presented with the reported results below. Sapphire wafers were used from two different vendors (Honeywell and Kyocera) with no discernable difference the the material quality. Silicon carbon wafers were used from three different vendors (Sterling, CREE, and II-VI) and the growth conditions had to be modified to produce the same HEMT structures and properties.

Table 2.1. Routine and Advanced Measurements Developed in the LDRD.

Routine Measurements	Advance Measurements
•Hall Measurements (300K) – Electron concentration and mobility – Now can do full wafer measurements •Capacitance-Voltage (C-V) – Pinch-off Voltage – Buffer resistivity – AlGaN thickness/composition •Atomic Force Microscopy (AFM) – Growth mode (2D-3D) •Contactless Sheet Resistance maps – Indicate variations across wafer •Photoluminescence – AlGaN composition	•X-ray Diffraction – Dislocation density, type • Electro-Reflectance – Study 2DEG and electric fields – AlGaN composition • Gated Hall Measurements (77-300K) – Investigate transport • Transmission Electron Microscopy – Dislocation density • Deep Level Spectroscopies – Electron traps in material

Composition measurements were routinely made using optical reflectance. Resulting composition measurements have been confirmed by x-ray diffraction and room temperature photoluminescence in selected samples and found to be within 3 mole percent. X-ray diffraction (XRD) measurements with (0004) and (10-11) reflections have been used to determine the dislocation density of dislocations with either a screw component or an edge component. Details of the XRD evalution of the materials are covered in Section 5. Transmission electron microscopy in both cross-section and plane view has been used to confirm dislocation density determined from XRD in selected films. The Al content in the AlGaN material was determined using both XRD and photoluminescence (PL). PL derived AlGaN composition measurements are shown in Fig. 2.2(a) for increases in the TMGa flow rate. An example PL spectrum is shown in Fig. 2.2(b) for a 27.8% Al content AlGaN layer. Electrical characterization included Hall effect to measure electron mobility and carrier concentration, Leheighton resistivity mapping to determine the resistivity of the GaN films and 2DEG, and capacitance-voltage (C-V) measurements to determine the carrier concentration in the 2DEG and pinch-off voltage. Examples of these techniques and more advanced characterization techniques developed in this LDRD are listed in Table 2.1.

2.2. Baseline GaN-based HEMT growth.

To improve GaN-based HEMT performance, "baseline" processes for both the material growth and device processing were first developed. Individual AlN, GaN, and AlGaN layers were grown on sapphire and SiC to confirm composition, growth rate and background impurity levels prior to the growth of full HEMT structures on SiC wafers. The nucleation of AlN on SiC and subsequent growth of the AlN epitaxial layer replicated similar processes that had been developed on sapphire. Ultimately, GaN-based HEMT processes with electron mobilities > 1300 cm^2/Vs, sheet charge > $1x10^{13}$ cm^{-2}, and sheet resistivity < 400 Ω/□, were developed. Fig. 2.2 shows the mobility and sheet charge for a series of growths, where minor changes in growth conditions were made to access the sensitivity of the transport properties to changes in the growth conditions. The electron mobilities and sheet concentrations measured in our baseline material compare favorable to those reported in the literature.

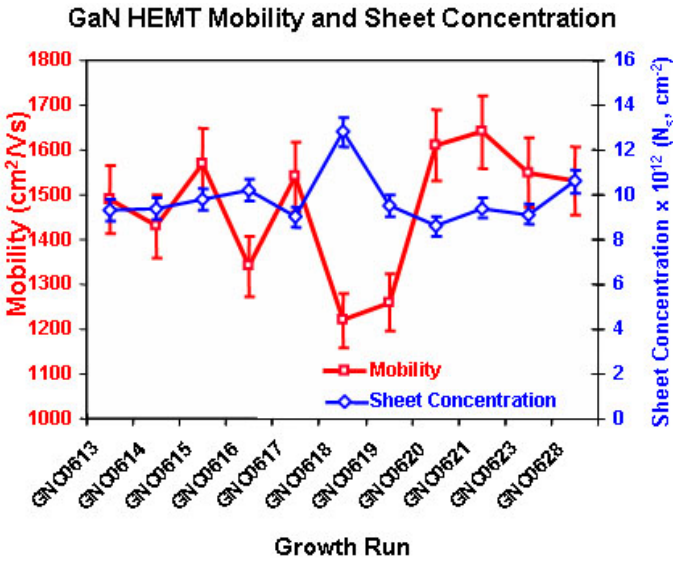

Fig. 2.3 Electron mobility of HEMT layers typically exceeded 1300 cm^2/Vs with a sheet charge > $1x10^{13}$ cm^{-2}.

With baseline processes established, several growth parameters were initially investigated to improve HEMT performance. Assuming that the initial microstructure is estab-

lished during the initial GaN growth on the AlN nucleation layer, variations in AlN thickness, growth temperature, and starting sequence of the nucleation and V/III ratio were studied, however little improvement over our starting baseline process was observed. Additional experiments found that the initial dislocation density is correlated to the GaN growth pressure, with high pressures producing GaN with fewer dislocations. For GaN growth at higher pressure the time spent in the 3D growth mode increases and this change in the morphology can be directly monitor using the in-situ optical reflectance measurements. By spending an increased time in a 3D growth mode at higher pressure the dislocation density was reduced as measured by x-ray diffraction. Though achieving a lower dislocation density is desirable, the semi-insulating (SI) quality of the GaN may be lost, resulting in inadequate device pinch-off.

Comparison of Vp in baseline HEMTs and recent structures.

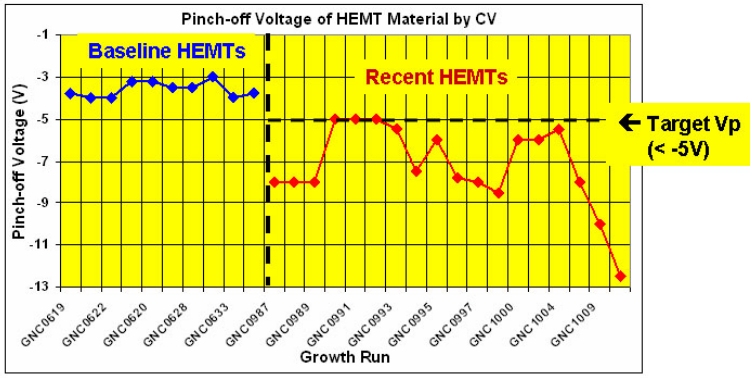

Fig. 2.4 Plot of the pinch-off voltage vs. the growth run number for the baseline HEMT structures and for films with a larger Al composition in the AlGaN.

Based on device results from our baseline material, it was determined that a more negative pinch-off voltage was required to compensate for the high temperature anneal of the ohmic contacts. By increasing the Al composition of the AlGaN top layer, pinch-off voltages exceeding –5V were achieved regularly. While maintaining the desired pinch-off voltage, improvements in the growth during the transition between GaN and AlGaN layers resulted in sheet resistances < 300 Ω/cm^2. A GaN capping layer has been shown in some cases to reduce gate leakage current. SiC substrates from several vendors have been tested over the past year, and significant differences in the surface polish between these vendors has been observed, especially for on SI SiC. Despite differences in the surface polish, HEMTs with similar pinch-off voltage and sheet resistance can be obtained. The key to achieving similar electrical properties in the HEMT layers will be modifying the AlN nucleation process to compensate for differences in surface polish and other surface morphology changes.

The baseline process for GaN HEMTs has been established. GaN active area mesas are patterned and etched by an inductively coupled plasma (ICP) system using a photoresist mask. The ICP power is kept to a minimum to inhibit buffer leakage currents. Next, ohmic contacts are patterned and deposited. Ti/Al/Mo/Au metal stack is used and alloyed at 850ºC for 30 seconds. The gate metal (Ni/Au) is next patterned and deposited. This brief sequence is used for quick HEMT feedback of GaN material. Optional steps to the baseline process include a transparent gate deposition for electroreflectance measurements, dielectric deposition for surface passivation, and airbridge metallization for multiple source and drain contacts, if characterization of multiple devices is desired.

2.3. Improving AlGaN growth

It is well known that the background concentration of carbon in GaN decreases with increasing growth pressure [2.2]. We have observed the same trend in 20-25% AlGaN films. Analysis by secondary ion mass spectroscopy (SIMS) showed a background carbon concentration of $6x10^{18}cm^{-2}$ for films grown at 75 torr. The concentration fell rapidly to $2x10^{17}cm^{-2}$ for growth at 300 torr and then more slowly to $1x10^{17}cm^{-2}$ for films grown at 400 and 500 torr. Generally, it is desirable to minimize impurity concentrations so growth at 300torr was selected. However, we have observed that both Al composition and growth rate decreased from 26% (2.1μm/hr) to 16% (0.25μm/hr) when the chamber pressure was increased from 75torr to 500torr respectively. The strong drop in Al incorporation and growth rate with increasing growth pressure is characteristic of parasitic, gas-phase pre-reactions that have been shown to generate nanoparticles above the wafer [2.3, 2.4].

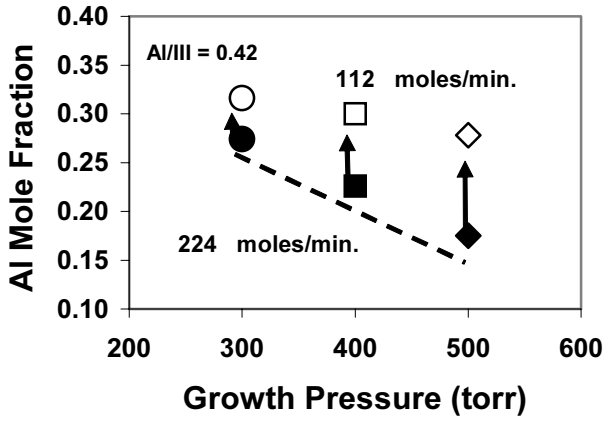

Fig 2.5. Al composition vs. growth pressure of AlGaN alloys grown with a fixed Al/group-III ratio of 0.42.

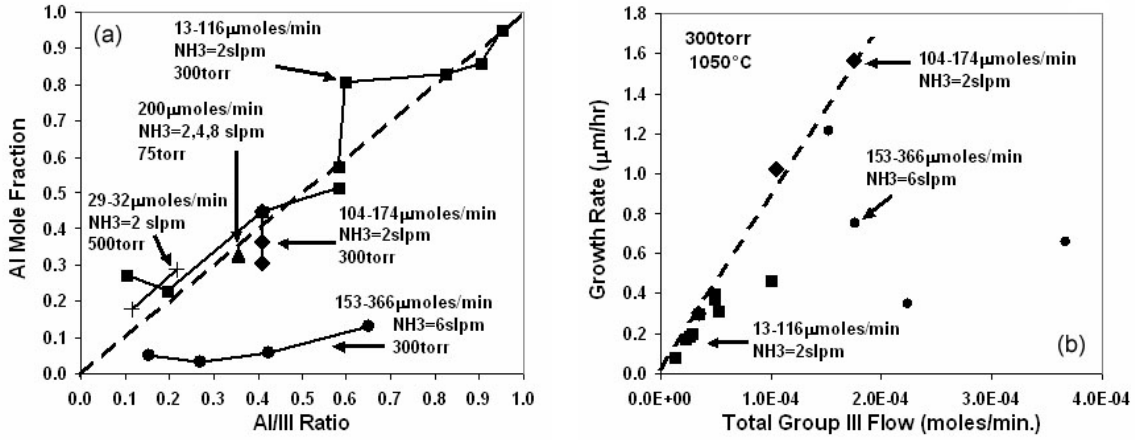

Fig. 2.6 (a.) Al mole fraction in the film vs. Al/group-III ratio in the gas phase. (b.) Growth rate vs. total group-III flux. Using lower group-III and (or) ammonia fluxes Al incorporation can be enhanced and a linear relationship between growth rate and group-III flux can be achieved. All lines are drawn as an aid to the eye.

Experiments to minimize parasitic, gas-phase reactions associated with increasing reactor pressure have been carried out to improve the Al incorporation efficiency and to

develop a linear relationship between growth rate and group-III flux. Such improvements should lead to better control of composition and thickness even if no improvement in material quality were obtained. In Fig. 2.5, the Al composition decreases with increasing growth pressure for a total group-III molar flux of 224 μmoles/min and a V/III ratio of 400. However, an increase in Al incorporation at all pressures while maintaining the same Al/III ratio can be achieved by simply reducing the total group-III flux in half as shown in Fig. 2.5. Hence, reducing group-III flux is a way to reduce parasitic, gas-phase reactions.

By using a lower group-III and/or ammonia flux, Al incorporation can be enhanced over the whole alloy range as shown in Fig 2.6. Under these conditions, the Al incorporation is linear with TMAl or TMGa flux, unlike the case shown in Fig. 2.6 where, at 300 torr and an ammonia flow of 6 slpm, the Al incorporation is sub linear with group-III flux. Even at 500 torr, Al compositions equal to the gas phase Al/III ratio can be achieved by using lower group-III fluxes. Growing films at 75 torr also result in efficient Al incorporation at higher group-III fluxes and incorporation that is independent of ammonia flow. The data points at 75 torr in Fig. 2.6 represent growth with ammonia flows of 2, 4 and 8 slpm and show no shift in Al composition. However, growth at 75 torr is also expected to result in a significant increase in carbon incorporation. The reduction in group-III flux can result in growth rates that could be unrealistically slow for growing thick buffers frequently used in LED structures (Fig. 2.6). However, useful growth rates can be achieved by increasing the group-III flux while still maintaining a linear relationship with group-III flux, even if Al incorporation is somewhat less efficient.

Fig. 2.7 shows a linear relationship between Al composition and growth rate as a function of total group-III flux at 400 torr and 970°C. This linearity holds for alloys from 30% to 80% even though the Al incorporation is not as efficient at 400 torr (Fig. 2.7). The previous discussion has been for films grown under conditions where the V/III ratio is typically less than 700 or at low pressures. However, efficient Al incorporation at 300 torr can

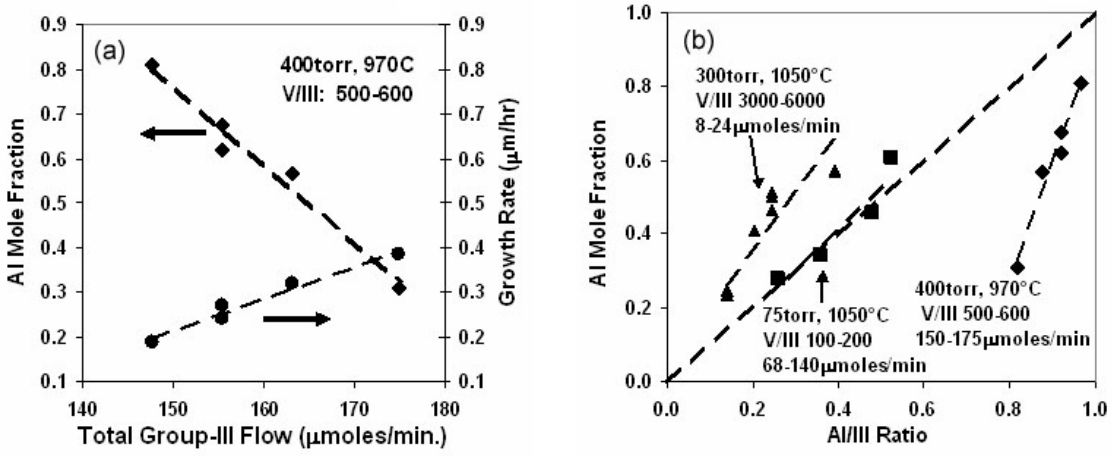

Fig. 2.7. (a.) Al mole fraction and growth rate vs. total group-III flux. (b.) Al mole fraction vs. Al/III ratio. All lines are drawn as an aid to the eye.

also be achieved at V/III ratios more typically used in the growth of GaN. By reducing the group-III flux to even lower levels, < 30μmoles/min for example, Al compositions can be similar to the gas-phase Al/III ratio for V/III ratios between 3000-6000 as shown in Fig. 2.7.

Growth conditions and the morphology of the nucleation layer influence the surface morphology of AlGaN films. Growth AlGAN on GaN films, which provide a relatively smooth template, can isolate the effect of growth conditions on surface morphology. Keller *et al.* [2.5] have reported that increasing ammonia flow increases the surface roughness of AlGaN films grown on GaN for high electron mobility transistor (HEMT) devices. We show a similar trend in surface morphology with increasing ammonia flow. Fig. 2.8 shows atomic force microscopy tapping mode images of $Al_{0.33}Ga_{0.67}N$ films (200-250Å) grown on GaN HEMT structures with different ammonia flows. All AlGaN films were grown at 300torr and 1050°C. In order to maintain a constant film composition while increasing the ammonia flow, the Al/III ratio was increased to compensate the reduction in Al incorporation due to parasitic gas-phase chemistry. As the ammonia flow was decreased from 6 slpm to 0.3 slpm, the rms roughness decreased from 0.91 nm to 0.26 nm and the terrace steps that were short and not well resolved with 6 slpm of ammonia become well defined with 0.3 slpm of ammonia. This improvement has been speculated to be the result of increased surface migration of Al adatom [2.5, 2.6] presumably due to the lower concentration of ammonia. However, similar well-formed terrace morphologies can be achieved under V/III ratios exceeding 5000 by using low group-III fluxes. Fig. 2.9 shows atomic force microscopy amplitude images of AlGaN films (200-250Å) grown on GaN with different ammonia and total group-III flows. Similar morphologies are observed for both the low ammonia, high group-III flux (NH_3=0.3 slpm, G-III=106 µmoles/min., specimen in Fig 2.9(a)) and the high ammonia, low group-III flux (NH_3=2 slpm, G-III=17 µmoles/min., specimen in Fig. 2.9(b)). Consequently, a lower ammonia concentration cannot solely be responsible for the observed improvement of surface morphology. However, improvements in surface morphology result from growth conditions that reduce parasitic gas phase reactions. While we initially expected improvements in controlling composition and

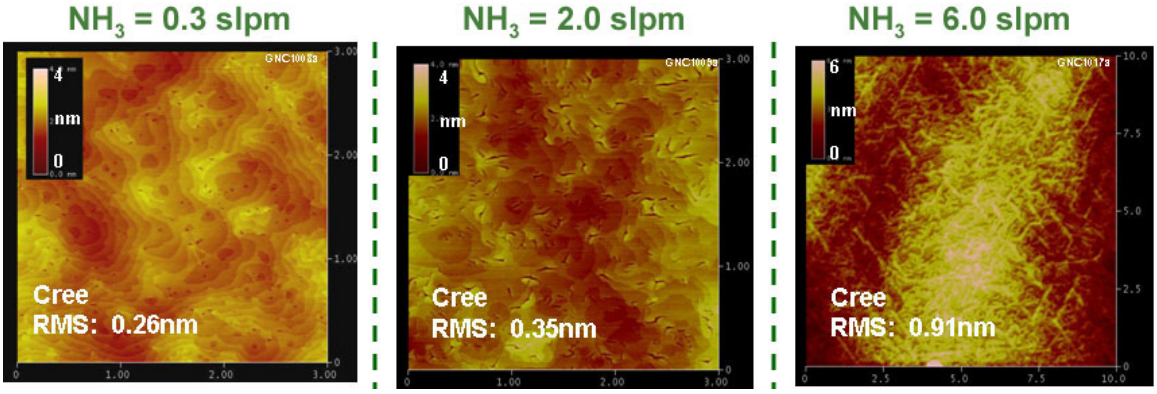

Fig. 2.8. Atomic force microscopy tapping mode images of 33% AlGaN films (200-250Å) grown on GaN with different ammonia flows. (a.) NH_3=0.3slpm, Al/III=0.44, V/III=124. (b.) NH_3=2slpm, Al/III=0.49, V/III=925. (c.) NH_3=6slpm, Al/III=0.49, V/III=3100. In order to maintain a constant film composition, the Al/III ratio was changed to overcome the parasitic gas-phase reactions which reduced Al incorporation with higher ammonia flow.

thickness by reducing parasitic reactions, it's possible that material quality, as reflected by improvements in terrace steps, is also improved. Further investigation between material properties and the presence of gas-phase parasitic reactions would be useful.

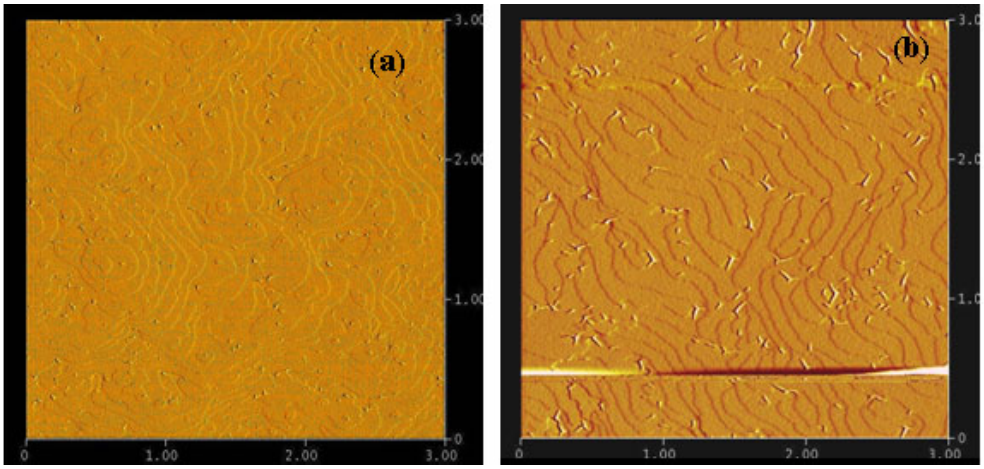

Fig. 2.9 Atomic force microscopy amplitude impages of AlGaN films (200-250 Å) grown on GaN with ammonia and total group-III flows (a) $Al_{0.33}Ga_{0.67}N$, NH_3 = 0.3 slpm, Al/III = 0.44, V/III = 124, group-III = 106 μmoles/min. (b) $Al_{0.29}Ga_{0.71}N$, NH_3 = 2.0 slpm, Al/III = 0.19, V/III = 5180, group-III = 17 μmoles/min.

The parasitic gas-phase reactions and nanoparticle formation identified by Creighton *et al.* [2.3, 2.4] could interact with the growth surface through some interaction with chemical byproducts from the nanoparticle generation or possibly by clusters of atoms small enough to reach the surface by diffusive transport. Since it is unlikely that byproducts of nanoparticle formation would be significantly different from reactions during epitaxial growth, we suggest the possibility that small clusters of atoms reach the growth surface and degrade surface morphology. Under conditions that yield a high rate of parasitic reactions (a combination of high pressure, group-III and ammonia flux) a higher concentration of clusters would be expected to reach the growth surface, resulting in reduced terrace widths and rougher morphology. Further investigations of the evolution of the growth surface and any interactions with parasitic gas-phase reactions are required to establish any active mechanisms.

2.4. Is smoother AlN on SiC better for HEMTs

HEMT structures grown on SiC typically use an AlN nucleation layer before growing the GaN and AlGaN devices layers. The electrical performance of HEMT devices can be influenced by the properties of the AlN nucleation layer. While transport properties of the initial baseline material achieved target goals, we sought to apply new knowledge of the growth of AlN that had been gained in developing deep UV LEDs. We investigated the growth of AlN films on SiC using significantly lower V/III ratios (i.e. N to Al ratio) around 10-100, ratios that resulted in much higher quality AlN films on sapphire substrates, while typical AlN nucleation layer used for HEMTs on SiC were grown with a V/III ratio of 1880 as shown in Fig. 2.10(a). In this AFM image the AlN terraces are pinned and rather narrow. This type of growth structure is believed to be a result of a high partial pressure of NH_3

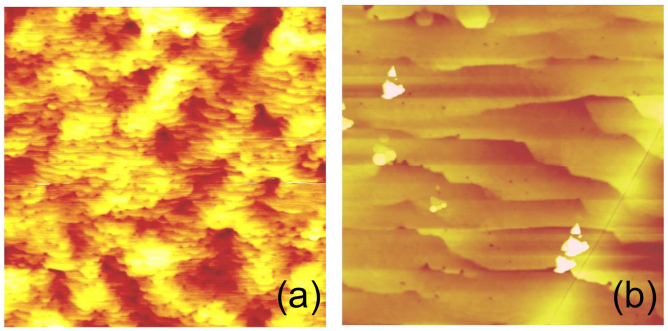

Fig. 2.10. Atomic force microscopy images of AlN films grown on SiC using a NH_3 to TMAl ratios of (i.e. V/III ratio) of (a) 1800 and (b) 11. The size of each image is 3 x 3 μm.

(high V/III ratio) that limits mobility of Al atoms on the growth surface. By lowering the NH_3 partial pressure (lower V/III ratio), increases in terrace width and reduced step pinning can be achieved as shown in Fig. 2.10(b). For this film the V/III ratio was 11, and cracks in the AlN are observed in the image. Cracking occurs for AlN films just 1000 Å thick, which is thinner than the typical 1000-1600Å used in HEMT structures. We concluded that while AlN films with lower V/III ratios result in better step structures and alignment to the underling SiC substrate, but they can not be used for HEMT development due to the tensile strain which increases during growth, leading to cracking. We are currently investigating AlN films initiated at high V/III ratios to relieve tensile stress, followed by AlN growth at a lower V/III to improve the AlN structure.

2.5. Evaluating SiC vendors and growth condition changes

During this LDRD project, SiC substrates from various vendors have been tested. The growth of SiC boules (especially semi-insulating) is very challenging and is still under development, however progress made in the last several years has been promising. In addition, more companies now produce sufficient quality SiC that the price for semi-

Table 2.2. Growth and structural changes in HEMT device material tested.

Growth and structure variables	Impact on device operation
AlGaN thickness	ohmic contact formation, pinch-off voltage
AlN growth temperature	electron mobility
GaN growth pressure	dislocation density
NH_3 flow used in AlGaN	growth mode and step structure
Growth transition between GaN and AlGaN layers	mobility, pinch-off voltage, current collapse

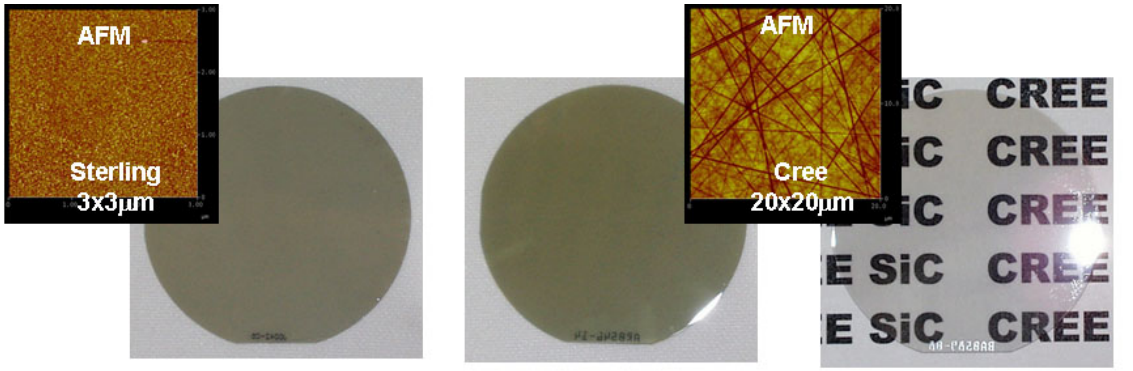

	Sterling (N+)	Cree (N+)	Cree (semi-insulating)
Polish:	Single Side	Single Side	Double Side (DSP)
Thickness:	254µm	270µm	400µm
Polytype:	6H	4H	4H
Price $/wafer:	165.00	300.00	3850.00

Fig. 2.11. Information on the Sterling and Cree wafers used for the growth of GaN-based HEMTs. Pricing information is of 2002.

insulating wafers is beginning to drop. In addition, several companies have achieved 3" SiC wafers with 4" wafers in the near future. As a result of the price decrease, material

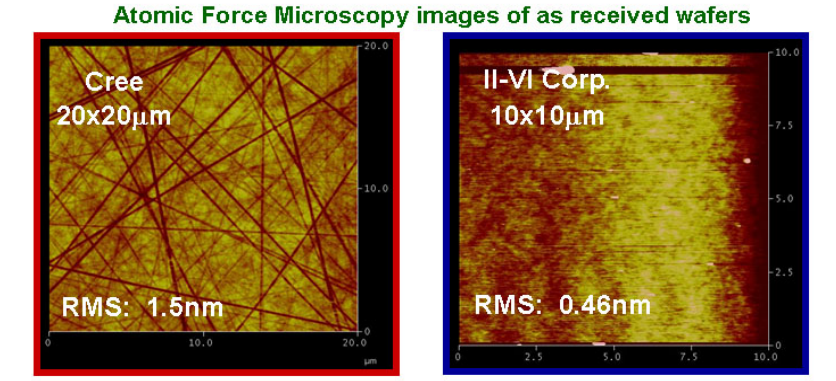

Pricing for SI-SiC wafers

CREE (4H, 430µm) :	$3200-4500 / wafer
II-VI Corp (6H, 270µm) :	$1000-1500 / wafer (Development) $2000-2500 / wafer (Prime)
II-VI Corp. (Reclaim):	$150 / wafer (samples to test at SNL)
Novasic (Reclaim):	Epi-growth was substandard.

Fig. 2.12. Atomic Force Microscopy images of SiC wafers received from (a) CREE and (b) II-VI Corporation. The RMS roughness is 1.5nm for (a) and 0.46nm for (b). Also shown is a price comparison of semi-insulating SiC wafers that were available in 2004.

from three vendors was evaluated by growing and testing HEMT structures on these different susbstrates.

As shown in the AFM images in Fig. 2.11 the wafer surface polish can vary substantially, and even vary between wafers from the same vendor. SiC wafers from Sterling appear to have a smoother surface polish when compared to CREE wafers. (Since these wafers were purchased from Sterling, Sterling has been purchased by Dow-Corning). Even though CREE is the largest supplier SiC wafers, the surface shows scratches from their polishing process and a relatively rough rms of 1.5nm which is possibly a concern for the growth of AlN and GaN films. In contrast, the material from both Sterling and II-VI Corporation are much smoother and scratch free, with the II-VI wafer having an RMS roughness of 0.46 nm as shown in Fig. 2.12.

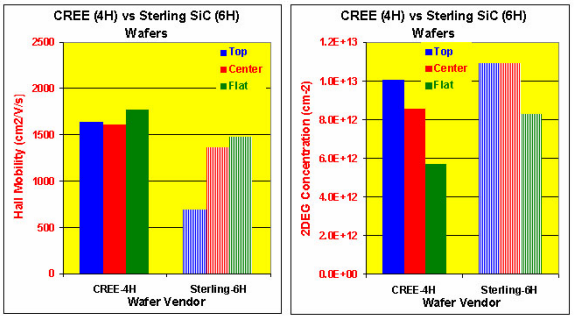

Fig. 2.13 Comparison of the electrical properties on Sterling 6H SiC wafers to Cree 4H SiC wafers

The first AlGaN/GaN HEMTs were grown on Sterling 6H SiC wafers which were n-type. After developing the growth process, we transitioned to Cree 4H SiC wafers because Cree had both n-type and SI wafers, which are needed for device isolation and rf testing of the final transistors. In transitioning from Sterling to Cree SiC wafers the AlN growth process needed to be changed. After optimization of the GaN material on the Cree SiC wafers the mobility increased 20-40 % and 2DEG carrier concentration decreasing slightly

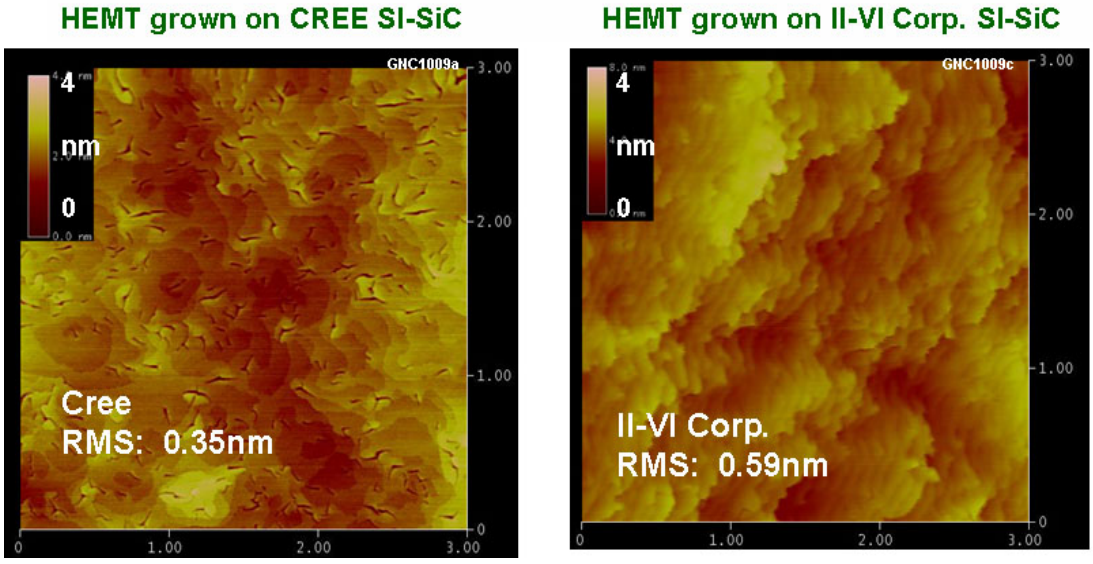

Fig. 2.14. AFM images of the surface morphology for AlGaN/GaN based HEMTs on SiC wafers from CREE and II-VI Corporation.

as shown in Fig. 2.13. The transconductance was also found to be 20-60 % larger on the Cree wafers compared to the Sterling wavers. These results suggest that the MOCVD growth process can be tuned to give greater flexibility in the choice of SiC vendor. Later SI SiC wafers from II-VI were used because of their lower cost compared to CREE. The surface morphology results of AlGaN/GaN HEMT structure grown simultaneously on CREE and II-VI wafers are shown in Fig. 2.13. Even though the surface polish is rougher on the CREE wafer compared to the II-VI wafer as shown in Fig. 2.12, the surface morphology of HEMT material grown on SiC from CREE is slightly smoother than material grown on SiC from II-VI Corporation as shown in the AFMs in Fig. 2.14. Even with the slight difference in the surface morphology the pinch-off voltage from CV and the sheet resistance showed no significant difference between the two wafers. The modifications of the AlN nucleation process that were developed in changing from the Sterling wafers to the CREE wafers can also be modified to improve the surface morphology of material grown on wafers from II-VI Corporation.

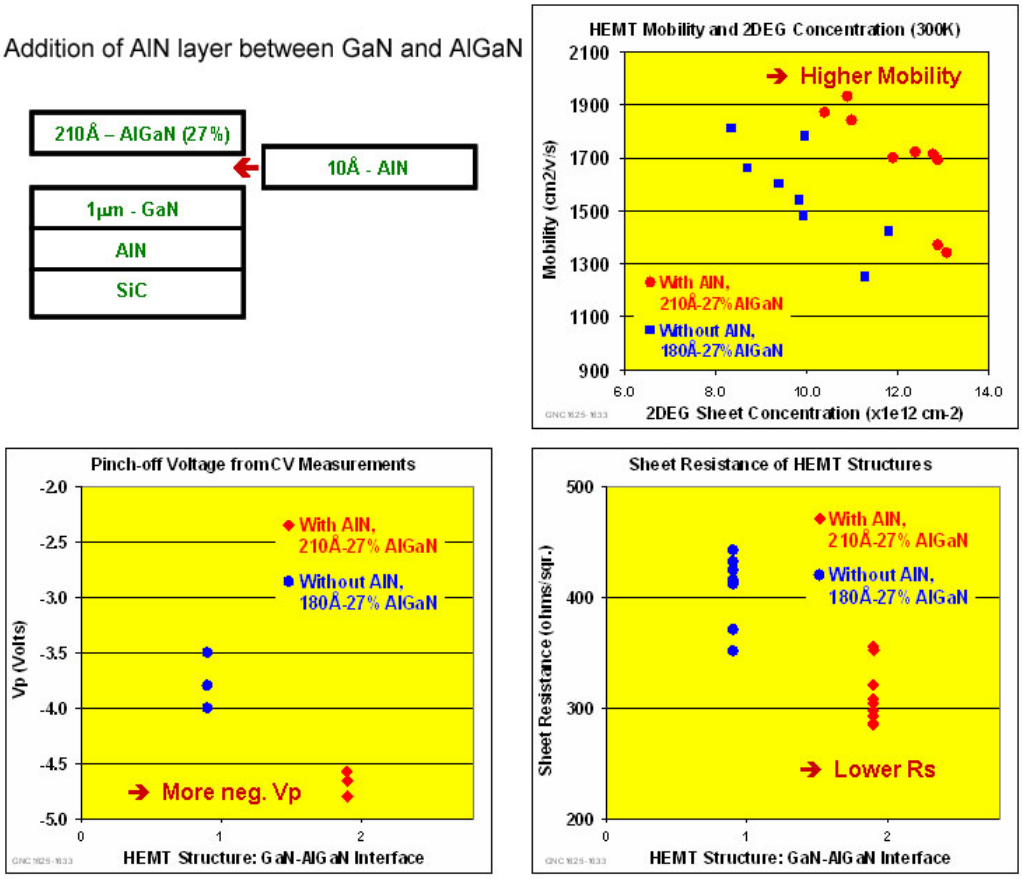

Fig. 2.15 Changes in the electrical properties are shown when a thin AlN layer is inserted between the GaN and AlGaN layers. The insertion of the AlN layer increases the electron mobility, decreases the pinch-off voltage and decreases the sheet resistance.

2.6. Insertion of AlN between the AlGaN and GaN layers

Following previous work by Smorchkova *et al.*, thin AlN layers were inserted between the AlGaN and GaN layers [2.7]. The thin AlN layer has two effects on the electrical properties. The first is to increase the electron mobility by reducing the alloy scattering from having the AlGaN placed directly on top of the GaN. The second is to increase the over all strain field on the GaN which increases the carrier density in the 2DEG layer. Both of these effects are seen in Fig. 2.15, where the higher mobilities, lower sheet resistivity and high pinch-off voltages are shown. Because of the increased strain near the GaN/AlN/AlGaN interfaces there is a greater risk of cracks forming unless the combined strain from these layers is kept below the critical thickness, which should be thinner for the combined AlN/AlGaN layer than for only AlGaN.

2.7. Summary of HEMT growth progress and electrical properties.

During this LDRD both the growth technology and the characterization technology were developed to routinely manufacture high quality HEMT wafers. The growth platform has some flexability especially when the SiC wafer polish changes. The routine use of XRD, C-V, Hall, and other characterization techniques listed in Table 2.1 allowed the optimization of AlGaN/GaN HEMT layers. Comparison of the electrical properties of the HEMT layers funded during this LDRD proposal and other workers in the field is shown in Fig. 2.16. As shown in Fig. 2.16 the HEMT results from Sandia compare very favorably with other groups working in the field. The data shown in Fig. 2.16 also show that the growth technology for these device structures is also maturing at a rapid rate, which should facilitate the fabrication of GaN-based microwave amplifiers in the near future.

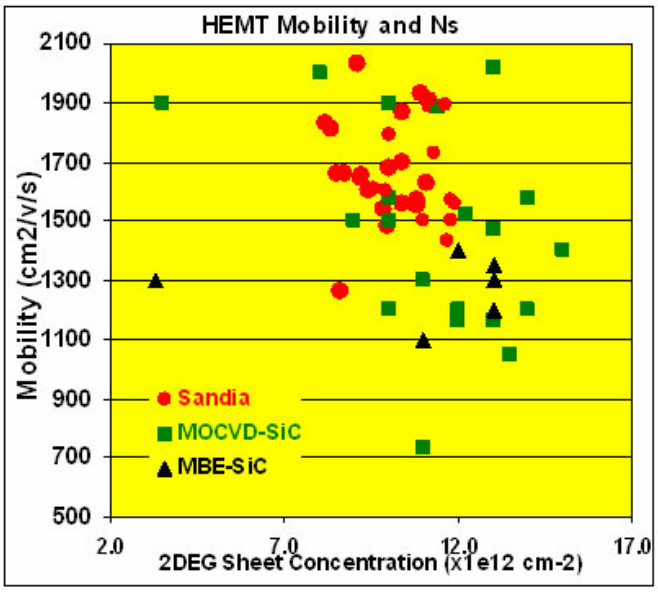

Fig. 2.16. The electron mobility is plotted vs. the 2DEG sheet carrier concentration. Improvments in the growth conditions led to the improved electrical properties.

Critical to the goals achieved in this LDRD were the quick and rapid evaluation techniques that were developed. However, these techniques applied on a routine basis also allow consistance checks on the material quality. As shown in Fig. 2.17 the dislocation densities measured using XRD are shown for 25 consecutive growth runs. Note that the

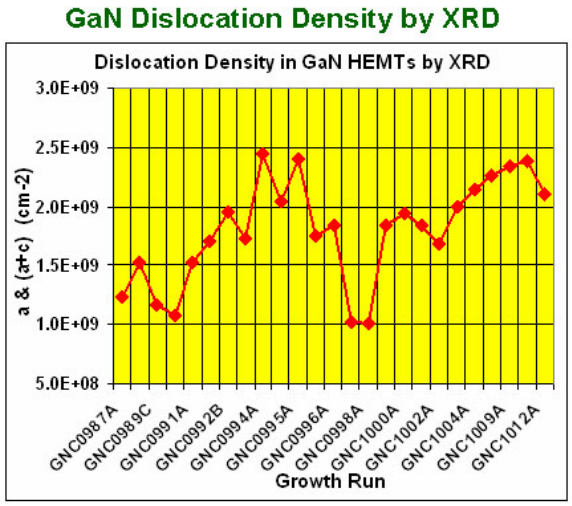

Fig. 2.17. The XRD measured dislocation is plotted for 25 consecutive growth runs.

dislocation density varies from 1.0×10^9 to 2.5×10^9 cm^{-2}. Fewer dislocations in the material might lead to the GaN not being insulating enough, while a greater number of the dislocation and the GaN material might be too resistive and contain too many trapping type defects. These consistant quality checks were critical to achieving the success demonstrated in this LDRD program.

2.8. References.

[2.1]. W. G. Breiland and K. P. Killeen, J. Appl. Phys. **78**, 6728 (1995).

[2.2]. 1 D.D. Koleske, A.E. Wickenden, R.L. Henry, M.E. Twigg, J. Cryst. Growth **242**, p55-69 (2002).

[2.3]. J. R. Creighton, W. G. Breiland, M. E. Coltrin and R. P. F. Pawlowski, Appl. Phys. Lett. **81**, 2626 (2002).

[2.4]. J. R. Creighton, G. T. Wang, W. G. Breiland, and M. E. Coltrin, J. Crys. Growth 261, 204 (2004).

[2.5]. S. Keller, G. Parish, P.T. Fini, S. Heikman, C.-H. Chen, N. Zhang, S.P. DenBaars, U.K. Mishra and Y.-F. Wu, J. Appl. Phys. 86, 5850 (1999).

[2.6] J. P. Zhang, A. Chitnis, V. Adivarahn, S. Wu, V. Mandavilli, R. Pachipulusu, M. Shatalov, G. Simin, J. W. Yang and M. Asif Khan, Appl. Phys. Lett. 81, 4910 (2002).

[2.7]. I. P. Smorchkova, S. Keller, S. Heikman, C. R. Elsass, B. Heying, P. Fini, J. S. Speck, and U. K. Mishra, Appl. Phys. Lett. 77, 3998 (2000).

3. Cantilever Epitaxy of GaN on SiC substrates

To reduce the influence of the abundant threading dislocations on the HEMT properties, GaN cantilever epitaxy (CE) was developed on SiC substrates. This follows the success of GaN CE on sapphire [3.1] for which Research Magazine R&D 100 award was given in 2004. In the CE work we achieved dislocation densities of $2x10^7$ cm^{-2} which is a factor of 10 lower than can be typically achieved for GaN growth on sapphire. These low dislocation densities were also achieved over large enough areas to place 1 mm^2 LED die on top of the CE wafers.

The advantages of using SiC substrates over sapphire are well documented. SiC has better thermal heat conduction than sapphire and is a better lattice match to AlN and GaN than sapphire. GaN films grown on sapphire tend to be under compression after cool down from the MOCVD growth, however on SiC the GaN films are under tension. This implies several consequences for the GaN CE growth on SiC as discussed below.

In Fig. 3.1 results are shown for the GaN CE on SiC substrates. In Fig. 3.1(a) the ICP etched SiC posts. To etch the posts the SiC is masked with sputtered Al and photoresist. The photoresist is patterned and developed. The lithographic pattern is etched using Cl-based

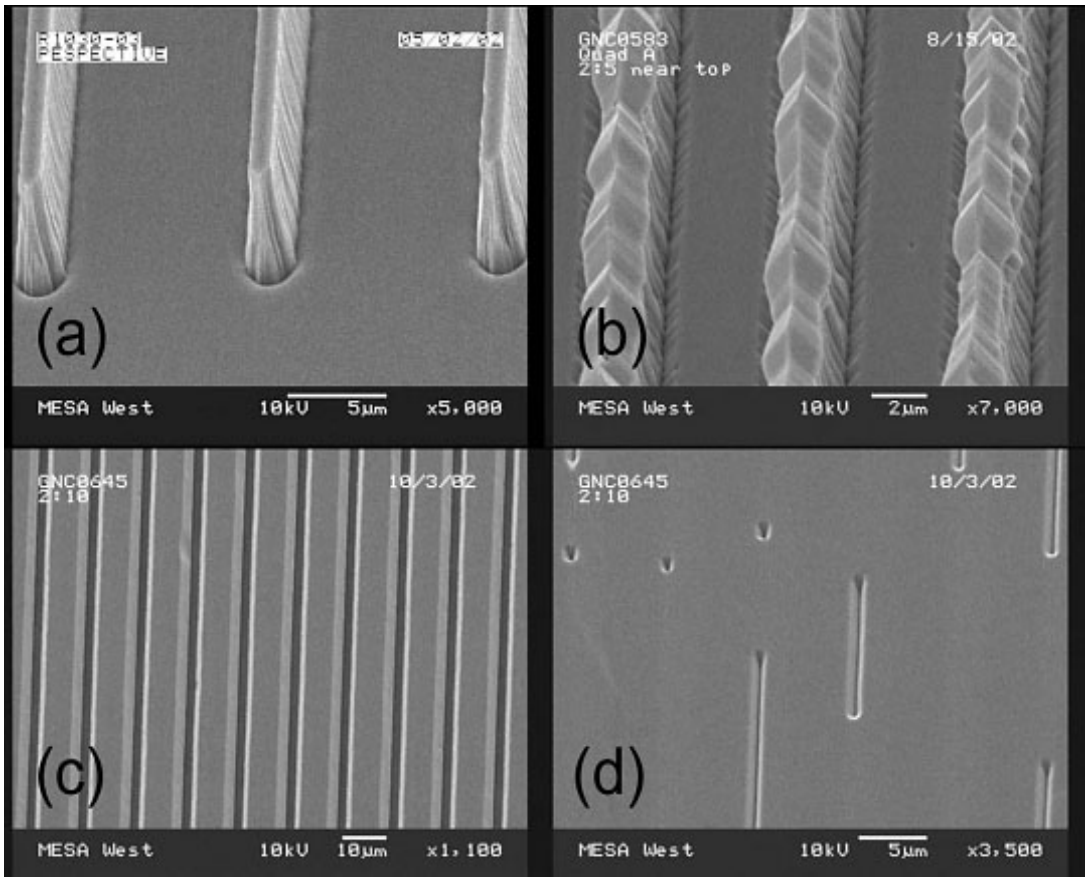

Fig. 3.1. SEM images of four stages of the GaN CE etching and growth on SiC. An SEM image of the (a) etched cantilever posts is shown, while in (b) growth of the pyramidal ridge is shown. Next (c) the initial cantilever wing is shown and finally (d) a nearly coalesced film is

chemistry to etch the Al and F- based chemistry to etch the SiC. Unlike sapphire, SiC is easier to etch and etch depths approaching 6 μm have been achieved. Micro masking caused by trace Al left on the surface before the F-based etch of the SiC occasionally occurs but is currently being addressed.

The GaN growth on the SiC is usually initiated using an AlN nucleation layer grown at high temperature. The pyramidal ridge and cantilever coalescence growth steps are directly transferable from what is currently done on sapphire [3.1] and images of the growth progression are shown in Fig. 3.1(b-d). Initially, the growth conditions are chosen to form a hexagonal ridge on top of the CE posts as shown in Fig. 3.1(b). Next the growth temperature is increased to 1100 ºC to increase the lateral growth rate so that the CE film can coalesce as shown in Fig. 3.1(c) and (d). One problem with the CE growth are the cracks that emerge in the GaN grown on the SiC, due to the tensile stress characteristic of the GaN films on SiC. Decreasing the cracking in the fully coalesced films would require stress management with the use of AlN interlayers [3.2]. While this would prevent the GaN film from cracking on the SiC, the subsequent growth of GaN on the AlN interlayer will create additional dislocations, thereby nullifying the advantage of using CE to reduce the GaN dislocation density. This was the main reason we did not pursue GaN CE growth on SiC further in this LDRD.

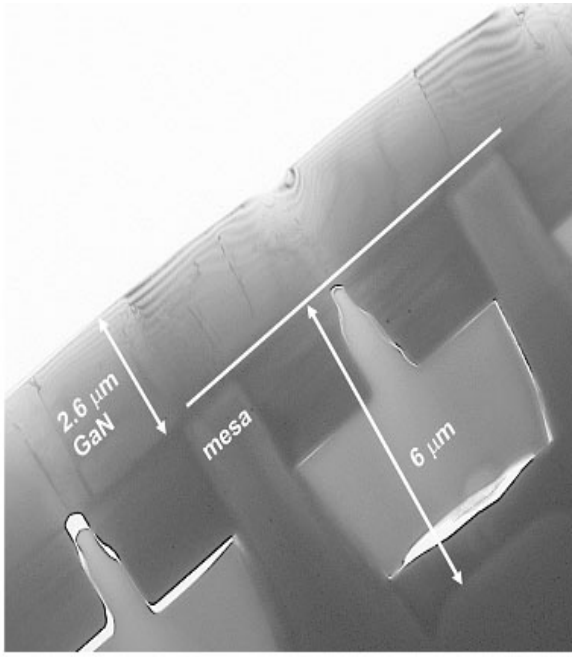

Fig. 3.2. Cross-section, bright-field TEM image showing mesas etched into SiC substrate and cantilever-epitaxial GaN grown at top.

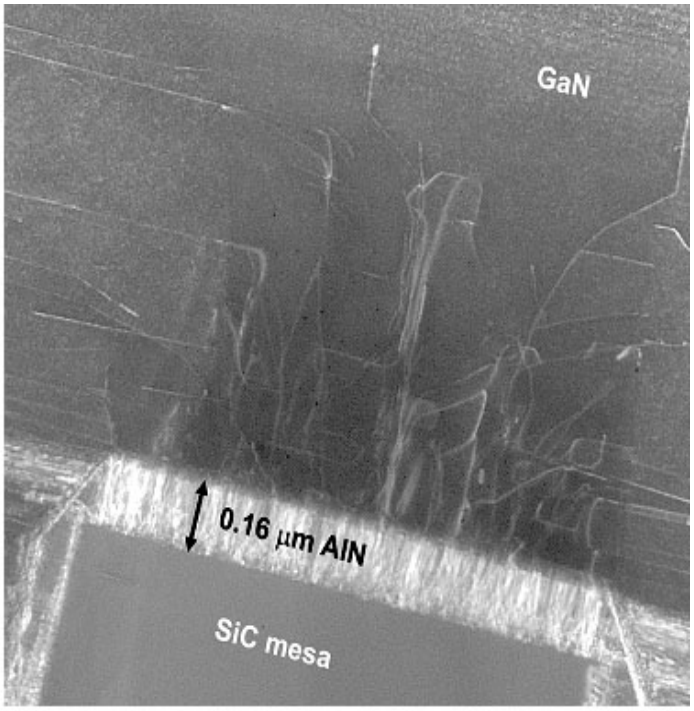

Fig. 3.3. Cross-section, weak-beam TEM image showing AlN nucleation layer over the mesa and threading dislocations in the GaN over the mesa. Approximately 2/3 of them are turned to horizontal, while 1/3 propagate vertically

Cross-section TEM was used to assess the GaN CE growth on SiC substrate. As seen in Fig. 2.2, deep trenches were easily etched into the SiC up to 6.0 μm deep. This is a huge advantage during GaN CE

growth since it allows greater flexibility in how the GaN growth parameters are varied during the growth and minimizes the interference from GaN that grows in the trenches. The mesas were found to be uniform in cross-section, 1.26 μm across. The GaN layer over the posts was grown to 2.6 μm thickness. There was also a thick, unwanted undergrowth of GaN laterally from the sides of the posts that contained many lateral dislocations, but it appears not to have caused serious detrimental effects in the GaN overlayer.

The GaN layer that grows on top of the AlN layers contains numerous vertical threading dislocations (VTDs) over the mesas, as seen in the higher magnification images in Fig. 2.3. Several such images showed that 2/3 of the VTDs over the mesa were turned to horizontal, with the remaining 1/3 propagating toward the surface. The bright layer immediately over the SiC mesa is the 0.16 μm-thick AlN nucleation layer. The vertical lines within it indicate a very high density of dislocations, which fortunately do not all propagate into the GaN grown upon it. AlN also nucleates on the sides of the mesas, apparently leading to the lateral undergrowth.

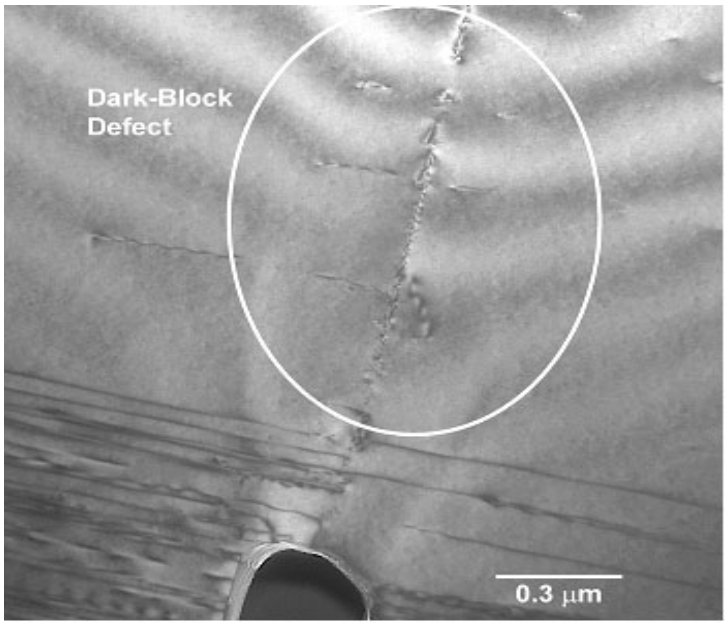

Fig. 3.4 Defects seen at the coalescence between two cantilevers. An array of lateral dislocations surrounds the coalescence, which is expected to produce a dark-block defect that would not emit light.

Many of the coalescences between adjacent cantilevers are defective, as seen in Fig. 3.4. In some cases, a crack was found between cantilevers that were not completely coalesced. Lateral dislocations are seen on either side of the defective coalescence seam. These arrays appear like those found at defected coalescences in CE-GaN grown on sapphire, and thus we expect they are non-radiative similar to the "Dark-Block Defects" that we have observed on GaN CE on sapphire [3.3]. Because of the large density of defective coalescences and the propensity of the GaN CE to crack on SiC substrates, we decided not to further investigate using GaN CE to reduce the dislocation density in operations HEMT devices.

3.1 References.

[3.1]. C. I. H. Ashby, C. C. Mitchell, J. Han, N. A. Missert, P. P. Provencio, D. M. Follstaedt, G. M. Peake, and L. Griego Appl. Phys. Lett. 77, 3233 (2000).

[3.2]. H. Amano, M. Iwaya, T. Kashima, M. Katsuragawa, I. Akasaki, J. Han, S. Hearne, J. A. Floro, E. Chason, J. Figiel, Jpn. J. Appl. Phys. Part 2 (Letters) **37**, L1540 (1998).

[3.3]. P. P. Provencio, D. M. Follstaedt, N. A. Missert, D. D. Koleske, C. C. Mitchell, A. A. Allerman, C. I. H. Ashby, Mat. Res. Soc. Symp. Proc. **743**, 115 (2002).

4. Impurity incorporation into the group III-nitrides

4.1 Density functional theory calculations of oxygen impurities in GaN

Density-functional theory [4.1] and the generalized-gradient approximatiom [4.2] for exchange and correlation were used to compute energy-minimum configurations and formation energies of substitutional and interstitial oxygen (O) in wurtzite GaN. The results indicate that O substituted at an N site (O_N) acts as a single donor with the ionized state (O_N^{+1}) being the most stable O state in *p*-type GaN. In *n*-type GaN, interstitial O (O_I) is predicted to be a double acceptor and O substituted at a Ga site (O_{Ga}) is predicted to be a triple acceptor. The formation energies of these two species are comparable to that of O_N in *n*-type GaN and, as such, they should form and compensate the O_N donors.

The extent of O_N compensation by O_I and O_{Ga} was estimated for a total O concentration of $10^{17}cm^{-3}$ and both Ga- and N-rich conditions. Ga-rich conditions yielded negligible compensation with an O_N concentration in excess of $9.9\times10^{16}cm^{-3}$. N-rich conditions yielded a 25% lower O_N concentration, due to the increased stability of O_I and O_{Ga} relative to O_N, with a moderate amount of compensation. The dependence of the O_N concentration on the total amount of O was also examined. For a total O concentration of $10^{18}cm^{-3}$ and Ga-rich conditions, the O_N concentration was estimated to be $8.7\times10^{17}cm^{-3}$, indicating increased compensation relative to that arising with an O concentration of $10^{17}cm^{-3}$. Overall, the theoretical results are consistent with experiments indicating that O acts as a donor in GaN(O) [4.3, 4.4, 4.5]. The prediction of an O acceptor state supports the findings of Chung and Gershenzon [4.4] who detected such a state in their samples.

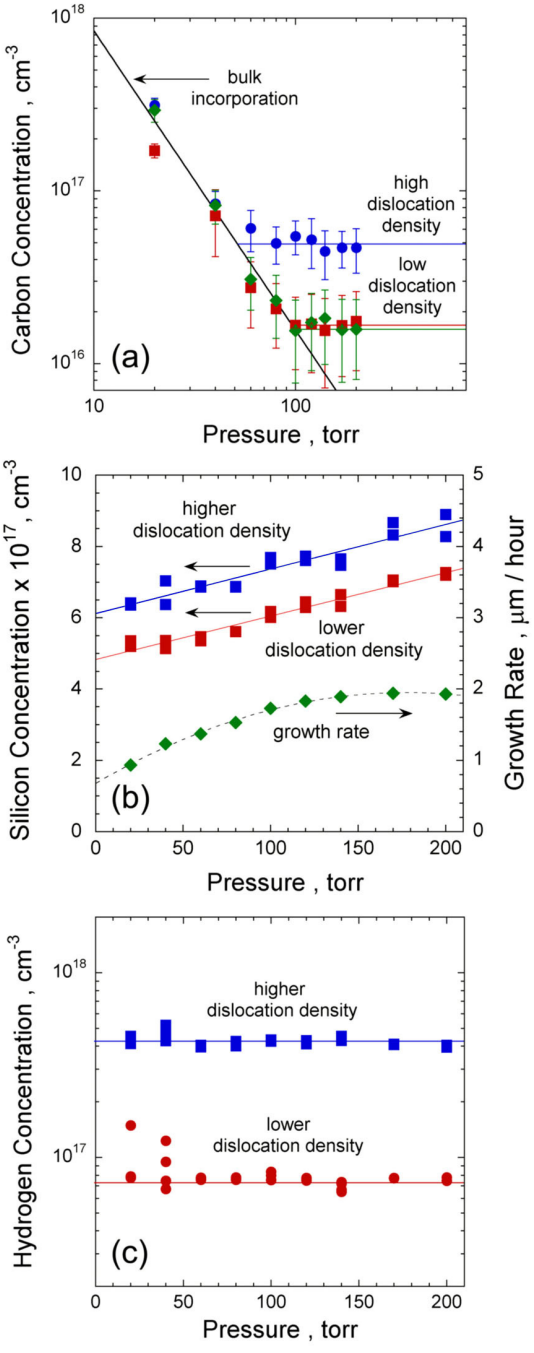

Figure 4.1. The (a) carbon, (b) silicon, and (c) hydrogen impurity incorporation as a function of growth pressure for films with both high and low dislocation density. The GaN growth rate is also plotted along the right y-axis in (b).

Complexes of O_N with the Mg acceptor and O_I with the Si donor were examined. Binding energies for charge-conserving reactions were ≥ 0.5 eV, indicating that these complexes can exist in equilibrium at room temperature. Complexes of O_N with the Ga vacancy (V_{Ga}) in *n*-type GaN were also examined and their binding energies were 1.2 and 1.4 eV, indicating that appreciable concentrations can exist in equilibrium at elevated temperatures. This conclusion is consistent with results from positron annihilation studies which indicate that O contamination enhances the formation of V_{Ga} [4.6, 4.7].

4.2 Density functional theory calculations of carbon impurities in GaN

Density-functional theory has been used to identify atomic configurations for carbon (C), and to determine formation energies for these configurations as a function of Fermi level and growth stoichiometry. Both substitutional and interstitial configurations were identified, with all of these states displaying electrical activity and associated defect energy levels in the gap. The energetically favored state for each species was found to depend strongly on Fermi level. The lowest energy state of C, for example, was found to be a substitutional N site in *n*-type material and either a substitutional Ga site or an interstitial site in *p*-type material, depending on the growth stoichiometry. Carbon was found to assume a variety of interstitial configurations and to produce defect energy levels deep within the gap. These defect levels can act as electron traps and may be detrimental to HEMTs.

4.3 SIMS investigation of impurity incorporation in GaN films

Carbon is related to one of the deep electron traps in bulk GaN and may be responsible for compensating the n-type background in GaN. Carbon has been shown to produce electron traps in GaN and may be responsible for producing the desired insulating character [6.8]. Carbon incorporation into GaN thin films typically comes from incomplete removal of the methyl groups from the Ga precursor.

For GaN films grown on sapphire the carbon incorporation may depend on whether it incorporates into the bulk or at dislocation cores. Evidence for these two different incorporation schemes is shown in Fig. 6.1(a). For this data the same growth run was repeated on one high (~$5x10^9$ cm^{-2}) and two low (~$8x10^8$ cm^{-2}) dislocation density substrates. The growth pressure was changed for each value shown followed by SIMS measurements to obtain the C concentration [4.9]. At low pressure the carbon incorporation increases as the growth pressure is decreased for both levels of dislocation density. As the growth pressure is increased the low dislocation substrates produce a carbon level of $1.5x10^{16}$ cm^{-3} while the higher dislocation density substrate produce a larger carbon level of $5x10^{16}$ cm^{-3}. At higher growth pressures etching mechanisms exist for the removal of carbon from the surface [4.9, 4.10]. This work suggests that C favors incorporation near dislocations at high growth pressures and can incorporate at both bulk and dislocations sites at lower growth pressures or possibly C solubility enhancement at dislocations. This work demonstrate the ability to tune the carbon level in the GaN film and thus either increase or decrease the carbon level to produce the desired electronic properties.

The silicon and hydrogen levels are also shown in Figs. 4.1(b) and (c) as a function of the growth pressure. Note that for light silane doping flows, the Si level increases as the pressure increases. This increase in the Si level coincides with a pressure induced increase in the growth rate. Also note that substrate with the higher dislocation density appears to have a slightly larger Si concentration than the lower dislocation density substrates, suggesting that Si incorporation might be more favorable around dislocation cores. The overall trend in the increase in the Si level as the growth rate increases was previously observed [4.9]. The hydrogen incorporation, on the other hand, appears to be constant as a function of pressure. While carbon is a deep acceptor or n-type compensator and silicon is an n-type dopant, the role of hydrogen in GaN electrical properties is somewhat unclear.

4.4 Electrical properties of GaN with different Si and C concentrations.

Prior research at Sandia National Laboratories on the effects of carbon impurities has been used to further understand the possible role of this impurity in HEMT devices grown on GaN. These devices typically employ a GaN layer grown under conditions which promote semi-insulating behavior. But these same growth conditions have been also shown to result in enhanced incorporation of carbon. In recent Sandia research on such layers, capacitance-voltage measurements showed different electrical behavior for high and low C concentration [4.11]. At low concentrations, the material was partly compensated while at high carbon concentration the material was semi-insulating. Density Functional Theory (DFT) calculations were able to explain these observations. At low concentrations, carbon substitutes for nitrogen and acts as an acceptor that compensates the Si donors. At concentrations exceeding the Si dopant level, carbon incorporates as an acceptor at nitrogen sites and as a donor at gallium sites, thereby rendering the material semi-insulating. The source of a blue luminescence peak in high C concentration material is then attributed to a transition between the C donor and the C acceptor states; and the temperature dependence of this peak is consistent with the donor to acceptor transition. Our work in the past year on these same samples has revealed the existence of metastable changes in this blue luminescence, and in the commonly observed yellow luminescence band which also appears to be strongly linked to the presence of carbon in GaN. Since the current collapse in GaN HEMTs is also a result of metastable changes in the electronic properties of the GaN active layer, understanding the role of carbon in this metastability could shed light on the this feature of HEMT performance.

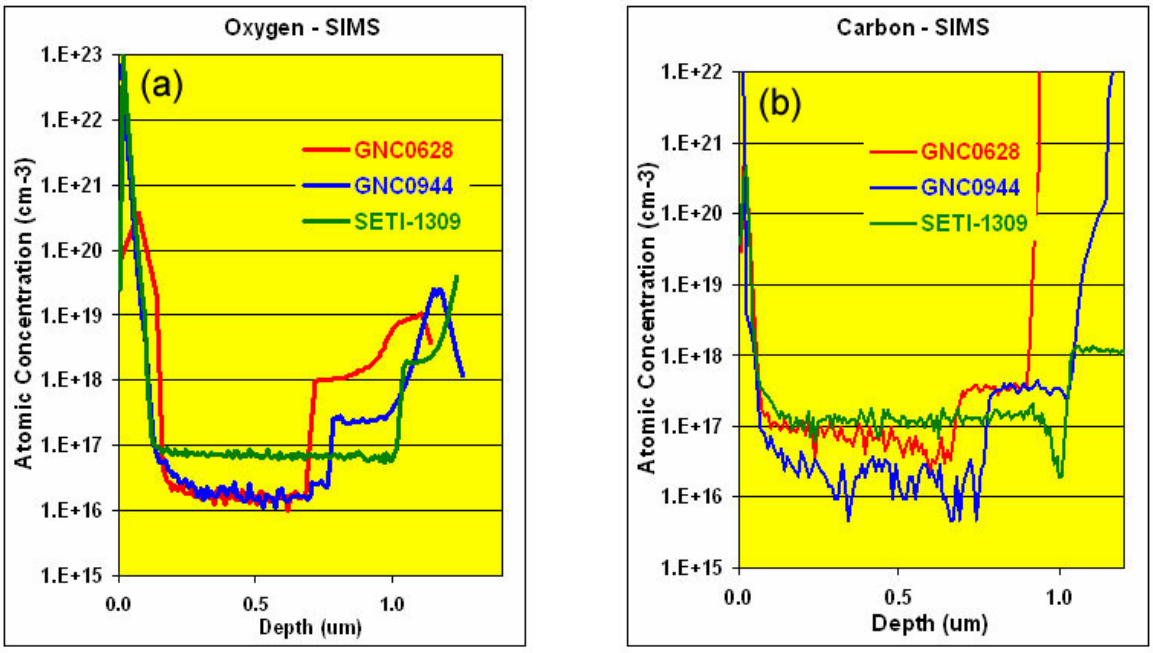

Fig. 4.2 Comparison of (a) oxygen and (b) carbon impurity levels in HEMT layers from SNL and HEMT wafers purchased from SETI

4.5 Comparison of impurities in HEMTs grown at SNL and SETI.

The oxygen and carbon levels were measured in GaN HEMT layers grown at SNL and at Sensor Electronic Technology, Inc. (SETI) located in Columbia, South Carolina. SIMS profiles are shown for (a) oxygen and (b) carbon in Fig. 4.2. Oxygen is known as an n- type dopant [4.12] in GaN while carbon is a deep acceptor or an electron trapping type defect which may contribute to compensation of the residual n-type background donors [4.11]. Note that the oxygen level is lower in the SNL material reach a level near $2x10^{16}$ cm^{-3}, while the material from SETI has oxygen levels that are $8x10^{16}$ cm^{-3}. The carbon levels are also lower in the SNL material shown in Fig. 4.2(b) compared to the SETI material. The higher carbon in the SETI material may be needed to compensate the higher levels of oxygen in order to achieve insulating GaN. Over time both the n-type and compensating carbon levels should be lowered to achieve more intrinsic, insulating material. As shown in Fig. 4.1(a) this will require lower dislocation density substrates as well as higher growth pressures to reduce the carbon levels and reduced oxygen ammonia and metalorganic precursors.

4.6 Dislocation Density and Carbon Content

The level of background carbon incorporated during the growth of GaN films is a key parameter for growth of successful HEMTs. An excessive amount of carbon (>5e17cm^{-3}) can result in excessive electronic trapping and too little will result in devices that do not pinch-off. The lower level of carbon is dependent on the background impurity level and is highly dependent on the starting purity of the source material and reactor integrity. It is well known that increases in growth pressure can result in lower levels of carbon incorporation

and lower threading dislocation. While lower dislocation densities are desirable, an upper limit in growth pressure is determined by the minimal level of carbon necessary to achieve device pinch-off. Recently, we have investigated the level of carbon in undoped GaN films as a function of growth rate as well as pressure. The intent was to decouple the relationship between dislocation density and growth pressure with carbon concentration and growth pressure. Fig. 4.3 shows the concentration of carbon in GaN grown at different pressure and TMGa flux. As expected, the level of carbon is inversely related to growth pressure. However, the level of carbon incorporated at a given pressure can be independently adjusted by varying the TMGa flux. Currently, we are in the process of growing HEMT devices with a sufficiently large enough carbon level for device pinch-off, while keeping the growth pressure higher for lower dislocation content. As expected, the level of carbon is inversely related to growth pressure. However, the level of carbon incorporated at a given pressure can be independently adjusted by varying the TMGa flux as shown in Fig. 4.3. Thus, we are in the process of growing HEMT devices with a sufficiently high carbon level that leads to device pinch-off, while growing at higher pressures that lowers the dislocation density.

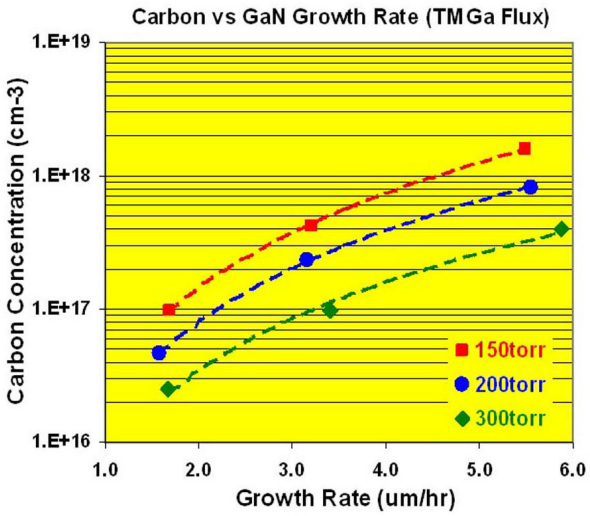

Fig. 4.3 Carbon concentration is plotted vs. the GaN growth rate. The data points represent different growth pressures.

4.7 References

[4.1]. W. Kohn and L. J. Sham, Phys. Rev. **140**, A1133 (1965).

[4.2]. J. P. Perdew, in Electronic Structure of Solids '91, edited by P. Ziesch and H Eschrig (Akademie, Berlin, 1991), p. 11.

[4.3]. W. Siefert, R. Franzheld, E. Butter, H. Sobotta, and V. Riede, Cryst. Res. & Technol. **18**, 383 (1983).

[4.4]. B-C. Chung and M. Gershenzon, J. Appl. Phys. **72**, 651 (1992).

[4.5]. C. Wetzel, T. Suski, J. W. Ager III, E. R. Weber, E. E. Haller, S. Fischer, B. K. Meyer, R. J. Molnar, and P. Perlin, Phys. Rev. Lett. **78**, 3923 (1997).

[4.6]. K. Saarinen, P. Seppälä, J. Oila, P. Hautojärvi, C. Corbel, O. Briot, and R. L. Aulombard, Appl. Phys. Lett. **73**, 3253 (1998). See also O. Briot, J. P. Alexis, S. Sanchez, B. Gil, and R. L. Aulombard, Solid State Electron. **41**, 315 (1997).

[4.7]. J. Oila, V. Ranki, J. Kivioja, K. Saarinen, P. Hautojärvi, J. Likonen, J. M. Baranowski, K. Pakula, T. Suski, M. Leszczynski, and I Grzegory, Phys. Rev. B **63**, 045205 (2001).

[4.8]. P. B. Klein, S. C. Binari, K. Ikossi, A. E. Wickenden, D. D. Koleske, and R. L. Henry, Appl. Phys. Lett. **79**, 3527 (2001).

[4.9]. D. D. Koleske, A. E. Wickenden, R. L. Henry, M. E. Twigg, J. Crystal Growth **242**, 55 (2002).

[4.10] D.D. Koleske, A. E. Wickenden, R. L. Henry, J. C. Culbertson, M. E. Twigg, J. Crystal Growth **223**, 466 (2001).

[4.11]. C. H. Seager, A. F. Wright, J. Yu and W. Götz, J. Appl. Phys. **92**, 6553 (2002).

[4.12]. W. J. Moore, J. A. Freitas, Jr., G. C. B. Braga, R. J. Molnar, S. K. Lee, K. Y. Lee, and I. J. Song, Appl. Phys. Lett. **79**, 2570 (2001).

5. XRD measurement of dislocation density

The growth of GaN on sapphire or SiC results a high density (10^8 to 10^{10} cm^{-2}) of vertical threading dislocations. These dislocations are typically detrimental to the electronic and optical properties of GaN films, however in HEMT type layers screening of the dislocation's electric field apparently reduces some of the electron scattering in a 2DEG [5.1]. However, higher electron mobility is typically observed in films that have a lower overall dislocation density [5.1].

During the course of this LDRD a reciprocal-space model was developed that describes the (*hkl*) dependence of the broadened Bragg peakwidths produced by x-ray diffraction from a dislocated epilayer. The model was compared the model to experiments and find that it accurately describes the peakwidths of 16 different Bragg reflections in the [010] zone of both GaN and AlN heterolayers. By using the lattice-distortion parameters determined by fitting the model to selected reflections, we can now estimate threading-dislocation densities for GaN, AlGaN, and AlN samples. The dislocation density estimates from XRD were compared to TEM measurements and good agreement was observed between these two techniques. Using this XRD technique allows for rapid feedback for improving the growth conditions in as little as 1 hour.

5.1 Description of the XRD method for dislocation determination.

One promising option is nondestructive measurement of the dislocation density by x-ray diffraction (XRD), a technique first used to measure dislocation densities in plastically deformed metals in the 1950s [5.2 – 5.5]. In the mid-1990s, the technique was extended with limited success to zinc-blende and diamond-structure epitaxial semiconductors, such as GaAs/Si and SiGe/Si [5.6-5.7]. More recently, the high defect densities in GaN and AlN have spurred renewed interest, and as a result, several approaches now exist for measuring threading-dislocation density in III-nitrides by XRD [5.8 – 5.15]. The physical basis for all of these works is measurement of the Bragg peakwidth, which varies with dislocation density.

Here we develop and test a reciprocal-space model of the Bragg peakwidth that describes its dependence on the coherence length, the tilt variance, and the twist variance of a dislocated epitaxial layer. We then analyze the functional form of the model in an effort to unify previous formulations. We conclude with experiments comparing threading-dislocation densities determined by XRD to those determined by transmission electron microscopy (TEM).

We examine GaN, AlGaN, and AlN heterostructures grown on the basal plane of sapphire or SiC by metal-organic chemical-vapor deposition. XRD was performed using a four-circle goniometer coupled to a four-fold (220) Ge monochromator delivering Cu $K\alpha_1$ x-rays. Scattered x-rays were detected by a Xe-filled proportional counter collimated with a three-fold (220) Ge analyzer. TEM was performed using a Philips CM20 microscope. Cross-sectional and plan-view specimens were prepared using Ga focused-ion-beam milling or

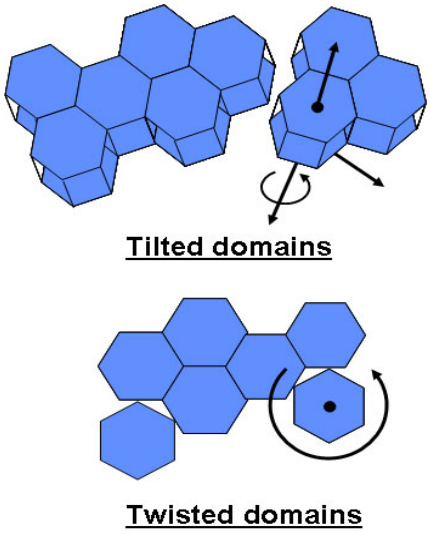

Fig. 5.1. Shows the GaN granularity and how the grains are tilted and twisted with respect to the normal c-axis.

appear in reciprocal space as broadened reciprocal-lattice points (dark-grey ellipses) of inverse size $2\pi/L \times 2\pi/h$. Inhomogeneous rotation of the lattice causes further broadening (light-grey ellipses) in directions transverse to the reciprocal-lattice vector $\mathbf{K}_{hkl}$. Each local rotation consists of three components, which we define as rotations about the Cartesian components $\mathbf{K}_{hkl}$ with the origin of reciprocal space conceptually attached to the surface of the crystal as in Fig. 5.2(a). Rotations about K_z are the familiar *twist*, while rotations about either K_x or K_y are the familiar *tilt*. Finally, inhomogeneous dilatation of the interplanar spacing further broadens these spots, but now along the direction of $\mathbf{K}_{hkl}$ (not shown).

We measure the transverse mechanical thinning followed by Ar-ion milling. The thickness of cross-sectional specimens was determined to ±20% using convergent-beam electron diffraction [5.16].

XRD measurements of threading-dislocation density rest on the fact that the strain fields produced by dislocations cause both a partial loss of long-range coherence of the crystal lattice, and inhomogeneous rotation and dilatation of the crystal planes. The domain tilts and twists are shown in Fig. 5.1 and are defined with respect to the c-axis. In Fig. 5.2(a) the distortions of the real-space lattice lead to corresponding broadening of the reciprocal-lattice points [5.14]. For example, reduced coherence produces finite-sized real-space domains of lateral width L and thickness h that

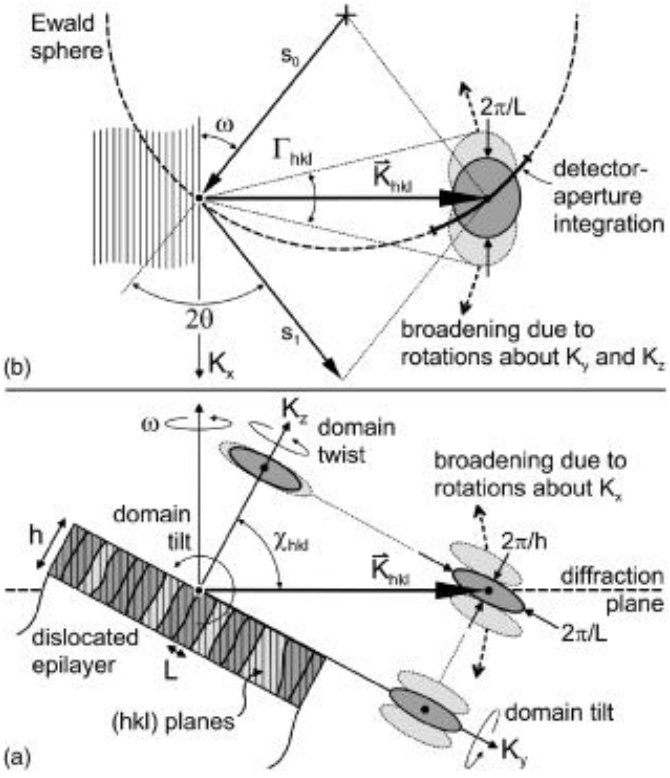

Fig. 5.2. Schematic diagram showing the real-space microstructure of a dislocated sample, the resulting reciprocal-space structure, and the skew diffraction geometry used to probe the reciprocal space: (a) Cross-sectional view of the sample and the diffraction plane, and (b) plan view of same.

width Γ_{hkl} of a broadened reciprocal-lattice point using the skew sample geometry also shown in Fig. 5.2. This geometry provides a pivotal advantage when applied to an asymmetric reflection: It is sensitive to broadening due to *both* tilt and twist [5.9, 5.10, 5.12-5.16]. To set up this geometry, the reflection of interest is brought into the diffraction condition by rotating the crystal's surface normal out the diffraction plane by an angle χ as in Fig. 5.2(a), with the rocking angle ω set to the Bragg angle θ as in Fig. 5.2(b). Here χ is the angle between $\mathbf{K}_{hkl}$ and the (001)-surface normal. The resulting geometry enables small-angle rocking curves (ω-scans) that move the tip of $\mathbf{K}_{hkl}$ parallel to rotations about both K_z and K_y, which is why both tilt and twist are probed. In contrast, traditional coplanar scans of asymmetric reflections, where the surface normal remains in the diffraction plane, see only tilt. [5.14].

Figure 5.2(b) shows a plan view of the quasi-symmetric diffractometer configuration and Ewald-sphere construction created by the skew geometry. Here, $\mathbf{s}_0$ and $\mathbf{s}_1$ represent the wave vectors of incident and scattered x-rays, respectively. Whenever a wide detector aperture is used, $\mathbf{s}_1$ fans out into a range of 2θ (not shown) producing a range of detected momentum transfers about $\mathbf{K}_{hkl}$ that integrate the diffraction pattern along the surface of the Ewald sphere (heavy black arc). This integration partially folds any broadening along $\mathbf{K}_{hkl}$ into the transverse scan. Like some others [5.11, 5.15], we use a highly collimated detector to eliminate this unwanted effect.

Under these conditions, we can describe the transverse width of a rocking curve by convolving contributions due to the tilt variance, the twist variance, and the coherence length:

$$\Gamma_{nkl}^{n} = (\Gamma_y \cos\chi)^n + (\Gamma_z \sin\chi)^n + (2\pi / L)^n / K_{hkl}^{n}, \qquad (1)$$

where Γ_{hkl} is the measured full-width at half-maximum (FWHM) of the Bragg peak, Γ_i is the FWHM of the rotational distribution about K_i (i=x, y, or z), and K_{hkl}=$|\mathbf{K}_{hkl}|$. The individual terms are folded using Gaussian (n=2), pseudo-Voigt (1<n<2), or Lorentzian (n=1) distributions [5.9]. Variation of the lateral coherence length L with (hkl) is approximated using two values, L_s and L_a, for symmetric and asymmetric reflections, respectively. We omit broadening due to several small instrumental effects [5.5, 5.6] that are negligible when peakwidths are large as in III-nitride films. If we multiply Eq. (1) by K_{hkl}^{n}, the root of each term becomes an easily recognized arc length in reciprocal space. For example, by inspecting Fig. 5.2, we see that the first right-hand term results from broadening along the arc traced by tilt rotations about K_y using a moment arm of length K_{hkl} cos χ. Similarly, the second term results from the arc traced by twist rotations about K_z using a moment arm of length K_{hkl} sin χ. The last term results from the arc defined by the reciprocal coherence length.

5.2 Applying the XRD method.

Figure 5.3(a) shows a fit of Eq. (1) to typical rocking-curve data for GaN on sapphire. Note that the full model (solid lines) very accurately describes the Bragg peakwidths seen for 16 different reflections from GaN. Figure 5.3(b) shows that an excellent fit also results for more defective AlN on sapphire. The fitted results shown in Fig. 5.3 assume that n=2; moreover, additional fits find that the overall goodness of fit steadily degrades for any n<2. We

conclude from this global behavior of the fitted peakwidths that Gaussian convolution is optimal. If we remove coherence-length contributions by setting L_s=L_a=∞, the model shifts downward (dotted lines). For low-index reflections, the shift is readily observed but small, while for high-index reflections, the shift almost vanishes. These results confirm previous suggestions [5.9] that errors produced by omitting the coherence length are moderate (always <20% in Fig. 5.3).

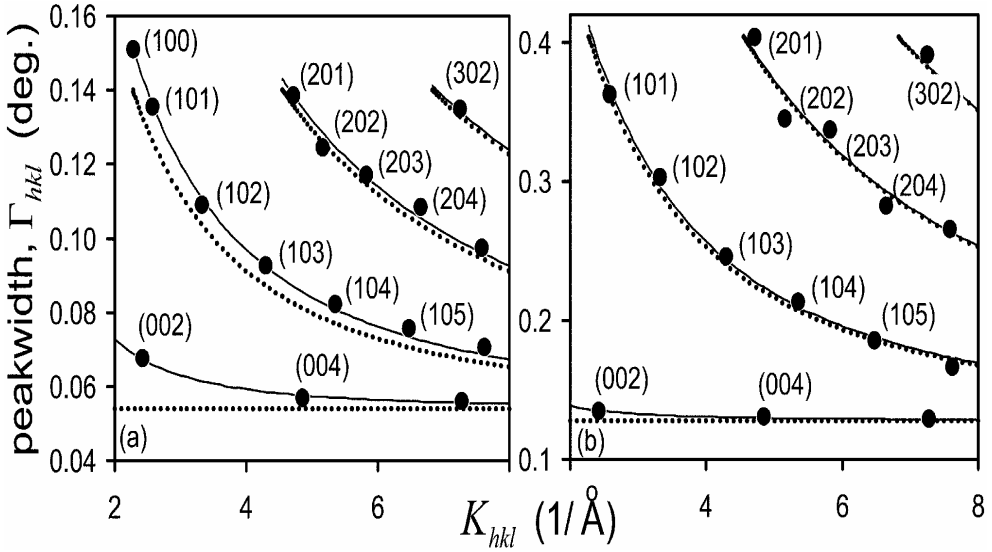

Fig. 5.3. Least-squares fits of Eq. (1) to measured Bragg peakwidths for: (a) 2 μm thick GaN with a threading-dislocation density of 1.7×10^{9} cm^{-2}, and (b) 1.5 μm thick AlN with a threading-dislocation density of 1.2×10^{10} cm^{-2}.

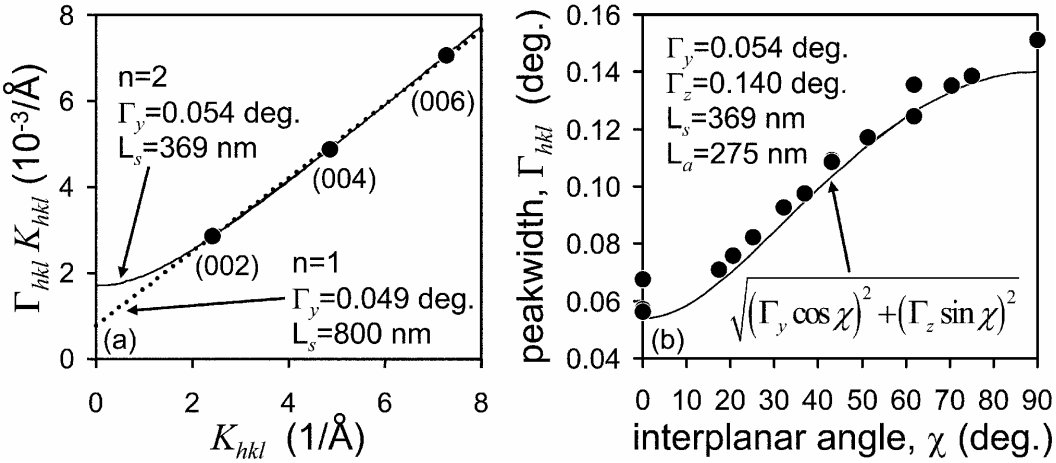

Fig. 5.4. Recasting of the data and fits in Fig. 5.3 (a) to show the relationship to (a) the traditional W–H model, and (b) χ-plots of lattice-rotation models (developed in Refs.[5.9, 5.13]).

Interestingly, Eq. (1) encapsulates many aspects of previous models. For instance, if we again multiply Eq. (1) by K_{hkl}^{n} and then take the nth root, we recover the Williamson–Hall (W–H) model [5.2] in generalized form. Figure 5.4(a) replots Fig. 5.3(a) data in this format for symmetric reflections where χ = 0. Recalling that K_{hkl}=(4π/λ)(sin θ), we find the expected linear behavior for W–H plots of Γ_{hkl}(sin θ)/λ versus (sin θ)/λ. Comparing the n=1

and n=2 plots in Fig. 5.4(a), we also find that Lorentzian folding extrapolates to much larger coherence lengths than does Gaussian folding. This result reaffirms early discussions by W–H pointing out the importance of the convolution type [5.2] Since Gaussian folding provides a superior global fit (*cf.* Fig. 5.3), it is likely that the Lorentzian folding normally used in W–H models materially overstates the coherence length in the III-nitrides.

Figure 5.4(b) shows that we can also replot Fig. 5.3(a) data versus χ in order to recover χ -plots like those presented for the rotational models developed by Srikant [5.9] and Sun [5.13]. However, there are three notable differences between our model and these previous models. First, we use a small-angle approximation for the lattice rotations—the advantage is highly simplified expressions that are the limit of the general rotational formulae adopted elsewhere [5.9, 5.13]. Second, as already discussed, we include coherence-length effects. In Fig. 5.4 (b), these effects appear as vertical displacements of the experimental data to positions that lie above a plot of the purely rotational part of our model (solid line). Third, we use no adjustable "interdependence" or "weight" parameters as in Refs. [5.9, 5.13]. As seen in Fig. 5.3, these *ad hoc* fitting parameters are not needed to accurately model the transverse peakwidths that are measured here in skew geometry.

Routine measurements of the parameters Γ_y, Γ_z, L_s, and L_a can be made by fitting Eq. (1) to as few as two symmetric and two asymmetric reflections. In our comparisons to TEM below, we use five reflections: (002), (004), (006), (101), and (202). We also note that if faster experiments are needed, the coherence-length term can be dropped from Eq. (1) thereby allowing Γ_y and Γ_z to be approximated using only one symmetric and one asymmetric reflection.

Threading-dislocation densities then follow from various classic formulae [5.3 – 5.5]. If threading dislocations are randomly distributed, then (i) $\rho = \Gamma^2/(4.36b^2)$ and (ii) $\rho = 1/L^2$ apply. If grain boundaries are formed, then (iii) $\rho = \Gamma/(2.09bL)$ applies instead. Here b is the magnitude of the relevant Burgers vector component b_s or b_e [5.10]. For Γ==Γ_y and L=L_s, these formulae give the density of dislocations ρ_s that possess a screw component b_s=c (**b**=**c** or **b**=**a**+**c**). For Γ=Γ_z and L=L_a, these formulae instead give the density of dislocations ρ_e that possess an edge component b_e=a (**b**=**a** or **b**=**a**+**c**).

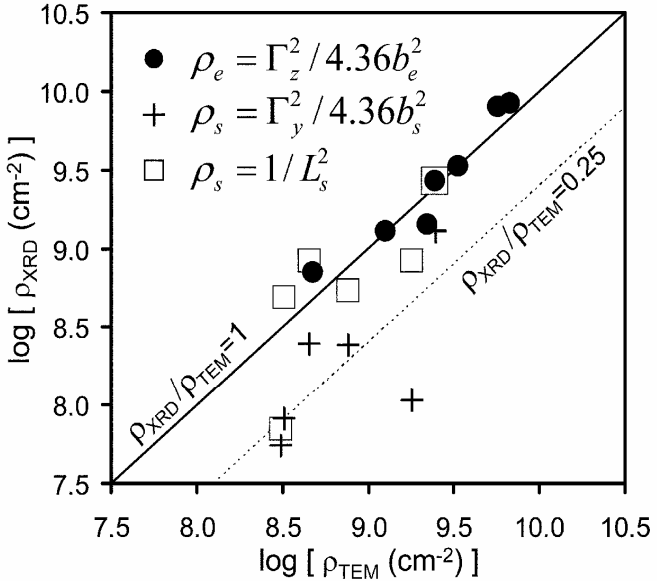

Fig. 5.5. Comparison of threading-dislocation densities measured by XRD to those measured by TEM. The examined samples consist of GaN on AlN/SiC (3 each), GaN on sapphire (2 each), $Al_{0.35}Ga_{0.65}N$ on GaN/sapphire (1 each), and $Al_{0.48}Ga_{0.52}N$ on AlN/sapphire (1 each). All samples are 0.8 to 3 μm thick.

5.3 Comparison of the dislocation density measured using XRD to TEM.

Figure 5.5 compares threading-dislocation densities found by XRD to measurements made on the same samples by TEM. As seen in the figure, agreement is very good across a broad range of sample types when we compare results for ρ_e obtained using formula (i) just above. Even if we attribute all errors to XRD and none to TEM, the root-mean-square error for the XRD results for ρ_e is <33%. Formulas (ii) and (iii) above also yield data for ρ_e (not shown) that follow the line defined by the ratio $\rho_{XRD}/\rho_{TEM}=1$, but the rms error substantially increases because of the lower accuracy of L_a (versus Γ_z), which results from the small contribution that L_a makes to the fitted peakwidths. The agreement between formulae implies that the dislocations contributing to ρ_e are randomly spaced.

If we compare results for ρ_s, different behavior is seen. Figure 5.5 shows that the data shift downward onto the curve $\rho_{XRD}/\rho_{TEM}=0.25$ when formula (i) is used, indicating poorer average agreement between XRD and TEM for ρ_s. If formula (ii) is used instead, five of six samples shift upward to the line $\rho_{XRD}/\rho_{TEM}=1.0$; results for formula (iii) fall in between (not shown). These shifts suggest smaller than expected tilt variances relative to the symmetric coherence lengths, possibly caused by adjacent dislocations having opposite-parity Burgers vectors such that tilt rotations partially cancel.

Previous comparisons of XRD and TEM often find somewhat poorer agreement than seen here. For example, Kirchner [5.12] indirectly compare four GaN samples and find that $\rho_{XRD}/\rho_{TEM}=2$ to 5 for ρ_e, while $\rho_{XRD}/\rho_{TEM}=0.1$ to 0.2 for ρ_s. Chierchia [5.14] compare three GaN samples using formula (i) and similarly find that $\rho/\rho_{TEM}=2$ to 7 for ρ_e; however, using formula (iii), they find that $\rho_{XRD}/\rho_{TEM}=0.7$ to 1.6. They cite this much-improved agreement as evidence that threading dislocations in their samples are nonrandomly spaced. Paduano [5.14] compare three AlN samples, and find that

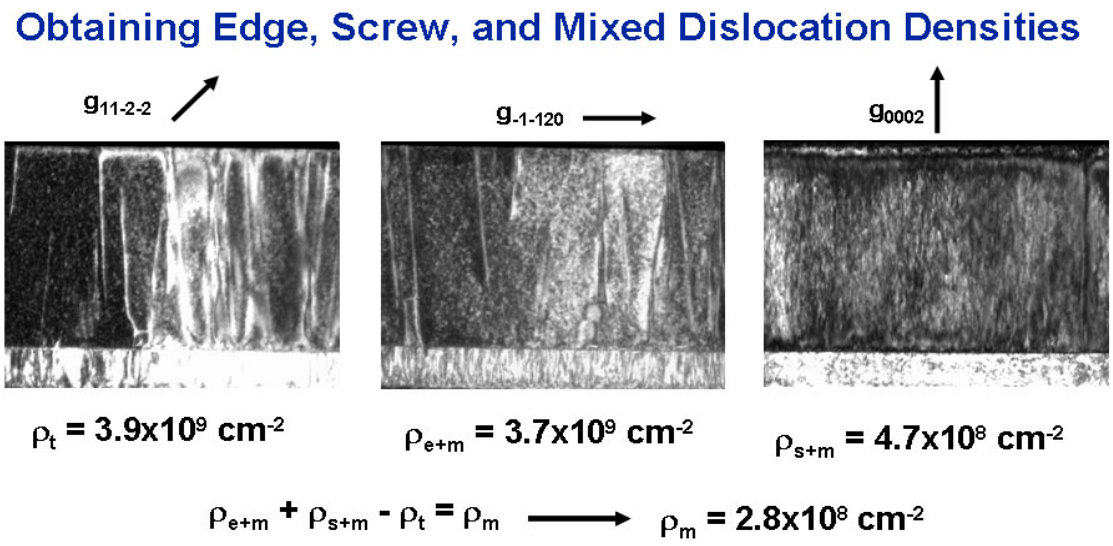

Fig. 5.6. TEM cross section images using three different imaging conditions were used to calculate the number of pure edge, pure screw and mixed edge and screw type dislocations. Note that the ρ_E = $3.4x10^9$ cm^{-2} > ρ_M = $2.8x10^8$ cm^{-2} > ρ_S = $1.9x10^8$ cm^{-2}.

ρ_{XRD}/ρ_{TEM}=1.6 to 4 for ρ_e. In brief, XRD has tended to overestimate ρ_e and underestimate ρ_s; differences with TEM greater than a factor of 2 have been common. To fully explain these variations in accuracy, yet more detailed comparisons of XRD and TEM, along with refined analysis of the mechanics that couple measured lattice distortions to the density and configuration of heterolayer dislocations, are needed.

5.4 Routine use of XRD to determine the dislocation density.

A TEM cross section measurement of the dislocation density is shown in Fig. 5.6 for one GaN film sample. For this cross section image the different g-vectors allow imaging of the total dislocations and the separate edge and screw component dislocations. Taking into account the finite thickness of the sample the dislocation densities can be estimated from these images. Note that as described in Fig. 5.6 the edge dislocation density is larger than the mixed or screw dislocation densities. Since the edge dislocation density is the largest demonstrate the importance of using the asymmetric XRD reflections in conjunction with symmetric XRD reflections to achieve an accurate measure of the dislocation density.

Correlations between the HEMT mobility and the total dislocation density are shown in Fig. 5.7. For this Figure the sheet carrier density varies with lower sheet carrier density producing higher mobility 2DEGs. Note that the HEMTs with the highest electron mobility have a total dislocation density near $1x10^9$ cm^{-2}. This plot demonstrates that there exists a dependence of the electron mobility on the dislocation density. Also note that as the sheet carrier density increases the electron mobility decreases even at constant dislocation density. XRD has proven to be an essential tool for the routine evaluation of the HEMT structure. The consistency of the material quality was demonstrated in Fig. 2.17.

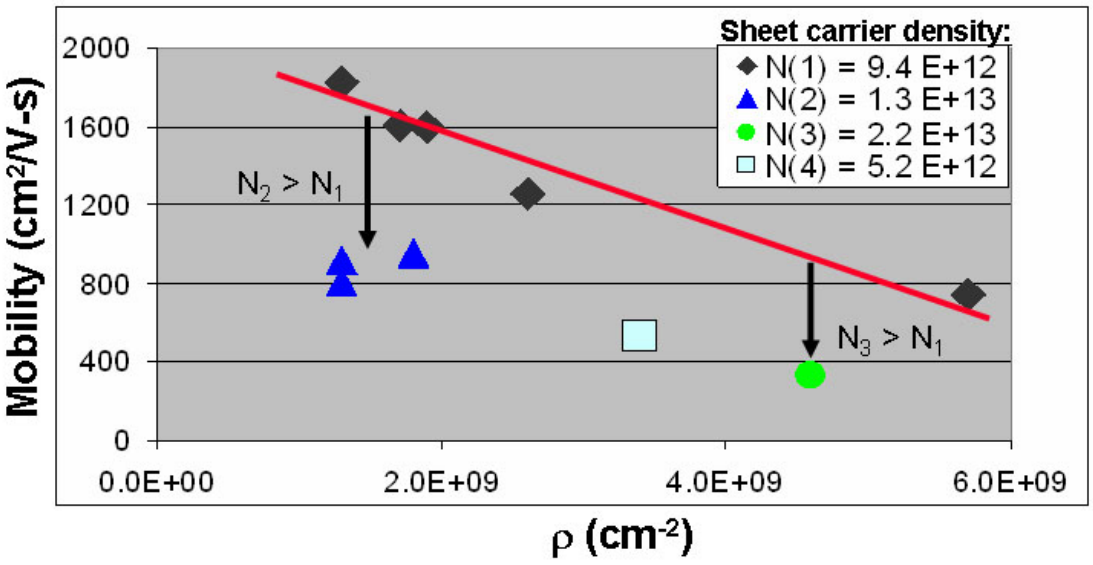

Fig. 5.7. The HEMT 2DEG mobility is plotted vs. the total dislocation density as measured by XRD.

5.5 References.

[5.1]. Debdeep Jena, Arthur C. Gossard, and Umesh K. Mishra, Appl. Phys. Lett. **76**, 1707 (2000).

[5.2] G. K. Williamson and W. H. Hall, Acta Metall. **1**, 22 (1953).

[5.3]. P. Gay, P. B. Hirsch, and A. Kelly, Acta Metall. **1**, 315 (1953).

[5.4]. C. G. Dunn and E. F. Koch, Acta Metall. **5**, 548 (1957).

[5.5]. M. J. Hordon and B. L. Averbach, Acta Metall. **9**, 237 (1961).

[5.6]. J. E. Ayers, J. Cryst. Growth **135**, 71 (1994).

[5.7]. E. Koppensteiner, A. Schuh, G. Bauer, V. Holý, G. P. Watson, and E. A. Fitzgerald, J. Phys. D **28**, A114 (1995).

[5.8]. B. Heying, X. H. Wu, S. Keller, Y. Li, D. Kapolnek, B. P. Keller, S. P. DenBaars, and J. S. Speck, Appl. Phys. Lett. **68**, 643 (1996).

[5.9]. V. Srikant, J. S. Speck, and D. R. Clarke, J. Appl. Phys. **82**, 4286 (1997).

[5.10]. T. Metzger, R. Höpler, E. Born, O. Ambacher, M. Stutzmann, R. Stömmer, M. Schuster, H. Göbel, S. Christiansen, M. Albrecht, and H. P. Strunk, Philos. Mag. A **77**, 1013 (1998).

[5.11]. H. Heinke, V. Kirchner, S. Einfeldt, and D. Hommel, Phys. Status Solidi A **176**, 391 (1999).

[5.12]. V. Kirchner, M. Fehrer, S. Figge, H. Heinke, S. Einfeldt, D. Hommel, H. Selke, and P. L. Ryder, Phys. Status Solidi B **216**, 659 (1999).

[5.13]. Y. J. Sun, O. Brandt, T. Y. Liu, A. Trampert, K. H. Ploog, J. Bläsing, and A. Krost, Appl. Phys. Lett. **81**, 4928 (2002).

[5.14]. R. Chierchia, T. Böttcher, H. Heinke, S. Einfeldt, S. Figge, and D. Hommel, J. Appl. Phys. **93**, 8918 (2003).

[5.15]. Q. S. Paduano, A. J. Drehman, D. W. Weyburne, J. Kozlowski, J. Serafinczuk, J. Jasinski, and Z. Liliental-Weber, Phys. Status Solidi C **0**, 2014 (2003).

[5.16]. B. Williams and C. Carter, *Transmission Electron Microscopy* (Plenum, New York, 1996), pp. 321–323.

6. In-situ measurements of AlGaN critical thickness

6.1 Importance of AlGaN/GaN stress state for HEMTs.

One of the main issues for AlGaN/GaN HEMT development is the maximum strain/thickness that the AlGaN can apply to the GaN layer to induce the 2DEG. Using *in-situ* wafer-curvature measurements of thin-film stress, we determine the critical thickness for strain relaxation in $Al_xGa_{1-x}N$/GaN heterostructures for Al compositions from 18% to 100 %. These ranges of Al cover typical Al compositions over the entire range. Using the critical-thickness models for brittle fracture and dislocation glide along with AFM measurements of the surface morphology we determined that the strain relaxation occurs by surface fracture for all compositions. Misfit-dislocations follow initial fracture, with slip-system selection occurring under the influence of composition-dependent changes in surface morphology. The formation of these misfit-dislocations is detrimental to the formation of the 2DEG and should introduce current leakage pathways.

6.2 In-situ determination of the AlGaN critical thickness on GaN.

When $Al_xGa_{1-x}N$ alloys are grown on (0001) GaN they have a tensile in-plane misfit strains which ranges from 0 to 2.38%. The elastic energy generated by these misfit strains drives fracture, plastic deformation, and surface instabilities during epitaxial growth of these materials. Consequently, the critical thicknesses where fracture and dislocation glide become possible in AlGaN/GaN place important limits on the design of device heterostructures. While previous work has measured the critical thickness of $Al_xGa_{1-x}N$/GaN alloys for $0.09 \le x \le 0.42$ [6.1-6.2] and for $x=1$ [6.3-6.6] little data exists in between these ranges.

Here we used the multi-beam optical stress sensor to measure the critical thickness for strain-relaxation in $Al_xGa_{1-x}N$/GaN epitaxial thin films for $0.18 \le x \le 1$. Experiments were carried out using $Al_xGa_{1-x}N$/GaN heterostructures that were grown on (0001) sapphire substrates by metal-organic chemical vapor deposition (MOCVD) in the RDR reactor shown in Fig. 2.1. Growths were performed at 1050 °C and 70-140 torr using trimethylgallium (16 - 95 μmoles / min.), trimethylaluminum (28 - 110 μmoles / min.), and ammonia (0.25-9 slpm) in hydrogen carrier gas. All AlGaN layers were Si doped (~$2x10^{18}$ cm^{-3}). Growth rates (1.7 μm/hr for GaN, and 0.11-0.65 μm/hr for $Al_xGa_{1-x}N$) were measured in-situ using optical reflectance [6.7]. Thin-film stresses were measured in real time using in-situ laser-deflectometry measurements of wafer curvature [6.8]. Following growth, the surface morphology of

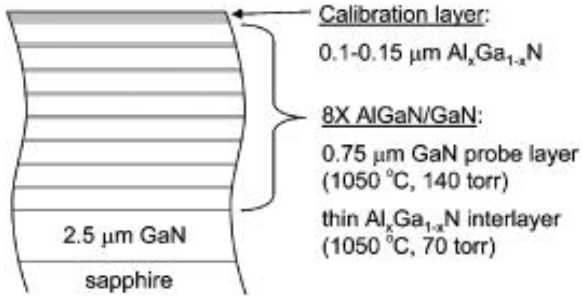

Fig. 6.1. Schematic diagram of the multilayer samples used to probe the critical thickness for strain relaxation in AlGaN.

selected samples was examined using tapping-mode AFM. The composition and strain of $Al_xGa_{1-x}N$ calibration samples was measured by x-ray diffraction using radial scans of reciprocal space about (0004), $(10\bar{1}1)$, and $(20\bar{2}5)$.

As shown in Fig. 6.1, special multilayer heterostructures were used to detect the critical thickness for the onset of strain relief. A series of bilayers comprised of $Al_xGa_{1-x}N$/GaN are grown on top of a thick GaN pseudo-substrate on sapphire. In the first bilayer, the AlGaN is chosen to be thinner than the expected critical thickness. In each subsequent bilayer, the thickness of the AlGaN is incremented by a constant multiplicative factor (1.2X to 2X, depending on the sample design). The GaN overlayer that completes each bilayer probes the strain state of the underlying AlGaN. An increase in the stress of the GaN probe layer signals the introduction of misfit dislocations at the previous AlGaN/GaN interface and indicates the onset of strain relaxation in the AlGaN. (Direct measurements of the AlGaN stress were precluded by the extremely thin layers of interest, signal-to-noise limitations of the laser deflectometer, and oscillatory artifacts produced by film-thickness gradients [6.9]) Each experiment concludes with growth of a thicker capping layer of AlGaN, which is used to calibrate the growth rate and composition.

Fig. 6.2 shows the real-time wafer-curvature data that results for a typical critical-

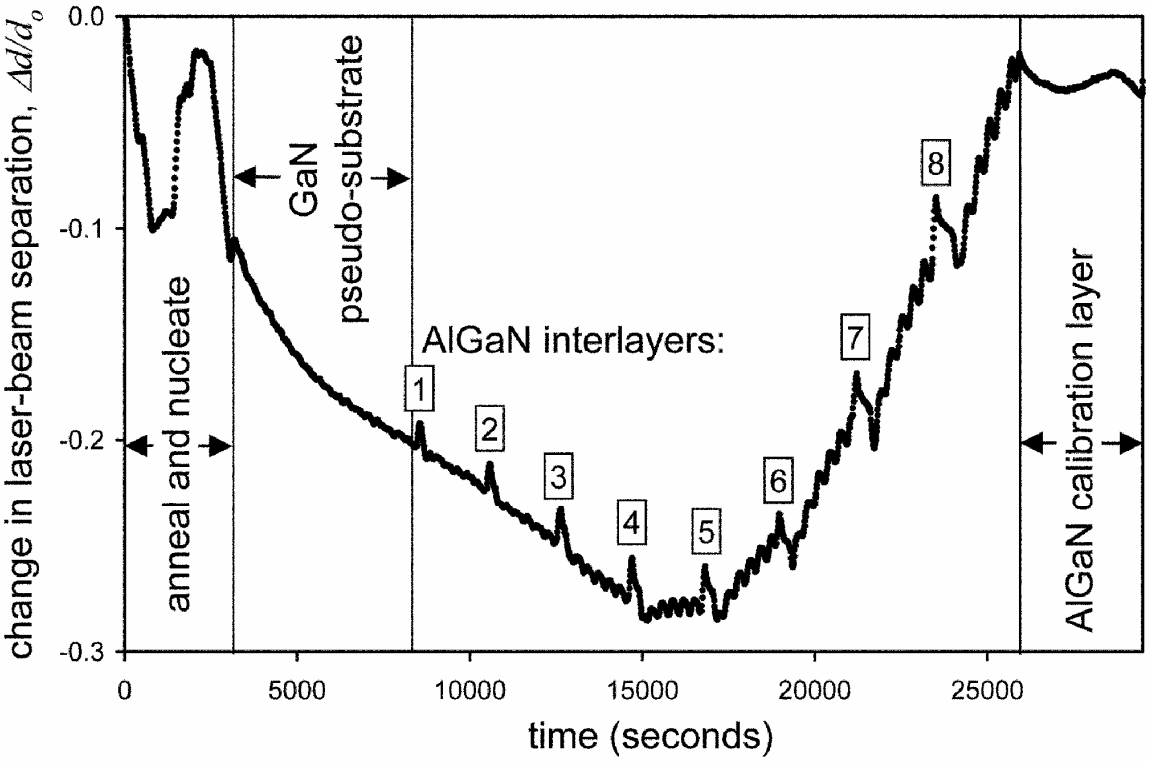

Fig. 6.2. Stress evolution during the growth of eight $Al_{0.89}Ga_{0.11}N$/GaN bilayers on GaN. The AlGaN layers sequentially increase in thickness as follows: 1.8, 2.3, 3.0, 3.8, 5.0, 6.5, 8.4, and 11 nm. Each GaN probe layer is 0.75-μm thick. Periodic oscillations in the data arise from optical diffraction effects produced by minor film-thickness gradients and are not due to film stress [6.9]. Spikes in the data as each AlGaN layer is grown result from reactor pressure changes and are also not due to film stress.

thickness experiment. Note that the normalized change in laser-beam separation ($\Delta d/d_0$) measured in the experiment is proportional to both the wafer curvature ($1/R$) and the stress-thickness product of the thin film (Δh_f) [6.8]. Since growth time is proportional to film thickness (h_f), the slope in Fig. 6.2 measures the film stress. In the figure, the slope (and stress) is nearly constant from the end of the GaN pseudo-substrate growth to the end of the third GaN probe layer. Since stress does not change in this interval, the first three AlGaN interlayers are unrelaxed and pseudomorphic with the surrounding GaN. The fourth probe layer clearly changes slope, which unambiguously signals the onset of strain relief. In our example, the critical thickness (h_c) is bracketed by the thicknesses of the third and fourth AlGaN interlayers (3.0 nm $< h_c \leq$ 3.8 nm). Subsequent AlGaN layers dislocate further with increasing thickness, which drives each GaN probe layer further into compression, as signified by their rising slopes.

Fig. 6.3 compares our measured critical thicknesses for a series of $Al_xGa_{1-x}N$/GaN heterostructures to previous reports in the literature. Reasonable agreement with previous work is found. For $x<0.42$ our data fall just below previous MOCVD results obtained by Hearne *et al.* [6.1] and Parbrook *et al*. [6.2], but we do not observe metastability against fracture as seen by Hearne *et al.* at low Al compositions. At the other extreme, $x=1.0$, our

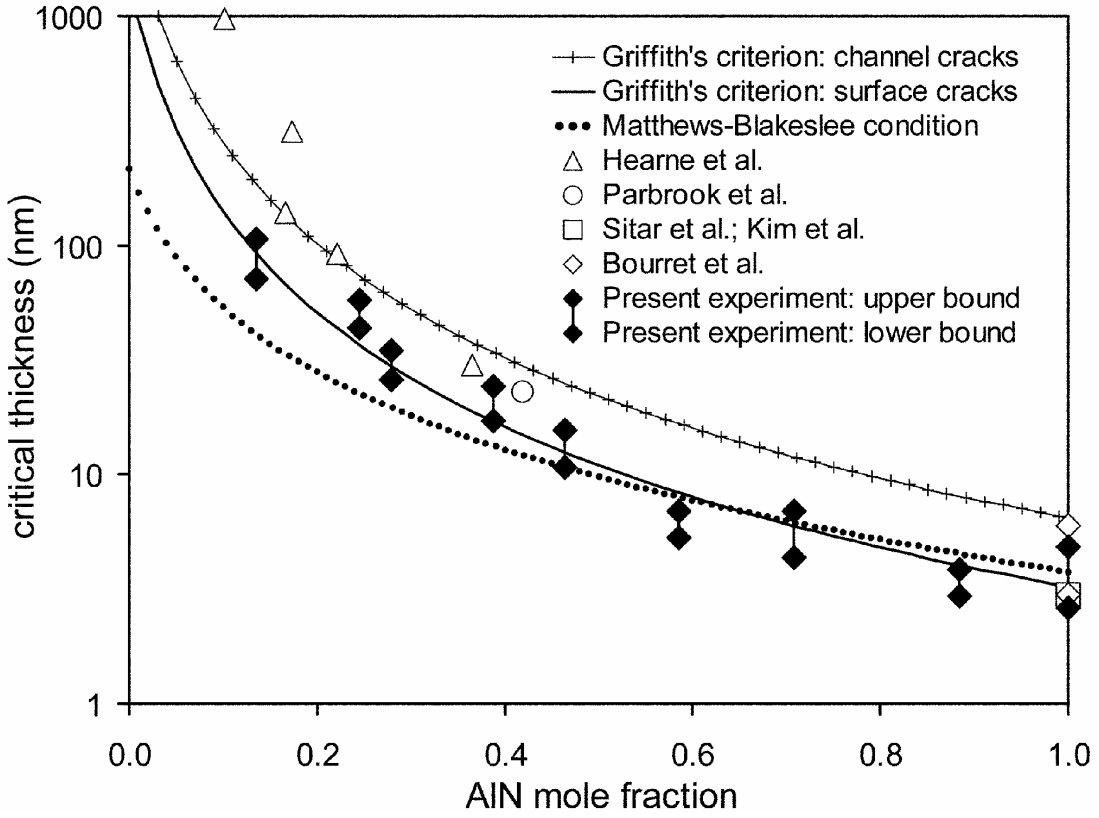

Fig. 6.3. Comparison of measured critical thicknesses for strain relaxation in $Al_xGa_{1-x}N$/GaN to previous measurements and theoretical calculations. For $x<1$, our measurements are for samples grown using an ammonia flow of 1 slpm. For $x=1$, we average results for six samples grown with ammonia flows of 0.25-9 slpm (no trend with ammonia flow was observed).

data bracket results reported by both Sitar *et al.* [6.3] and Kim *et al.* [6.10], which were obtained using transmission-electron microscopy (TEM) and XRD studies of materials grown by molecular-beam epitaxy (MBE).

All of these x=1 results exceed the very small critical thicknesses (0-0.75 nm) reported in *in-situ* reflection high-energy electron diffraction (RHEED) studies [6.4-6.6]. This discrepancy can be resolved by considering the mechanisms thought to be at work. Earlier RHEED works attribute initial relaxation to rapid dislocation glide [6.4, 6.5], but this can be ruled out because glide is prohibited by energy-balance considerations. Later work invokes elastic relaxation produced by surface-morphology [6.5], which is credible because no critical-thickness limit exists for roughening. Since the GaN probe-layers used in the present work are not sensitive to coherent surface morphology, this also explains why we do not see a similar critical thickness. Interestingly, these RHEED studies also report a secondary critical-thickness stage at 3-6 nm [6.5, 6.6]. This secondary stage agrees with observations obtained by wafer curvature, TEM, and XRD.

In an effort to better understand the sequence of mechanisms that operate at the onset of strain relaxation, we calculated theoretical critical-thickness values for three different relaxation processes: (1) brittle fracture by propagation of surface cracks, (2) brittle fracture by propagation of channeling cracks, and (3) plastic deformation by dislocation glide. Critical thicknesses for brittle fracture were calculated using Griffith's criterion as formulated by Hutchinson and Suo [6.11]. Critical thicknesses for dislocation glide were calculated using the Matthews-Blakeslee (M-B) condition as formulated by Freund [6.12]. Additional details specific to AlGaN alloys appear in Ref. [6.13]. Note that our calculations include a nominal correction for the intrinsic growth stress of GaN [6.8] (~0.25 GPa), which renders the critical thicknesses finite at x=0.

Fig. 6.3 compares these calculations to the experimental data. Turning first to fracture, we note the distinction between surface cracks and channeling cracks [6.11]. Surface cracks are self-limiting in lateral extent, and thus, may have isolated crack termini. In contrast, channeling cracks are unstable and propagate laterally until they terminate at another crack or the edge of the film. Fig. 6.3 shows that our measured critical thicknesses closely match theory for surface fracture and always fall well below theory for channel fracture. Therefore, we infer that surface-fracture initiates relaxation (producing a composition dependence in accord with surface-fracture theory). Importantly, misfit dislocations must shortly follow; otherwise, there would be no change in stress in the overlying GaN probe layer signaling relaxation. An interesting and ironic consequence of these results is that AlN interlayers used for fracture control in AlGaN/GaN may themselves function through initial fracture.

Fig. 6.3 also shows the Matthews-Blakeslee condition for dislocation glide on the $\frac{1}{3}\langle\bar{1}\,\bar{1}23\rangle/\{11\bar{2}2\}$ slip system [6.13], which we examine as an alternative to initiation by fracture. This slip system gives a lower bound for the inclined second-order slip systems that are viable in biaxially strained planar alloys grown on (0001) GaN [6.13, 6.14]. For x<0.5, the M-B condition lies below the measured critical thickness, and dislocation glide appears to be initially metastable, in agreement with previous work [6.1, 6.13]. For x>0.6, the M-B condition moves above Griffith's criterion for surface-fracture making surface fracture the favored process. Yet for x>0.5, the proximity of our data to both theories leaves open the

possibility that dislocation glide may operate first. This ambiguity notwithstanding, we have no clear evidence suggesting that dislocation metastability suddenly ceases for x>0.5; moreover, we do have additional direct evidence for surface fracture in this same regime.

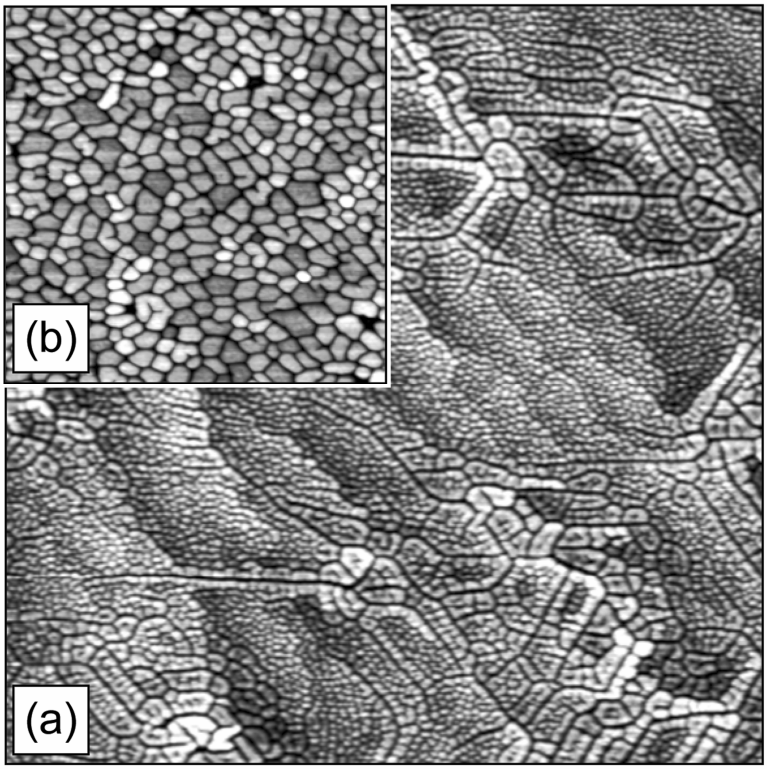

Fig. 6.4. (a) 2x2 μm^2 AFM image an 9-nm-thick $Al_{0.51}Ga_{0.49}N$ layer grown using an ammonia flow of 1 slpm. The height scale of the image ranges from 0 nm (black) to 2.5 nm (white). (b) 1x1 μm^2 AFM image of a 10-nm-thick AlN layer grown using an ammonia flow of 6 slpm. The height scale of the image ranges from 0 nm (black) to 4.0 nm (white).

Take for example Fig. 6.4(a), which shows the rich surface morphology found by AFM for a 9-nm-thick layer of $Al_{0.51}Ga_{0.49}N$ on GaN. Several unterminated surface-fractures lines are clearly visible, which verifies that surface fracture does indeed operate at a very early stage. These fractures are of further interest because they are decorated by a complex system of facetted mounds. The mounded regions tend to be thicker than adjacent terraces suggesting an enhanced incorporation rate at locally strain-relaxed regions that bound the fracture lines. Away from fractured areas, surface-steps are clearly visible, and a fine-scale dot-like surface morphology covers all of the terraces.

In contrast, Fig. 6.4(b) shows an AFM image for a 10-nm-thick layer of AlN on GaN. This sample exhibits a more homogeneous surface morphology that is free of steps, fine-scale roughness, and obvious fracture lines; nonetheless, there is tentative evidence for surface fracture here as well. Note that the surface consists of a dense array of facetted or rounded mounds bounded by a network of grooves that are at least ~2-4 nm deep. Many of these mounds are strikingly similar in size and shape to the mounds that decorate the surface fractures in Fig. 6.4(a), which suggests that surface-fracture may also have lead to the facetted features observed here. Presumably, overt fracture lines have vanished due to the growth and surface transport that follows initial fracture at a critical thickness near 3 nm.

The different surface morphologies seen in Fig. 6.4(a) versus Fig. 6.4(b) will influence which slip systems operate during plastic deformation the AlGaN. As discussed elsewhere [6.1, 6.13, 6.14], nonplanar morphologies on the (0001) surface produce inhomogeneous strain fields that enable basal-plane glide of misfit dislocations on the normally inactive $\frac{1}{3}\langle\bar{1}\bar{1}20\rangle/\{0001\}$ primary slip system. If the bounding grooves are sufficiently deep, the dense

array of small mounds seen in Fig. 6.4(b) would be particulary compatible with this mechanism. In contrast, extended planar surfaces adjacent to crack channels or mounded regions (e.g., the terraces seen in Fig. 6.4(a)) will have little inhomogeneous strain. In this case, only the inclined secondary slip systems can act to propagate interfacial dislocations to regions remote from morphological features such crack channels or mounds.

In conclusion, we have measured the critical thickness for strain relaxation of $Al_xGa_{1-x}N$/GaN alloys for the composition range $0.18 \le x \le 1$. The measurements closely follow Griffith's criterion for surface fracture indicating that surface fracture acts first to initiate relaxation. AFM shows unterminated surface-fracture channels in support of this interpretation. AFM also shows a marked change in surface morphology as composition and ammonia flow are varied. The different surface morphologies that result will have varying inhomogeneous strains, which will influence the slip systems available for dislocation glide. Taken as a whole, our results show that strain-relaxation in $Al_xGa_{1-x}N$ alloys proceeds through a complex interplay involving fracture, surface morphology, and dislocation glide.

6.3 References.

[6.1]. S. J. Hearne, J. Han, S. R. Lee, J. A. Floro, D. M. Follstaedt, E. Chason, and I. S. T. Tsong, Appl. Phys. Lett. **76**, 1534 (2000).

[6.2]. P. J. Parbrook, M. A. Whitehead, R. J. Lynch, and R. T. Murray, Mat. Res. Soc. Symp. Proc. Vol. **743**, 505 (2003).

[6.3]. Z. Sitar, M. J. Paisley, B. Yan, J. Ruan, W. J. Choyke, and R. F. Davis, J. Vac. Sci. Technol. B **8**, 316 (1990).

[6.4]. N. Grandjean and J. Massies, Appl. Phys. Lett. **71**, 1816 (1997).

[6.5]. G. Feuillet, B. Daudin, F. Widmann, J. L. Rouviere, and M. Arlery, J. Cryst. Growth **189/190**, 142 (1998).

[6.6]. A. Bourret, C. Adelmann, B. Daudin, J. L. Rouviere, G. Feuillet, and G. Mula, Phys. Rev. B **63**, 245307 (2001).

[6.7]. W. G. Breiland and K. P. Killeen, J. Appl. Phys. **78**, 6726 (1995).

[6.8]. S. Hearne, E. Chason, J. Han, J. A. Floro, J. Figiel, J. Hunter, H. Amano, and I. S. T. Tsong, Appl. Phys. Lett. **74**, 356 (1999).

[6.9]. W. G. Breiland, S. R. Lee, and D. D. Koleske, J. Appl. Phys. **95**, 3453 (2004).

[6.10]. C. Kim, I. K. Robinson, J. Myoung, K. Shim, M.-C. Yoo, and K. Kim, Appl. Phys. Lett. **69**, 2358 (1996).

[6.11]. J. W. Hutchinson and Z. Suo, *Advances in Applied Mechanics*, Vol. 29 (Academic Press, San Diego 1992), pp. 63-191.

[6.12]. L. B. Freund, J. Mech. Phys. Solids **38**, 657 (1990).

[6.13]. J. A. Floro, D. M. Follstaedt, P. Provencio, S. J. Hearne, and S. R. Lee, submitted to J. Appl. Phys.

[6.14]. S. Srinivasan, L. Geng, R. Liu, F. A. Ponce, Y. Narukawa, and S. Tanaka, Appl. Phys. Lett. **83**, 5187 (2003).

7. Heat modeling and measurement of HEMT layers

7.1 Modeling of heat flow during HEMT operation.

Various methods for thermal management of GaN-based HEMT layers on SiC were surveyed. Heat recovery, refrigeration cooling, and various heat transport and sinking methods were considered, including the use of heat pipes and forced liquid cooling in microchannels. In addition, a thermal solution method was developed for a GaN based HEMT. For the case study a HEMT with 5 gate groups each composed of 10 gates 100μm in width with a 10μm gate pitch were modeled. For the operation of the HEMT, a 5 W/mm dissipated power density and an effective heat source width = 1 μm were assumed. Thermal modeling for the center gate is shown in Fig. 7.1 Because SiC is a comparatively good thermal conductor the bottom side boundary condition is assumed to be equivalent to an infinite extension of the SiC substrate thickness. The maximum temperature rise at the top surface is 106.4°C and the temperature difference in the view of a) is 83.3°C. The maximum temperature rise at the bottom surface is 45.6°C with a temperature range of 23.7°C in (b).

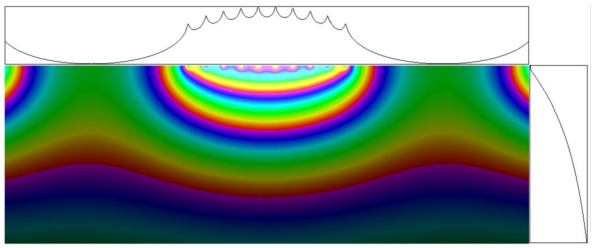

Fig. 7.1. Source line centered temperature crossections including top-center profile. The solution is shown for the center gate structure.

7.2 HEMT self-heating measured using UV micro-Raman scattering

We report micro-Raman studies of self-heating in an AlGaN/GaN heterostructure field-effect transistor using below (visible 488.0 nm) and near (UV 363.8 nm) GaN band-gap excitation. The shallow penetration depth of the UV light allows us to measure temperature rise (ΔT) in the two-dimensional electron gas (2DEG) region of the device between drain and source. Visible light gives the average ΔT in the GaN layer, and that of the SiC substrate, at the same lateral position. Combined, we depth profile the self-heating. Measured ΔT in the 2DEG is consistently over twice the average GaN-layer value. Electrical and thermal transport properties are simulated. We identify a hotspot, located at the gate edge in the 2DEG, as the prevailing factor in the self-heating.

Wide band-gap semiconductor GaN has recently been used to develop heterostructure field effect transistors (HFETs) for high power and microwave applications [7.1 – 7.4]. The large piezoelectric and spontaneous polarization fields occurring in the AlGaN/GaN heterostructures generate a quasi-two-dimensional electron gas (2DEG) at the hetero-interface without doping, and the 2DEG forms the conductive channel between the HFET drain and source (D–S). With the 2DEG confined within ≈10 nm and narrow HFET gate widths, channel current densities can be very high in these devices, leading to significant local Joule heating. This self-heating degrades HFET performance or results in irreversible damage. Thermal management is crucial to the viability of these devices, motivating accurate measurements of self-heating.

Figure 7.2 shows the *I–V* characteristics of the device studied here; the inset to Fig. 7.2 depicts the device structure [7.5]. The $Al_{0.19}Ga_{0.81}N$/GaN structure is grown on a 6H–SiC substrate. The device is composed of Ohmic source and drain contacts separated by 5 μm and a 2-μm-Schottky gate at the D–S center. The 1.5-μm-wide "windows" on each side of the gate are used for our micro-Raman measurements. The device gate width is 150 μm. We separate the *I–V* dependence into below and above saturation regions, and demark them with vertical lines at the $V_{D–S}$ values for each V_g. These two regions meet where a segment of the 2DEG has become depleted (with low carrier density and decreased mobility due to enhanced scattering) and drift velocity saturates [7.6]. Above this voltage (II) we see the current diminish with increasing $V_{D–S}$. This decrease correlates with the development of a localized "hotspot" at the gate edge, where the self-heating effect is strongest.

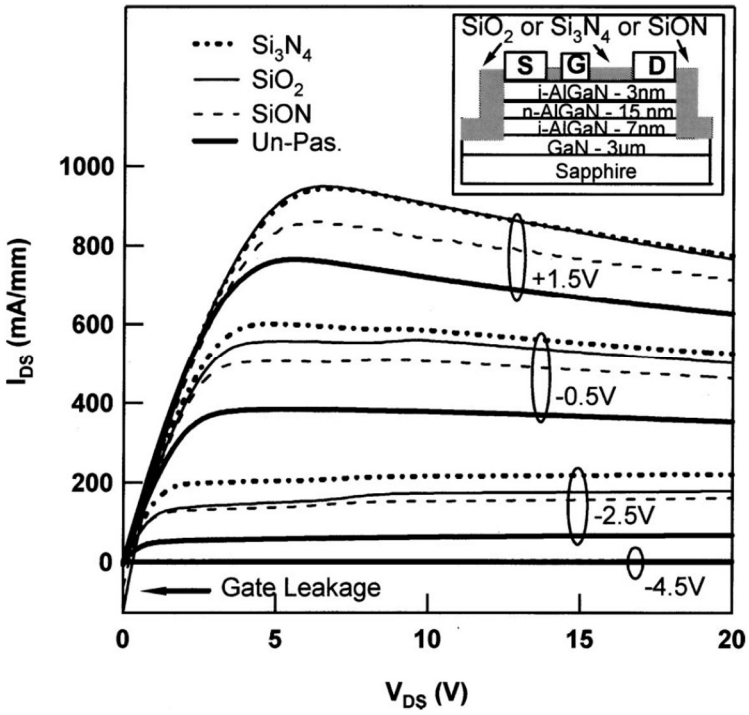

Fig. 7.2. *I–V* dependence for the AlGaN/GaN HFET at different V_g. Inset: device layout (not to scale).

Self-heating effects in these devices can be studied using micro-Raman spectroscopy via shift in the phonon energy (E_2^2 for GaN) [7.7]. To date, these have been performed solely using conventional visible excitation. Previous studies have exploited visible micro-Raman to laterally map self-heating in AlGaN/GaN HFETs [7.8 – 7.10]. Because GaN is transparent to visible light, one obtains an average measure of temperature limited by the layer thickness (or depth of focus), and the focus spot size. In contrast, micro-Raman measurements using near-band-gap ultraviolet (UV) excitation sample a shallow, near-surface region. For excitation wavelength 363.8 nm, the optical penetration depth is d_{opt} < 100 nm in GaN [7.11], close to the relevant length scale of the HFET active region and 2DEG. These measurements allow us to study the temperature rise (ΔT) of the HFET 2DEG region. We directly compare our results with micro-Raman measurements of the average ΔT in the GaN layer using sub-band-gap excitation (488.0 nm) under identical conditions. The visible measurements allow us to simultaneously obtain ΔT in the substrate via the SiC phonon shifts. Combined, the UV and visible studies provide us with a temperature depth profile of the structure under varying drive conditions, for which we find no previous report. We support our results with electrical and thermal simulations of the device.

Figure 7.2 shows measured temperature rise ΔT from room temperature versus input power for the same conditions as in Fig. 7.2. The measurements are performed ~0.3 μm from the gate edge on the drain ($V \geq 0$) side; the focal spot is ~0.6 μm in diameter. In each panel we show the GaN ΔT measurements using UV excitation, GaN with visible light, and SiC substrate temperature (visible). Values observed using UV light are consistently two to three times higher than those obtained with visible light due to the fact that the UV probe emphasizes the Al-GaN/GaN interfacial region where the local Joule heating takes place. As expected, the lowest ΔT values in Fig. 7.3 are for the SiC substrate since it has good thermal conductivity and is attached to a heat sink. We note in each panel a relatively rapid rise in temperature followed by a somewhat slower rise with input power. Our overall thermal resistance from the visible Raman measurements is 10.4±1.8 °C/(W/mm), in good agreement with previously reported results from similar devices [7.10].

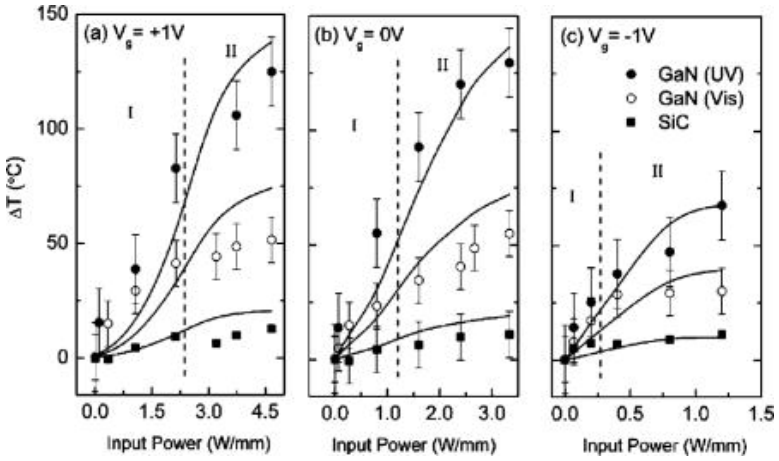

Fig. 7.3. Temperature rise (from ambient) vs. input power at gate voltages (a) +1 V, (b) 0 V, and (c) –1 V. 2DEG from UV Raman data (●). Average GaN (○) and SiC (■) from visible Raman data. Solid curves are simulation results.

We have conducted combined electrical and thermal simulations of the device structure. Two approaches are used to simulate the electrical behavior. A 2D finite difference analysis [7.12] is used to self-consistently solve the Poisson equation coupled with the continuity and Schrödinger equations [7.13]. The FE analysis includes 1 μm thick GaN followed by the $Al_{0.19}Ga_{0.81}N$ layer (Fig. 7.2, inset). Ohmic contacts are used for source and drain regions, and the gate is a Schottky contact (1.2-eV barrier height). The meshing emphasizes the 2DEG and immediately surrounding layers. The Joule heating density (W/cm^3) is obtained from the simulated electric field and electron density, and using the field-dependent drift velocity [7.14]. Alternatively, a quasi-2D model was developed predicting HFET dc characteristics and power generation across the gate. The model incorporates Schrödinger–Poisson results for 2DEG density versus gate bias [7.15] and low-field 2DEG transport results obtained over a limited range of temperatures and carrier densities for our specific device [7.5]. This model extends into the saturation region with inclusion of a field-velocity expression from Monte Carlo calculations [7.16], a "channel length" correction required to accommodate velocity saturation and maintain continuity [7.17], and local heating. Above saturation, both methods show the Joule power to be primarily localized to a power peak ~0.1 μm wide (FWHM, averaged through 2DEG depth) and located in the 2DEG region at the edge of the gate on drain side. A sample FE simulation is shown in Fig. 7.4(a) for V_{D-S}=4 V (V_g=0,P=1.6 W/mm). The characteristics of the simulated power peak and the hot-electron processes leading to its formation are consistent with what has been previously described for

a GaN HFET [7.18]. The simulated D–S power density profiles are used directly in our thermal simulation.

For the finite element (FE) thermal analysis [7.19] we use the same layer architecture inset to Fig. 7.2. Thermal conductivities (κ) of GaN are known to depend on dislocation density (ρ_D) [7.20], which varies along the epitaxial growth direction. We divide the GaN layer in our simulation into two layers. The first layer is the 150 nm initial growth region, with κ = 1.3 W/cm K; the remainder of the GaN has $\rho_D < 10^{10}$ cm^{-2} and κ = 1.5 W/cm K [7.20]. We take into account the temperature dependence of these values according to Ref. [7.21]. Since the thin AlGaN plays a minor role in dissipating heat, we employ the properties of GaN. We use κ = 4.9 W/cm K for SiC (Ref. [7.22]) and ignore its temperature dependence, since the observed ΔT rise is small. No thermal boundary resistance [7.23] is used at the GaN/SiC interface. Heat is generated in the simulation by a thin slab at the AlGaN/GaN boundary according to the lateral dependence of the electrical simulation. Fig. 7.4(b) shows the thermal simulation for the drive conditions of Fig. 7.4(a). The hotspot is clearly seen near the gate edge. Heat conduction has the expected effect of broadening the hotspot. The vertical line illustrates the micro-Raman probe center. Figure 7.4(c) shows the simulated ΔT versus depth along the probe line. We see that a significant temperature decrease occurs in the GaN due to the high thermal conductivity of the SiC. For comparison with the measurements, a volume average is calculated from the simulated ΔT across the diameter of the microprobe and along the depth of the device. For the UV excitation, the depth average is taken over d_{opt} [7.24], while for visible light we average over the full GaN thickness.

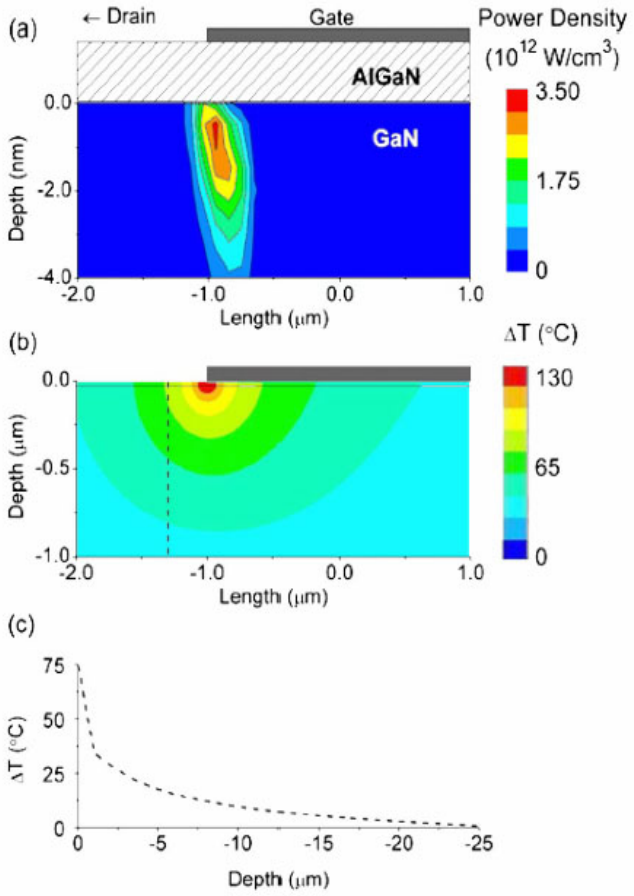

Fig. 7.4. (Color online) 2D FE simulation of the device at V_D=+4 V, source and gate grounded (P=1.6 W/mm): (a) Power density map. AlGaN thickness not to scale; (b) ΔT simulation; (c) ΔT along the vertical line segment (dashed line) shown under the arrow in (b). Note change in units on depth axis between (a) and (b).

Simulations are systematically carried out for several V_{D-S} values at each V_g studied. Results for ΔT are shown as solid curves in each panel of Fig. 7.3. We observe distinct heating regions marked by the vertical dashed lines in each panel corresponding to the regions

denoted on the *I–V* dependence in Fig. 7.2. The low-power range of region I corresponds to the Ohmic regime of the device and approaching the dotted line, the 2DEG becomes depleted at the drain. For $\kappa \sim 1/T$, a quadratic dependence is expected in ΔT versus power across the Ohmic region. The electrical simulations show a gradual increase in the electric field of the hotspot where region I approaches region II. The drift velocity in the hotspot is at its maximum near this boundary. Region II is above saturation, and beyond this point, additional power supplied to the device is dissipated primarily within the hotspot. With the hotspot broadening towards the source [7.17, 7.18] (i.e., under the gate metal) and the thermal gradient increasing, a diminishing fraction of the hotspot lies within the volume sampled optically. Combined, these factors lead to the slower temperature rise with input power in region II (see Fig. 7.3). Visible micro-Raman studies on the source side of the device reveal the bulk-GaN ΔT to consistently be ~50% that observed by the drain, thereby confirming the importance of the hotspot. The lateral temperature decrease is also in good agreement with the FE thermal analysis.

Models incorporating the 2DEG, velocity saturation, and thermal effects have provided excellent agreement with measured temperatures for the surface-2DEG, GaN layer, and SiC substrate regions for a range of AlGaN/GaN HFET drive conditions (V_{D-S} and V_g). We note that the maximum ΔT values measured using UV light are very high in comparison to our visible Raman measurements and those previously reported [7.8 – 7.10]. The simulations project that the *immediate* hotspot region exhibits a much higher temperature than values obtained in the UV studies. For example, under the highest drive power in Fig. 7.3(b), the simulated hotspot $\Delta T \approx 240$ °C (3.3 W/mm) while the UV and visible measurements give 130 and 55 °C, respectively, thus illustrating the importance of local heating. Our experimental results, backed by simulations, vitally supplement previous work which suggested rather small vertical temperature gradients [7.8] Since prior measurements relied solely on lateral mapping by visible Raman, combined with FE analysis, we conclude that depth profiling provides critical information for understanding self-heating in these high-power devices.

7.3 References

[7.1]. O. Ombacher, B. Foutz, J. Smart, J. R. Shearly, N. G. Weimann, K. Chu, M. Murphy, A. J. Sierakowski, W. J. Schaff, L. F. Eastman, R. Dimitrov, A. Mitchell, and M. Stutzmann, J. Appl. Phys. **87**, 334 (2000).

[7.2]. M. A. Khan, X. Hu, A. Tarakji, G. Simin, J. Yang, R. Gaska, and M. Shur, Appl. Phys. Lett. **77**, 1339 (2000).

[7.3]. M. Singh and J. Singh, J. Appl. Phys. **94**, 2498 (2003).

[7.4]. F. Stengel, S. N. Mohammad, and H. Morkoç, J. Appl. Phys. **80**, 3031 (1996).

[7.5]. S. R. Kurtz, A. A. Allerman, D. Koleske, A. G. Baca, and R. D. Briggs, J. Appl. Phys. **95**, 1888 (2003).

[7.6]. U. V. Bhapkar and M. S. Shur, J. Appl. Phys. **82**, 1649 (1997).

[7.7]. We have established our own phonon shift vs *T* calibration curves for the HFET GaN and SiC substrate.

[7.8]. M. Kuball, J. M. Hayes, M. J. Uren, T. Martin, J. C. H. Birbeck, R. S. Balmer, and B. T. Hughes, IEEE Electron Device Lett. **23**, 7 (2002).

[7.9]. Y. Ohno, M. Akita, S. Kishimoto, K. Maezawa, and T. Mizutani, Jpn. J. Appl. Phys., Part 2 **41**, L452 (2002).

[7.10]. M. Kuball, S. Rajasingam, A. Sarua, M. J. Uren, T. Martin, B. T. Hughes, K. P. Hilton, and R. S. Balmer, Appl. Phys. Lett. **82**, 124 (2003).

[7.11]. J. Wagner, H. Obloh, M. Kunzer, M. Maier, K. Köhler, and B. Johs, J. Appl. Phys. **89**, 2779 (2001).

[7.12]. APSYS, Crosslight Inc. (2003).

[7.13]. E. M. Azoff, IEEE Trans. Electron Devices **36**, 609 (1989).

[7.14]. K. Seeger, *Semiconductor Physics-An Introduction* (Springer, Berlin, 2004).

[7.15]. F. Sacconi, A. Di Carlo, P. Lugli, and H. Morkoç, IEEE Trans. Electron Devices **48**, 450 (2001).

[7.16]. M. Farahmand, C. Garetto, E. Bellotti, K. F. Brennan, M. Goano, E. Ghillino, G. Ghione, J. D. Albrecht, and P. P. Ruden, IEEE Trans. Electron Devices **48**, 535 (2001).

[7.17]. B.-J. Moon, Y. H. Byun, K. Lee, and M. Shur, IEEE Trans. Electron Devices **37**, 908 (1990).

[7.18]. N. Braga, R. Mickevicius, R. Gaska, X. Hu, M. Shur, M. A. Khan, G. Simin, and J. Yang, J. Appl. Phys. **95**, 6409 (2004).

[7.19]. ANSYS Inc., Release 8.0 (2003).

[7.20]. J. Zou, D. Kotchetkov, A. A. Balandin, D. I. Florescu, and F. H. Pollak, J. Appl. Phys. **92**, 2534 (2002).

[7.21]. E. K. Sichel and J. I. Pankove, J. Phys. Chem. Solids **38**, 330 (1977).

[7.22]. M.E. Levinshtein, S.L. Rumyantsev, and M. Shur, in *Properties of Advanced Semiconductor Materials* (Wiley, New York, 2001).

[7.23]. K. A. Filippov and A. A. Balandin, MRS Internet J. Nitride Semicond. Res. **8**, 1 (2003).

[7.24]. Weighting according to attenuation factor $e^{-(\alpha_{in}+\alpha_{out})z}$ does not produce a significant difference in the simulated ΔT values.

8. Electroreflectance studies of AlGaN/GaN HEMTs

8.1 Introduction

With the capability to vary electric field, contacted electroreflectance is a powerful tool for investigating AlGaN/GaN heterostructures and their field-induced properties. Large piezo-electric and spontaneous polarization fields occurring in AlGaN/GaN heterostructures can generate a two-dimensional electron gas (2DEG) without doping. High 2DEG carrier densities, electron saturation velocities, breakdown fields, and thermal conductivities found in these structures make them attractive as heterostructure field effect transistors (HFETs) for high voltage, high power microwave amplifiers [8.1 – 8.5]. We have implemented an electroreflectance technique which utilizes nitride HFET fabrication processes and augments conventional electrical characterization of these devices. In this article general characteristics and analysis of AlGaN/GaN electroreflectance are described. We find that contacted electroreflectance measurements reveal distinct spectral features associated with the AlGaN barrier, 2DEG, and adjacent GaN interface. Testing models of AlGaN/GaN bandstructure, these experiments provide a direct measurement of AlGaN polarization fields. We present a calculation of the GaN 2DEG dielectric function which simulates electroreflectance results over a wide range of electron density. Comparing previous results for heterostructures grown on sapphire with recent results for samples grown on SiC, the measured AlGaN electric field approached that predicted by a bandstructure model for the higher quality sample grown on SiC.

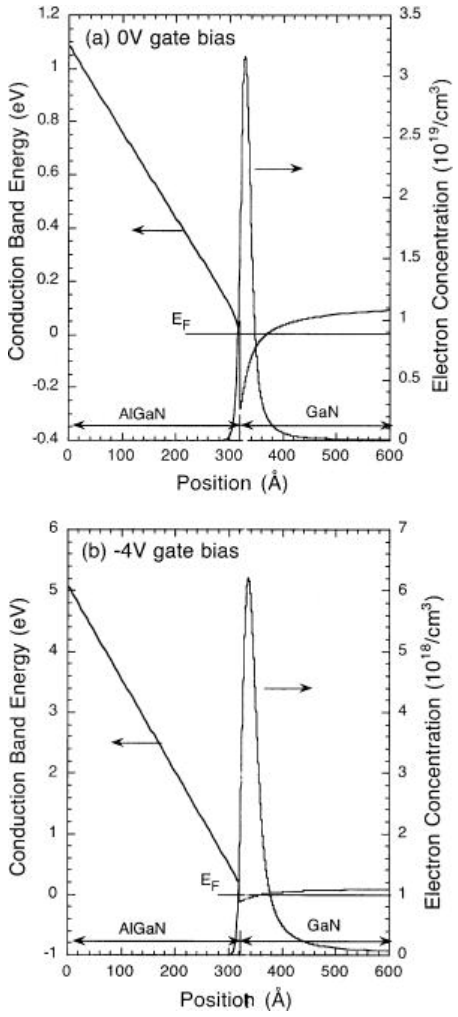

Fig. 8.1. Schrödinger–Poisson cal-culation of conduction band energy and electron density for an $Al_{0.19}Ga_{0.81}N$ (320 Å)/GaN hetero-structure with 0 V (a) and –4 V (b) gate bias, 300 K [note different *y*-axis scales for (a) and (b)].

8.2 Assignment of the electro-reflectance features to HEMT band-structure

In undoped AlGaN/GaN heterostructures, a large polarization electric field, the boundary conditions, and the conduction band offset combine to produce the 2DEG. For AlGaN/GaN grown on Ga-faced, GaN, the thin AlGaN layer is in biaxial tension, and the sum of piezoelectric and heterointerface, "spontaneous" polarization components results in 10^5–10^6 V/cm electric fields in the AlGaN layer. The Fermi energy at

the surface of the AlGaN is pinned, and the resulting Schottky barrier is described by a composition dependent, empirical rule. The origin of the surface pinning is not presently understood. With the large electric field and pinned surface potential of the AlGaN layer, electrons are transferred from the surface to form a 2DEG at the AlGaN/GaN interface. This "standard model" of AlGaN/GaN heterostructures is summarized by Ambacher *et al.* [7.5].

Unusually large 2DEG carrier densities ($>1\times10^{13}/cm^2$) are found in AlGaN/GaN heterostructures. From Schrödinger–Poisson solutions of the "standard model," we obtained the bandstructure and carrier density of the $Al_{0.19}Ga_{0.81}N$ (320 Å)/GaN heterostructure, studied extensively in this work. As illustrated in Figs. 8.1(a) and 8.1(b) for 0 V and –4 V (gated AlGaN surface potential relative to the 2DEG), respectively, 2DEG carrier density was depleted with increased electric field in the AlGaN barrier. (As a rough approximation $\Delta V \approx \Delta Q/C_{geo}$, where ΔV is a change in voltage across the AlGaN barrier, ΔQ is the change in 2DEG density, and C_{geo} is the geometric capacitance of the AlGaN layer.) Thereby, observed energy shifts in the electroreflectance with bias voltage allowed us to unambiguously assign electroreflectance features to elements of the AlGaN/GaN band structure.

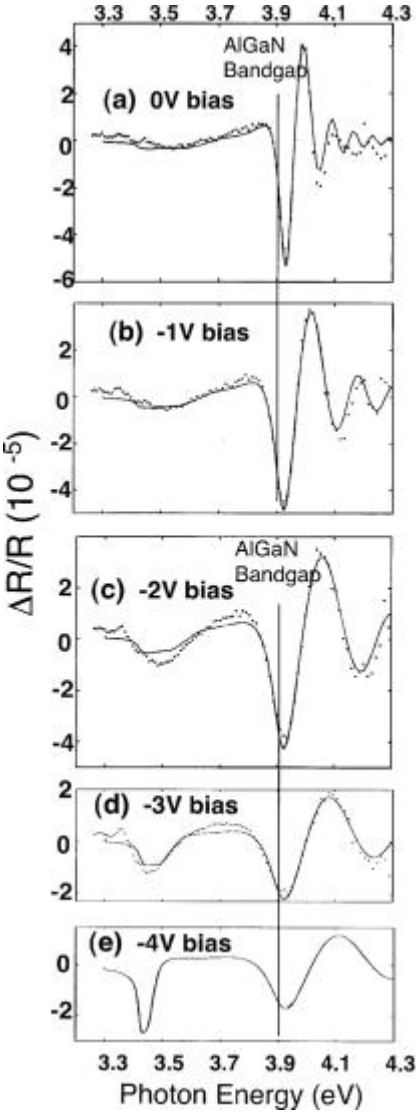

Fig. 8.2. Electroreflectance spectra (300 K) for the $Al_{0.19}Ga_{0.81}N$ (320 Å)/GaN heterostructure at 0 V (a), –1 V (b), –2 V (c), and –3 V (d) gate bias (same scale). Solid lines are the AlGaN FKO line shape fit plus the contribution from the 2DEG dielectric model. Based on the models, the –4 V spectrum (e) was simulated.

Electroreflectance spectra for the AlGaN/GaN heterostructure, grown on SiC, are shown in Fig. 8.2. As reported previously for thicker InGaN (Ref. [8.6]) and AlGaN (Ref. [8.7]) layers, Franz–Keldysh oscillations (FKOs) were clearly observed from the polarization-induced electric field in the AlGaN barrier. The period of the FKO increased as the barrier electric field increased with negative gate bias, enabling identification of those features associated with the AlGaN barrier [8.8]. In addition, a broad 2DEG feature appeared at energies just above the band gap of GaN [8.8-8.10]. As the 2DEG was depleted, the broad feature narrowed and converged with the GaN band-edge feature [8.8]. In general, such a broad first-derivative 2DEG feature has been observed in electroreflectance studies where contacts have been made between an HFET Schottky gate and the 2DEG channel [8.8, 8.10]. With this configuration, only the AlGaN barrier field, 2DEG carrier density, and the position of the GaN/2DEG interface were modulated, eliminating spurious spectral features which may be

associated with other parts of the multilayer sample in a contactless measurement. Through modulation of the GaN interface, bulk GaN features were observed at ≤ 3.42 eV in all spectra, and the bulk GaN feature grew in amplitude with depletion of the 2DEG.

Experimental AlGaN FKO spectra were least-squares fit to the Airy function formula for a single band-edge [8.11]. This analysis of the 0 V bias spectrum [see Fig. 8.2(a), solid line] produced AlGaN electric-field (0.26 MV/cm, assuming an electron-hole reduced mass of 0.2 m_e) and band gap (3.93 eV) values close to those obtained from analysis of the high order FKOs with the simple asymptotic expression [8.8]. The measured electric field approaches the value (0.33 MV/cm) predicted by a "standard model" of this AlGaN/GaN heterostructure, shown in Fig. 8.1(a) Electroreflectance studies of a comparable AlGaN/GaN heterostructure grown on sapphire revealed a large AlGaN electric field (0.50 MV/cm), and we speculated that the electric field anomaly may be due to material quality issues such as trapped space charge in the barrier or an Al composition gradient [8.8]. Fitting of the AlGaN FKOs revealed a broad, first-derivative line shape for the 2DEG in the energy range, ≈ 3.4–3.8 eV. The 2DEG electroreflectance was modeled using a golden-rule calculation of the dielectric function for the measured 2DEG density, 7.4×10^{12} e/cm^2 (see Fig. 8.2, solid line). Contrary to previous reports [8.9], extra structure attributed to 2DEG quantum-confinement was not resolved in our measurements or model. Detailed analysis of these electroreflectance spectra will be presented in a later section.

8.3 Calculation of the 2DEG electromodulated dielectric function

To simulate the 2DEG electroreflectance line shape, we have developed a simple model which utilizes Schrödinger–Poisson data for 2DEG energy levels and wave functions. A golden rule calculation is performed to obtain the imaginary part of the 2DEG dielectric function, $\varepsilon_1(\hbar\omega)$ [8.12]:

$$\varepsilon_1(\hbar\omega) = \sum_{i,\nu,k\|}\left(\frac{2\pi e}{m_c^*\omega}\right)^2 \cdot |\langle \nu \mid \Psi_i(x')\rangle|^2 \cdot |\hat{\varepsilon}\cdot p|^2 \{1 - F[E_i(k_\|) - E_F]\} \cdot \delta[E_i(k_\|) - E_\nu(k_\|) - \hbar\omega], \quad (1)$$

for valence band states, $|v\rangle$, the Fermi function, F, quantum-confined electron wave function, $|\Psi_i\rangle$. and a wave vector in the 2DEG plane, $k_\|$. Substitute,

$$E_i(k_\|) - E_\nu(k_\|) = E_{i\perp} + E_\| - E_{\nu\perp}, \quad (2a)$$

where

$$E_\| = \hbar^2 k_\|^2 / 2\mu \quad (2b)$$

and μ is the electron-hole reduced mass ($\mu \approx m_e^*$). Holes at the band edge of GaN are massive ($m_h^* \approx 1.8\ m_e$) [8.13], suggesting a "classical" approximation, and at energies below the valence band minimum, the wave function of the massive hole oscillates rapidly. The large hole mass and the behavior of the 1D density of states allow us to consider only hole energies near the valence band-edge. We approximate the hole wave function with a delta-function, $|v\rangle = |\ \delta(x-x^t)\ \rangle$, with $E_{v\perp} \approx E_{v\perp}(x)$, the energy of the valence band edge across the

2DEG region. With this localized hole approximation, a spatially varying dielectric function across the 2DEG is defined by substitution into Eq. (1):

$$\varepsilon_1(\hbar\omega, x) \approx \sum_i \left(\frac{2\pi e}{m_c^*\omega}\right)^2 \cdot |\Psi_i(x)|^2 \cdot |\hat{e}\cdot p|^2 \frac{2\pi\mu}{\hbar^2} \cdot \int_0^\infty [1 - F(E_{i\perp} + E_{\parallel} - E_F)] \cdot \delta[E_{i\perp} + E_{\parallel} - E_{v\perp}(x) - \hbar\omega] dE_{\parallel}. \quad (3)$$

Line broadening, Γ, is included in the calculation by substituting a Lorentzian for the energy delta function:

$$\varepsilon_1(\hbar\omega, x) \approx \sum_i \left(\frac{2\pi e}{m_c^*\omega}\right)^2 \cdot |\Psi_i(x)|^2 \cdot |\hat{e}\cdot p|^2 \frac{2\pi\mu}{\hbar^2} \cdot \int_0^\infty \frac{2}{\pi\Gamma} \cdot \frac{[1 - F(E_{i\perp} + E_{\parallel} - E_F)]}{1 + [E_{i\perp} + E_{\parallel} - E_{v\perp}(x) - \hbar\omega]^2 (2/\Gamma)^2} dE_{\parallel}. \quad (4)$$

Requiring only Schrödinger–Poisson results for the 2DEG, this expression [Eq. (4)] can be evaluated for an array of $\hbar\omega$ and x values. The electromodulated component is obtained by calculating the differences in Eq. (4) resulting from small changes in 2DEG density or gate voltage, and convergence is reached with a small number of contributing electron quantum confinement states ($1 \leq i \leq 5$). The 2DEG thickness is only a fraction of the optical wavelengths under investigation, and the imaginary part of the electromodulated dielectric response, $\Delta\varepsilon_1(\hbar\omega)$, is obtained by integrating across the thickness of the 2DEG, which is equivalent to summing over final hole states. A Kramers–Kronig transform of $\Delta\varepsilon_1(\hbar\omega)$produces the real part of the electromodulated dielectric function, $\Delta\varepsilon_1(\hbar\omega)$. Measured differential changes in reflectance are related to the modulated dielectric function by

$$\Delta R/R = a(\varepsilon^*) \cdot \Delta\varepsilon_R(\hbar\omega) + b(\varepsilon^*) \cdot \Delta\varepsilon_I(\hbar\omega), \quad (5)$$

where a and b are Seraphin coefficients, specific to sample multilayer optical properties [8.14].

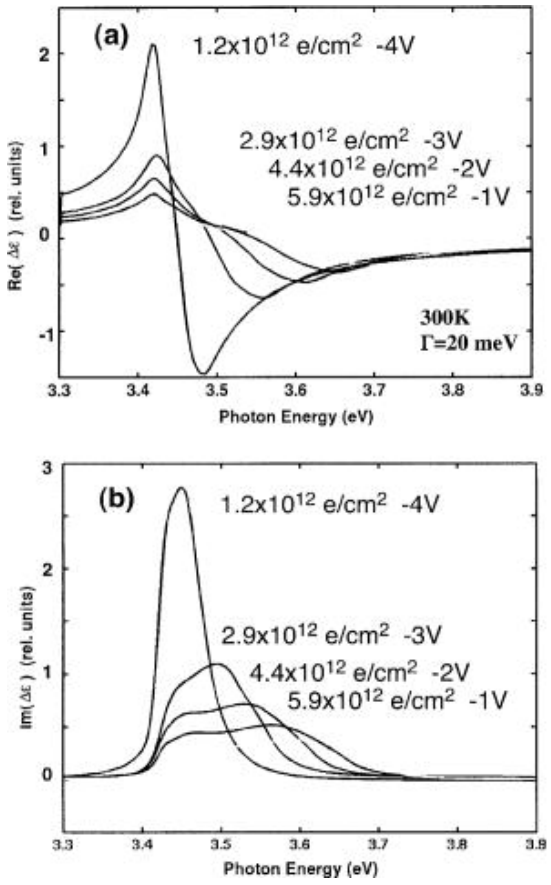

Fig. 8.3. Calculated real (a) and imaginary (b) electromodulated dielectric functions for 2DEGs over a range of electron densities or gate voltages.

This model produced a broad first derivative 2DEG electroreflectance line shape. Modulated dielectric functions calculated at 300 K and Γ = 20 meV for a range of electron densities are shown in Figs. 8.3(a) and 8.3(b). At 300 K, structure due to individual electron quantum confinement states was not well resolved, even with Γ = 0. The model predicted a well defined narrowing and shift of the 2DEG electroreflectance feature to lower energy with decreasing carrier density. With the peak-to-peak, small signal modulation voltage

fixed for all spectra, the amplitude of the 2DEG feature grew rapidly before merging with the bulk GaN feature upon depletion.

8.4. Experimental Details and electrical characterization of HEMT structures

AlGaN/GaN samples were grown by metalorganic chemical vapor deposition (MOCVD). Chemical sources were trimethylgallium, trimethylaluminum, and ammonia. The growth temperature was 1050 °C. An AlN nucleation layer was used to initiate GaN growth on sapphire or 4H–SiC substrates. For the heterostructure in this study, a 1-µm-thick GaN layer was unintentionally doped *n*-type, $4\times10^{17}/cm^3$, and the GaN layer was capped with a 320 Å thick, $Al_{0.19}Ga_{0.81}N$ barrier (background-doped mid-$10^{16}/cm^3$). Composition was determined from optical and x-ray measurements. Gated van der Pauw contacts (1–4 mm^2) were used for electroreflectance. Ohmic Ti/Al/Ni/Au source and drain contacts at corners of the sample penetrated to contact the 2DEG. Oxidized Ni(75 Å)/Au(75 Å) formed an optically transparent, Schottky barrier gate contact.

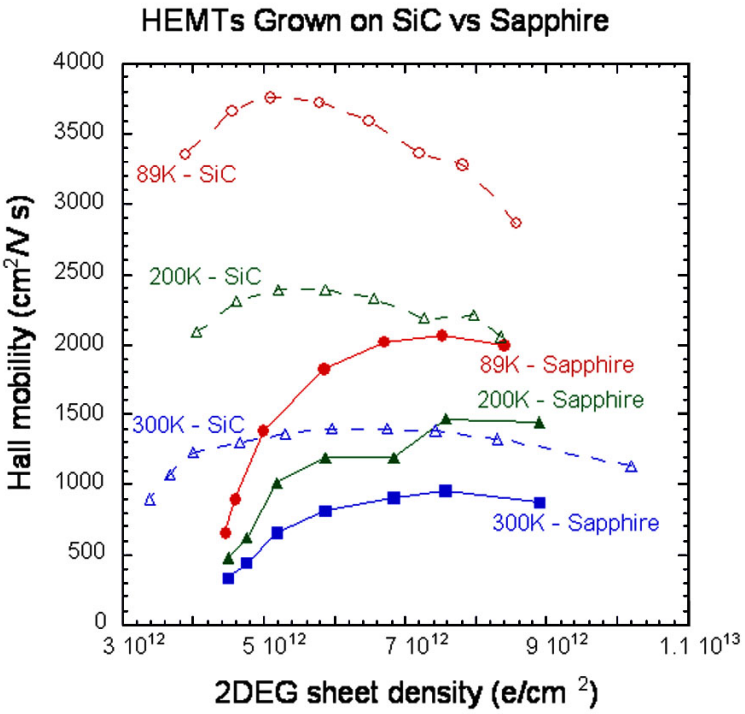

Fig.8.4. Hall mobility vs electron density from gated-Hall measurements. Results for the $Al_{0.19}Ga_{0.81}N$ (320 Å)/GaN heterostructure grown on SiC (solid lines) are compared with a similar structure grown on sapphire (dotted lines) for several temperatures.

For electroreflectance measurements, the sample was illuminated with a 150 W Xe lamp and a single grating monochrometer with 1 nm resolution. The electromodulated signal (150 Hz) was detected with a lock-in and a silicon, UV photodiode. All spectra were normalized to 0.2 V_{pp} modulation amplitude.

Compared with our previous studies of heterostructures grown of sapphire, AlGaN/GaN grown on 4H–SiC displayed an overall improvement in sample quality as demonstrated from Hall measurements. A gated-Hall configuration with a Schottky, "Red Cross-shaped" gate positioned between the ohmic van der Pauw contacts, was used to control 2DEG density for transport measurements. 2DEG gated-Hall mobility results for electroreflectance samples grown on sapphire and SiC are shown in Fig. 8.4. Gated Hall data were quoted only over a range where parasitic gate currents were negligible, and the carrier concentration versus gate voltage was consistent with capacitance–voltage (*C–V*) results. Typically the 2DEG on SiC displayed 300 K Hall mobilities >1000 cm^2/V s over a 2DEG density range 3.5×10^{12}–1.1×10^{13} e/cm^2, with the mobility weakly increasing with decreasing 2DEG density over much of that range. For the electroreflectance structure on SiC shown in Fig. 8.4, peak 300 K mobility was 1400 cm^2/V s@$6–7\times10^{12}$ e/cm^2, and peak low temperature (89 K) mobility was 3800 cm^2/V s@5×10^{12} e/cm^2. However, the 2DEG mobility (300 K) on sapphire peaked at 900 cm^2/V s and decreased with decreasing 2DEG density, dropping to 200 cm^2/V s@4×10^{12} e/cm^2. The dependence of Hall mobility on electron density indicated that 2DEG mobility was limited by high dislocation densities for our heterostructures grown on sapphire, and dislocation densities were reduced

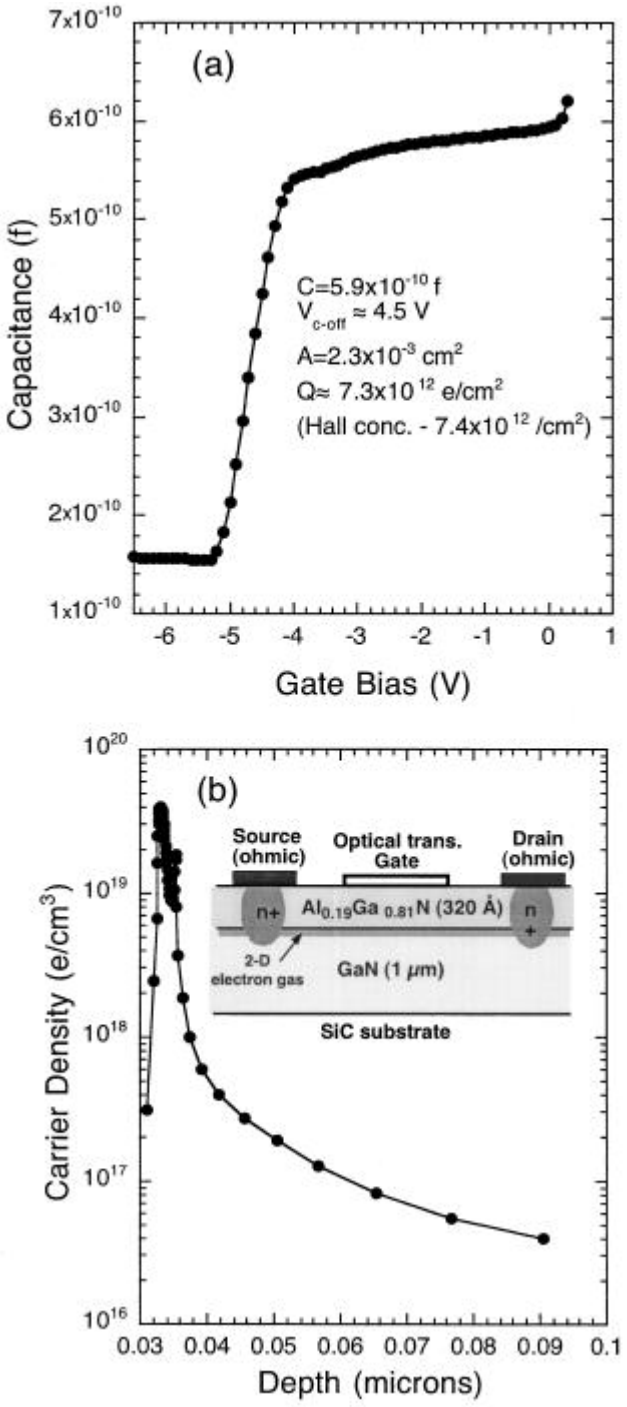

Fig. 8.5. Capacitance–voltage data (a) for the $Al_{0.19}Ga_{0.81}N$ (320 Å)/GaN heterostructure. *C–V* electron concentration profile (b) was determined from the differential capacitance. A drawing of the sample is shown as an inset in (b).

in heterostructures grown on SiC to levels where scattering from the AlGaN barrier limited 2DEG mobility [8.15, 8.16].

Complimenting our Hall results, Hg-probe *C–V* data for the electroreflectance sample grown on SiC are shown in Figs. 5(a) and 5(b). The measured 2DEG depletion or "knee" voltage (≈ 4.5 V) and the geometric capacitance (≈ 2.6×10^{-7} f/cm^2) [see Fig. 8.5(a)] produced a 2DEG sheet concentration of 7.3×10^{12} e/cm^2@0 V bias, in good agreement with the 0 V carrier concentration obtained with Hall measurements. The electron density in Fig. 8.5(b) was determined from the differential capacitance [$\propto dV/d(1/C^2)$]. The geometric capacitance provided an estimate of AlGaN layer thickness (320 Å), observed as the position of the onset of the 2DEG in Fig. 5(b).

8.5 Analysis of optical measure-ments

Results unique to electroreflectance were obtained by tracking the evolution of AlGaN barrier and 2DEG features with bias. The variation of electroreflectance with 0, –1, –2, and –3 V gate bias is shown in Figs, 8.2(a)–8.2(d), respectively, for the AlGaN/GaN heterostructure grown on SiC. Clearly the period of the AlGaN FKO increased with negative bias on the gate and increasing electric field in the AlGaN. Best line shape, Airy function fits of the FKO spectra in Figs. 8.2(a)–8.2(d) (solid lines) were obtained with an AlGaN band gap of 3.905±0.025 eV. From the band-gap energy, we estimated an $Al_xGa_{1x}N$ composition, x = 0.19±0.01, based on reflectance data for the ternary alloy [8.17, 8.18]. Although we infer some improvement in material quality for structures grown on SiC, the AlGaN FKO linewidth (≈ 30 meV) was comparable to that observed for samples grown on sapphire. Except for shifts to higher energy with increased band gap, the shape of these electroreflectance spectra were unchanged at 77 K, and we believe that linewidths remain limited by inhomogeneities and defects, not intrinsic phonon processes [8.19].

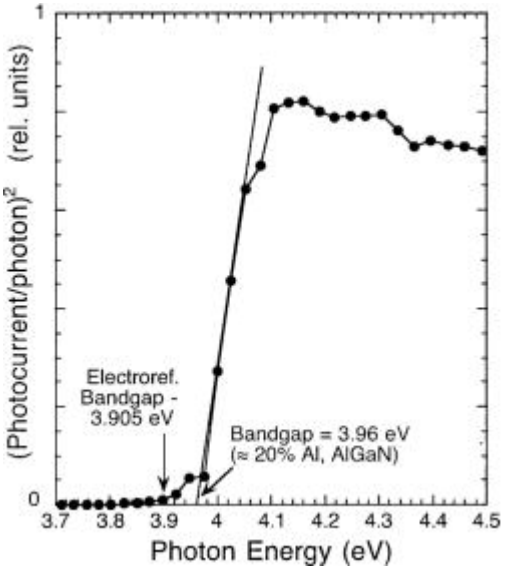

Fig. 8.6. Photocurrent spectrum for the $Al_{0.19}Ga_{0.81}N$ (320 Å) /GaN hetero-structure (300 K). AlGaN band gaps determined by photoconductivity and electroreflectance are indicated in the figure.

The AlGaN barrier photoconductive response (see Fig. 8.6) provided an independent measurement of band-gap, and we obtained an AlGaN band-gap of 3.96 eV @300 K (20% Al) [8.17, 8.18] which was in reasonable agreement with the band gap determined by analysis of the FKO line shape. Perhaps the small feature at 3.90–3.97 eV in the photoconductive response is a Urbach-tail associated with localization, but it was not observed consistently in other samples. Lattice constants of the biaxially strained AlGaN barrier were determined from x-ray diffraction measurements. Using the elastic constants [8.20] and Vegard's law, we obtained a composition (20.0±0.5%

Al) consistent with that determined indirectly through our optical measurements of the AlGaN band gap.

Electric fields determined from the FKO period in Figs. 8.2(a)–8.2(d) are plotted in Fig. 8.7. The electric field was roughly linear versus gate bias with the slope indicating ≈ 100% of the bias dropped across the AlGaN barrier, not the ohmic contacts or 2DEG channel. Averaging over the data in Fig. 8.7, we measured a 0 V bias, AlGaN polarization electric field of 0.25±0.05 MV/cm (*w*/2DEG density of 7.4×10^{12} e/cm^2). The AlGaN electric field predicted by the "standard model" for an $Al_{0.19}Ga_{0.81}N$ (320 Å)/GaN heterostructure is also shown in Fig. 8.7 (dashed line). The model predicted an electric field of 0.33 MV/cm and 2DEG density of 8.7×10^{12} e/cm^2@0 V bias [refer to Fig. 8.1(a)].

Over the energy range 3.3–3.9 eV, the solid lines in Figs. 8.2(a)– 8.2(e) represent the sum of the best FKO line shape and a linear combination of the real and imaginary electromodulated dielectric functions from Figs. 8.3(a) and 8.3(b). To calculate the results in Figs. 8.2(a)–8.2(e) the Seraphin coefficients (which are proportional to the coefficients in the aforementioned linear combination) were fixed, independent of voltage. The dielectric functions in Figs. 8.3(a) and 8.3(b) were calculated from Schrödinger–Poisson solutions for $Al_{0.19}Ga_{0.81}N$ (320 Å)/GaN with 85% of the "standard model" interfacial polarization charge to produce an electric field of 0.31 MV/cm and the measured 2DEG charge density @0 V bias. Comparing data with the model in Fig. 8.2, clearly the calculation of the dielectric function described the spectral shift with charge density of the 2DEG electroreflectance feature. Also, the model accounted for the ≈ 4× change in amplitude of the 2DEG feature over 0 to –3 V bias. Using no adjustable parameters, Fig. 8.2(e) is the predicted electroreflectance spectrum for the heterostructure at –4 V bias [see Fig. 8.1(b) for band structure @–4 V]. Although this spectrum was not measured due to the large resistance of the 2DEG prior to depletion, our models are capable of generating the spectrum based on analysis of the lower voltage results.

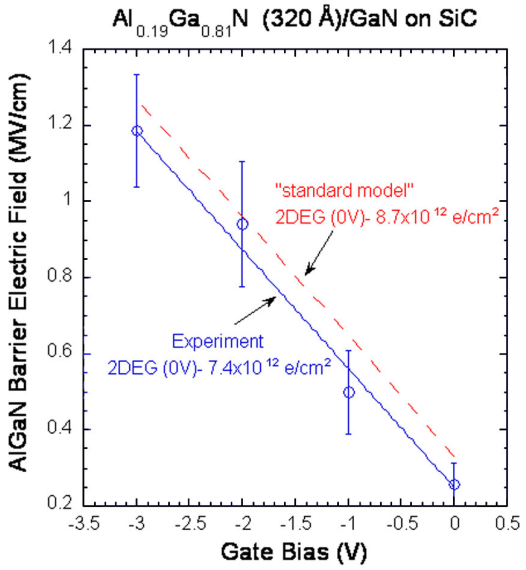

Fig. 8.7. Electric field vs gate bias obtained from the electroreflectance spectra in Figs. 8.2(a)–8.2(d). Electric field predicted by the "standard model" for an $Al_{0.19}Ga_{0.81}N$ (320 Å)/GaN heterostructure is indicated by the dotted line.

Several mechanisms could produce both an electric field and 2DEG density slightly lower than the "standard model." One of the simplest modifications would be to allow partial strain relaxation of the AlGaN layer which would reduce the interfacial polarization charge, electric field, and 2DEG density, but x-ray diffraction indicated that the AlGaN layer was unrelaxed. As we observed in comparing heterostructures grown on SiC and sapphire, material issues such as Al composition gradients, inhomogeneities or roughness, etc. should

be considered before proposing revision of bandstructure models to produce measured electric fields and 2DEG densities.

8.6 Conclusions

Contacted electroreflectance studies of AlGaN/GaN heterostructures and their 2DEGs compliment conventional electrical and transport measurements and provide direct measurement of characteristics associated with bandstructure and material quality. The electric field and composition of the thin (<400 Å) AlGaN barrier was determined by analyzing the gate voltage-tunable FKO line shape. For a high mobility (higher quality) $Al_{0.19}Ga_{0.81}N$ (320 Å)/GaN heterostructure grown on SiC, the measured AlGaN barrier electric field (0.25±0.05 MV/cm @0 V bias) approached the value predicted by a standard heterostructure model (0.33 MV/cm). Adjusting model interfacial polarization charge to produce the measured 2DEG density (7.4×10^{12} e/cm^2, @0 V bias), the calculated electric field (0.31 MV/cm) reached reasonable agreement with the measured value. With the convergence of measured and calculated electric fields, we are confident that electroreflectance will become an important tool to monitor the material-driven evolution of nitride heterostructure models and devices.

The 2DEG produced a broad, voltage-tunable first derivative electroreflectance feature. We developed a method to calculate the electromodulated dielectric function from the results of Schrödinger–Poisson calculations of 2DEG energies, wave functions, and band bending. Our model described the line shape and relative amplitude of the 2DEG electroreflectance feature over a wide range of electron density and gate voltage. The example of our 2DEG contacted electroreflectance measurements and model may shed new light on other reflectance studies where extra features are sometimes attributed to the 2DEG.

8.7 References

[8.1]. M. A. Khan, J. N. Kuznia, J. M. Van Hove, N. Pan, and J. Carter, Appl. Phys. Lett. **60**, 3027 (1992).

[8.2]. M. A. Khan, J. N. Kuznia, D. T. Olsen, W. J. Schaff, J. W. Burm, and M. S. Shur, Appl. Phys. Lett. **65**, 1121 (1994).

[8.3]. S. N. Mohammad, A. A. Salvador, and H. Morkoç, Proc. IEEE **83**, 1306 (1995).

[8.4]. J. M. Redwing, M. A. Tischler, J. S. Flynn, S. Elhamri, M. Ahoujja, R. S. Newrock, and W. C. Mitchel, Appl. Phys. Lett. **69**, 963 (1996).

[8.5]. O. Ambacher, J. Smart, J. R. Shealy, N. G. Weimann, K. Chu, M. Murphy, W. J. Schaff, L. F. Eastman, R. Dimitrov, L. Wittmer, M. Stutzmann, W. Rieger, and J. Hilsenbeck, J. Appl. Phys. **85**, 3222 (1999), and references therein.

[8.6]. C. Wetzel, T. Takeuchi, H. Amano, and I. Akasaki, J. Appl. Phys. **85**, 3786 (1999).

[8.7]. Y. T. Hou, K. L. Teo, M. F. Li, K. Uchida, H. Tokunaga, N. Akutsu, and K. Matsumoto, Appl. Phys. Lett. **76**, 1033 (2000).

[8.8]. S. R. Kurtz, A. A. Allerman, D. D. Koleske, and G. M. Peake, Appl. Phys. Lett. **80**, 4549 (2002).

[8.9]. D. Y. Lin, Y. S. Huang, Y. F. Chen, and K. K. Tiong, Solid State Commun. **107**, 533 (1999).

[8.10]. E. S. Snow, O. J. Glembocki, and B. V. Shanabrook, Phys. Rev. B **38**, 12483 (1988).

[8.11]. D. J. Hall, T. J. C. Hosea, and D. Lancefield, J. Appl. Phys. **82**, 3092 (1997).

[8.12]. P. Y. Yu and M. Cardona, *Fundamentals of Semiconductors*, 3rd ed. (Springer, Berlin, 2001).

[8.13]. M. Suzuki and T. Uenoyama, Solid-State Electron. **41**, 271 (1997).

[8.14]. F. H. Pollak and H. Shen, Mater. Sci. Eng., R. **10**, 275 (1993).

[8.1]. X. Z. Dang, P. M. Ashbeck, E. T. Yu, G. J. Sullivan, M. Y. Chen, B. T. McDermott, K. S. Boutros, and J. M. Redwing, Appl. Phys. Lett. **74**, 3890 (1999).

[8.15]. D. Jena, A. C. Gossard, and U. K. Mishra, Appl. Phys. Lett. **76**, 1707 (2000).

[8.16]. T. J. Ochalski, B. Gil, P. Lefebvre, N. Grandjean, M. Leroux, J. Massies, S. Nakamura, and H. Morkoç, Appl. Phys. Lett. **74**, 3353 (1999).

[8.17]. H. Jiang, G. Y. Zhao, H. Isikawa, T. Egawa, T. Jimbo, and M. Umeno, J. Appl. Phys. **89**, 1046 (2001).

[8.18]. F. H. Pollak, *Group III Nitride Semiconductor Compounds*, edited by B. Gil (Clarendon, Oxford, 1998).

[8.19]. A. F. Wright, J. Appl. Phys. **82**, 2833 (1997).

9. HEMT Characteristics for Optimized GaN/AlGaN Growth

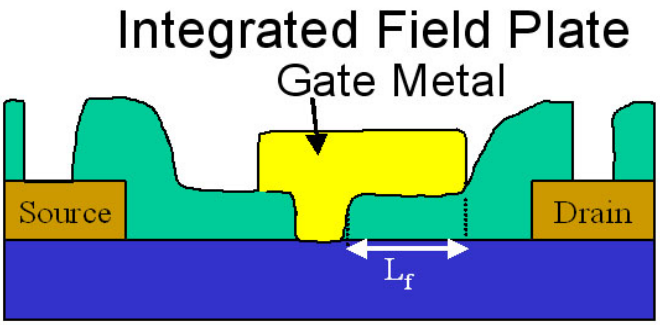

Fig. 9.1. Cross section of a HEMT with a field plate structure.

With improved material quality and an improved method of passivation, devices were fabricated with improved performance. Device fabrication involves the following steps: First the device active regions are defined by mesa isolation using either reactive-ion etching or inductively-coupled etching. Following isolation, source and drain metal contacts for the transistor are defined and deposited using TiAlNiAu. The ohmic contacts are alloyed, typically at temperatures near 875 C. Following ohmic contact formation, optical gates are aligned and placed in the gap between the source and drain contacts. The metal layers used in optical gate formation were Ni/Au. On certain wafers electron beam gates are defined and deposited between gate and drain contacts. These three steps of isolation, ohmic contact formation, and gate deposition define the active transistor. The transistors are next passivated with the optimized SiN dielectric for low rf dispersion. Further processing steps are performed if airbridges are desired to connect large number of gate fingers for a higher current and higher power device. Passive elements such as resistors, capacitors, and transmission lines may also be fabricated if a monolithic integrated circuit is desired. Backside processing for wafer thinning and source via grounds may also be used. A device cross section is shown in Fig. 1.1.

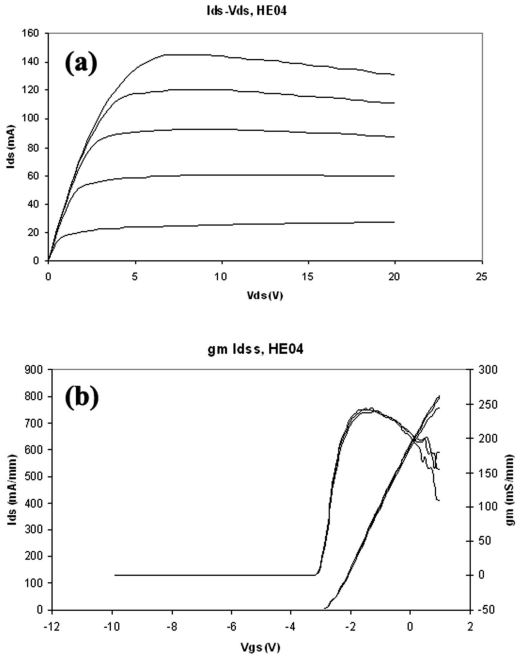

Fig. 9.2. Drain I-V characteristics for a 0.6x150 mm GaN HEMT. (a) I_{DS} vs. V_{DS}, (b) I_{DS} vs. I_{GS}.

During the course of this LDRD, two types of basic devices were used. The first type, a conventional process is shown in Fig. 1.1 and described above. Another type of process used a "field plate" for moderating the peak electric

field between the gate and the drain, as illustrated in Fig. 9.1. In this process, the SiN passivation occurs prior to gate formation. The gate is then formed after etching an opening into the SiN and re-patterning gate metal to cover the opening and a part of the gate-drain space. HEMTs using either type of gate should be able to validate improvements in GaN material growth.

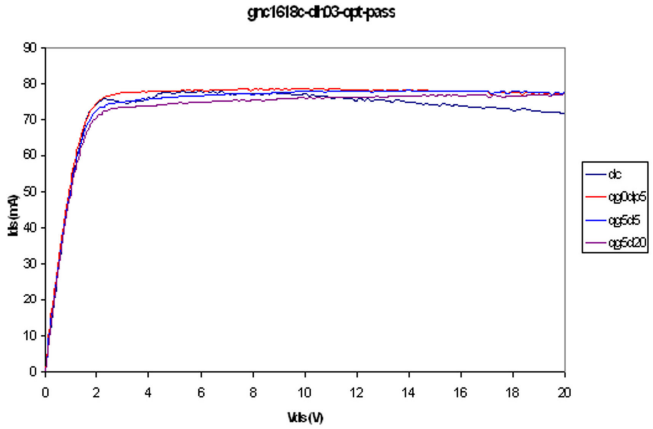

Fig. 9.3. Pulsed I-V characteristics for a 1 x 150 mm GaN HEMT. The quiescent condition is V_{DS}=20V, V_{GS}=−5V.

A baseline HEMT structure emerged during this LDRD based on the following generic structure: a 100 nm AlN nucleation layer grown on a SiC substrate, an approximately 1000 nm thick GaN buffer layer, and a 18-21 nm AlGaN layer with 25-27% Al. Such a structure yielded excellent I-V curves as illustrated in Figure 2 with little current collapse, as illustrated in Fig. 9.3. Peak transconductance is in excess of 250 mS/mm for a 0.6 µm or smaller gate.

The baseline HEMT structure showed excellent DC and pulsed electrical characteristics. It was also characterized for on-wafer power measurements, which are the true test of how devices will perform as power amplifiers. As shown in Fig. 9.4, both small (150 µm periphery) and medium-sized (1.2 mm periphery) gave greater than 5W/mm power density at 10 GHz. Power-added-efficiency was measured in excess of 50% for these devices.

These results on the baseline structure are typical results which validate the material optimization process which were repeated on a baseline structure at several time points during the LDRD work. The repeated structures were either characterized with power sweep measurements, as described above, or were used in actual power amplifier builds. Although power measure-ments were not carried out on all growth experiments described in previous sections, pulsed I-V measurements were carried out for a number of these. Pulsed I-V measurements have been shown to be a good predictor of power output [9.1]. Several variations on the baseline structure gave good pulsed I-V measurements and are also promising candidates for power amplifier applications.

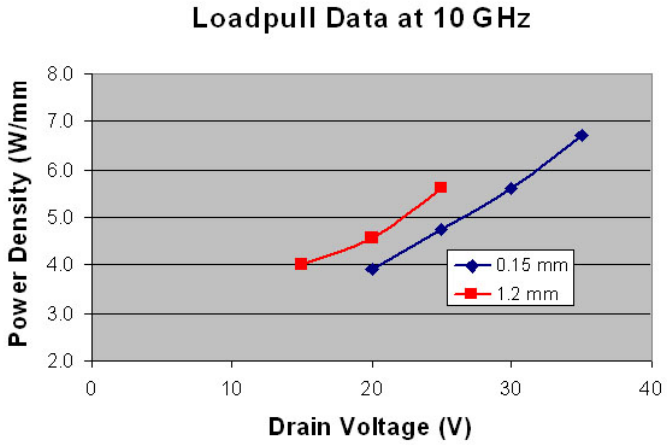

Fig. 9.4. Power density for 150 µm and 1.2 mm periphery GaN HEMTs acquired using on-wafer load pull power sweeps.

HEMTs with growth pressure in the range of 150-300 Torr, several types of surface termination, and those growth with an AlN interface (prior to AlGaN growth) gave good pulsed I-V results, which are an indication that the materials technology has improved sufficiently during this LDRD to be of practical use.

9.1 Improved Passivation for GaN HEMTs.

The first key to success in building GaN-based amplifiers is to start with high quality materials and processes. The electron mobilities and sheet concentrations measured in our baseline material compare favorable to those reported in the literature. They are sufficient to predict good DC properties in HEMTs. They are a necessary but not sufficient condition for achieving good rf properties as well. The rf properties are not predictable based on any known material characterization techniques at present. It is necessary to know how to predict whether samples are susceptible to rf dispersion effects (where transistor properties are frequency dependent). In particular, current collapse (large drops in drain current of a FET that occur on a fast time scale after application of a set of gate and drain bias pulses) effects in GaN are widespread. They are associated with various trap locations created in growth or with traps at the gate-drain surface created by growth or processing. Various growth initiatives are described in other sections of this LDRD. In this section, the pulsed I-V technique for evaluating current collapse is described. An improved method for reducing rf dispersion and current collapse in GaN HEMTs by SiN_x passivation is also described. Gate-lag measurements (a specific form of pulsed I-V measurement, where gate voltages are pulsed from off-to-on conditions and drain-current pulses are measured) have long been used to characterize rf dispersion in GaAs devices. We have adapted these methods to GaN devices. In particular, we developed three useful quiescent conditions that place low, medium and high stress to GaN devices. With these methods we have observed samples with up to 99% current collapse (in unapassivated wafers). Most of the cases of high current collapse occurred in unpassivated wafers. SiN_x has been reported to alleviate current collapse in GaN HEMTs. However, our SiN_x has shown a wide range of outcomes when evaluated for current collapse. After exploring some of the deposition parameters for SiN_x deposition, we have found that temperature (increasing) and to a lesser extent SiH_4 flow (increasing) reduces current collapse in GaN HEMTs. An example of moderate current collapse with SiN_x deposited at 250C and moderate SiH_4 flow is compared with a better SiN_x film deposited at 300C and high SiH_4 flow showing low current collapse (Figure 1). In these examples, the pulsed I-V characteristics under high drain bias quiescent conditions (and negative gate bias) show the current decrease compared to the DC currents.

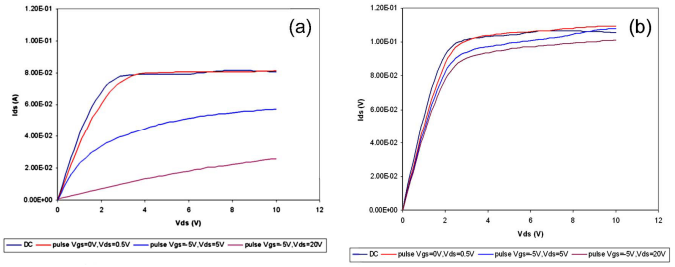

Fig .9.5 Example of SiN_x passivation with moderate (left) and low (right) current collapse.

9.2 References

[9.1]. S.C. Binari, K. Ikossi, J. A. Roussos, W. Kruppa, D. Park, H. B. Dietrich, D. D. Koleske, A. E. Wickenden, and R. L. Henry, IEEE Trans. Electron Devices 48, 465 (2001).

Distribution:

1	MS0601	Daniel D. Koleske	1126
1	MS0601	Andrew A. Allerman	1126
1	MS0601	Robert M. Biefeld	1126
1	MS0601	Stephen R. Lee	1126
1	MS0603	Albert G. Baca	1742
1	MS0603	Charles T. Sullivan	1742
1	MS0603	Phillip F. Marsh	1742
1	MS0603	Ronald D. Briggs	17421
1	MS0603	Christopher P. Tigges	1713
1	MS0603	Randy J. Shul	1723
1	MS1056	David M. Follstaedt	1111
1	MS1056	Paula P. Provincio	1111
1	MS1415	Alan F. Wright	1112
1	MS1415	Nancy A. Missert	1112
2	MS9018	Central Technical Files	8945-1
2	MS0899	Technical Library	4536
1	MS0188	D. Chavez, LDRD Office	01011


Sandia National Laboratories